# COUPLING NITROGEN VACANCY CENTERS IN DIAMOND NANOPILLARS TO WHISPERING GALLERY MICRORESONATORS

by

KHODADAD NIMA DINYARI

A DISSERTATION

Presented to the Department of Physics
and the Graduate School of the University of Oregon
in partial fulfillment of the requirements
for the degree of
Doctor of Philosophy

December 2012

DISSERTATION APPROVAL PAGE

Student: Khodadad Nima Dinyari

Title: Coupling Nitrogen Vacancy Centers in Diamond Nanopillars to Whispering Gallery Microresonators

This dissertation has been accepted and approved in partial fulfillment of the requirements for the Doctor of Philosophy degree in the Department of Physics by:

| | |
|---|---|
| Dr. Steven van Enk | Chairperson |
| Dr. Hailin Wang | Advisor |
| Dr. Miriam Deutsch | Member |
| Dr. Steve Kevan | Member |
| Dr. Mark Lonergan | Outside Member |

and

| | |
|---|---|
| Kimberly Andrews Espy | Vice President for Research and Innovation/Dean of the Graduate School |

Original approval signatures are on file with the University of Oregon Graduate School.

Degree awarded December 2012

DISSERTATION ABSTRACT

Khodadad Nima Dinyari

Doctor of Philosophy

Department of Physics

December 2012

Title: Coupling Nitrogen Vacancy Centers in Diamond Nanopillars Whispering Gallery Microresonators

For cavity quantum electrodynamics systems (cavity-QED) to play a role in quantum information processing applications and in quantum networks, they must be robust and scalable in addition to having a suitable method for the generation, processing and storage of quantum bits. One solution is to develop a composite system that couples a nitrogen vacancy (NV) center in diamond to a whispering gallery mode supported by a fused silica microsphere. Such a system is motivated by the optical and electron-spin properties of the NV center. The NV center is the leading spin-qubit and exhibits atomic like linewidths at cryogenic temperatures and has spin coherence times greater than milliseconds at room temperature. These long coherence times, coupled with nanosecond scale spin readout and manipulation times, allow for millions of quantum operations to be processed. Silica whispering gallery resonators are the only class of microresonators with quality factor high enough to reach the strong coupling regime, which is necessary for some quantum information processing applications.

Integrating these two components into a system that could position a diamond nanopillar near the surface of a deformed-double stemmed microsphere system, with nanometer precision, at 10 K was a major achievement of this research. Cavity resonances in deformed microspheres can be excited with a free-space coupling technique which simplifies their integration into cryogenic environments. In these intentionally deformed resonators, an enhanced evanescent field decay length was observed at specific locations along the ray orbit. The double-stem arrangement enables the cavity resonance to be tuned over 450 GHz, with sub-10 MHz resolution, at 10 K. These two features, the enhanced decay length and broad range tuning with high resolution, are indispensible tools for cavity-QED studies with silica microspheres.

Diamond nanopillars were fabricated from single crystal diamond with diameters as small as 140 nm in order to maintain a high quality factor. Studies were conducted on NV centers in nanopillars and bulk diamond to determine their suitability for cavity-QED applications. In an attempt to increase the light-matter interaction between NV centers and whispering gallery modes, diamond substrates were optically characterized that were irradiated with nitrogen ions.

CURRICULUM VITAE

NAME OF AUTHOR: Khodadad Nima Dinyari

GRADUATE AND UNDERGRADUATE SCHOOLS ATTENDED:

University of Oregon, Eugene
University of California, Santa Barbara
Cabrillo College, Aptos, California

DEGREES AWARDED:

Doctor of Philosophy, Physics, 2012, University of Oregon
Bachelor of Science, Physics, 2004, University of California, Santa Barbara

AREAS OF SPECIAL INTEREST:

Cavity Quantum Electrodynamics
Nano- and Micro-Fabrication

PROFESSIONAL EXPERIENCE:

Research Assistant, Hailin Wang, Department of Physics, University of Oregon, 2008 - present.

Teaching Assistant, Department of Physics, University of Oregon 2005 - 2008

GRANTS, AWARDS, AND HONORS:

National Science Foundation IGERT Fellowship, Material Science Institute, University of Oregon, 2010 – 2011

National Science Foundation GK12 Fellowship, Material Science Institute, University of Oregon, 2008 – 2010

PUBLICATIONS:

Khodadad Nima Dinyari, Russell Barbour, David Golter and Hailin Wang, Mechanical Tuning of Whispering Gallery Modes over a 0.5 THz Tuning Range with MHz Resolution in a Silica Microsphere at Cryogenic Temperatures, Optics Express, 19 19, 17966-17972 (2011)

Russell J. Barbour, Khodadad N. Dinyari and Hailin Wang, A Composite Microcavity of Diamond Nanopillar and Deformed Silica Microsphere with Enhanced evanescent decay length, Optics Express, 18 18, 18968-18974 (2010)

Mats Larsson, Khodadad Nima Dinyari and Hailin Wang, Composite Optical Microcavity of Diamond Nanopillar and Silica Microsphere, Nano Letters, 9 4, 1447–1450 (2009)

Dustin Kleckner, William Marshall, Michiel J. A. de Dood, Khodadad Nima Dinyari, Bart-Jan Pors, William T. M. Irvine, and Dirk Bouwmeester, High Finesse Opto-Mechanical Cavity with a Movable Thirty-Micron-Size Mirror, Physical Review Letters 96, 173901-173901-4 (2006)

ACKNOWLEDGMENTS

None of this could be done on my own. I appreciate all of the collaborations that I was so fortunate to be a part of. Mom and Dad, thank you for everything that you have done. You have been an important part of my life and helped me in the ways you knew best. Niloo and Farbod, thanks for being the best sister and brother I could hope for. The Millers, you are family; thank you for being a part of my life. There were so many influential teachers that I had growing up and they all helped me find my path towards physics. I really appreciated the Math Academy in the Pajaro School District and that demo show by Leila Drake's uncle. Carlos Figueroa and the whole Cabrillo College program was an awesome opportunity for me to grow as a physicist and a leader. Once at UCSB, I was excited to do science research as well as studying it in the classroom. Phil Lubin, you were such a pleasure to work with. Dirk Bouwmeester, it was an honor to work with you and your fantastic research team.

One of the first people I became friends with at the UO was Bonnie Grimm. She helped me with all kinds of things from academics to who my dentist should be. I had a great cohort to study and teach physics with during my first two years in graduate school. Nate and Mick, thank you for putting up with me. You kept me sane. I am fortunate to have joined the Wang Group in the summer of 2006. Thank you Hailin for your hard effort, guidance and support. I will never forget this experience you provided to me and I will make the best of it. To the Wang members before me thank you. A special thanks to Yumin, Shannon, Young-Shin and Yan for being there during my arrival and showing me

how to get started. I was stoked that Carey and Tim joined the group at the same time. Thanks you two for being great lab partners

I am so fortunate to have had worked with three postdocs while at the UO. Mats, I love you and thanks for being so darn fun. Ann, I love you too, don't worry. Really though, Mats helped me get this project rolling and was there at the beginning when there were so many mistakes and discouraging moments. Russell, you helped immensely and brought some awesome knowledge and expertise with you from Scotland. Chunhua, all I can say is that you are selfless, truly selfless. Thank you for the fun times in China and hard work in the USA. Hard work, is that Andrew? Thanks Andrew for believing even when I gave up hope. You are a great friend and colleague. Tom, Thein, Mark and Victor, you guys are rad and thanks for putting up with my BS.

The machine shop crew deserves a big shout out. Kris, Jeffrey, John and David, thank you for putting up with me and helping me have such a fun time while building my experiments. Kurt, thanks for helping me down in CAMCOR. Ngoc, thanks for helping me anneal my samples. Brandy and Jen, you two totally ROCK! Brandy, thank you so VERY much for editing this entire dissertation with me.

To my neighbors, the dog walking crew, and Jason and Les, thanks for caring for me. Sam, thanks for helping me during the hardest part of my life so far. Lastly, I would like to thank those that I haven't explicitly thanked above. You are appreciated greatly. Trust me.

For everyone before me and to everyone who follows.

TABLE OF CONTENTS

Chapter Page

Chapter Page

LIST OF FIGURES

Figure Page

Figure Page

Figure Page

Figure Page

Figure Page

LIST OF TABLES

# CHAPTER I

# INTRODUCTION

Albert Einstein helped develop the concept of spontaneous decay of an atom, which was initially thought to be a property of the emitter, but was later shown by Purcell to be a function of its environment. This concept of spontaneous decay was necessary in order to develop a more accurate picture of Planck's Blackbody Radiation Law; it describes the electromagnetic energy intensity distribution for a blackbody, as a function of its wavelength, when it is in thermal equilibrium with its surroundings [1]. It took further development of quantum electrodynamics to understand that the environment influences the decay rate of an emitter. Paul Dirac initially developed the theoretical foundation of quantum electrodynamics with his seminal work quantizing the electromagnetic field [2, 3].

Amongst other things, Dirac contributed the concept of operator theory where, for example, the creation and annihilation, or ladder operators are used to find the eigenenergies and eigenvectors of a quantum harmonic oscillator. Dirac also developed the formalism of the quantum electrodynamics vacuum state. This concept is deeply rooted in quantum optics, and it is this atom-vacuum interaction that accounts for the shift of the ground state energy of an atom. The experimental study of the fine structure of hydrogen revealed this shift, the Lamb shift, which resulted in the Nobel Prize in Physics in 1955 [4]. This shift comes through the coupling of the electron to the vacuum

state. This framework of the electromagnetic vacuum lead to other theoretical discoveries including the natural linewidths of atoms and the total spontaneous emission rate of atoms by Weisskopf and Wigner, and the Casimir-Polder force between two plane conductors and quantum beats [5, 6, 7, 8].

There was great progress in quantum field theory during the first half of the twentieth century in the context of charged particles interacting through the exchange of photons. On the other hand, the theoretical framework of optical phenomena was still semi-classical in the sense that the sources of photons were treated quantum mechanically but the field radiation was treated classically. Quantum optics was granted its status as a distinct branch of physics during the time around the development of the Hanbury-Brown-Twiss (HBT) interferometer. These developments lead to the theory and understanding of photon statistics through the correlations and fluctuations of the photo-induced currents in detectors[9, 10]. The HBT interferometer was first utilized as an astronomical tool used to determine the angular size of the star Sirius. Now, it is an indispensable tool in quantum optics. Theoretical work continued to make progress in the field of quantum optics and as technology became more mature (laser development, detector improvement, optical coatings, microfabrication, etc.) in the latter years of the twentieth century, experimental studies began in earnest to understand atomic decay and how the modification of the local environment affected the dynamics of these rates.

Some of the first experimental results from the field of quantum optics focused on the statistics of laser emission and the observation of photon bunching from Gaussian sources of photons [11, 12, 13]. It was observed in an earlier experiment by Drexhage that the decay rate of optical emitters could be modified by varying the thickness of a

dielectric layer, which acted as the spacer, between the emitter and the conductive surface [14]. It was observed that the emission from the dye was suppressed when the spacing between the emitter and the surface was less than the emission wavelength. Studies naturally progressed towards microcavity systems. Initially, optical cavities were constructed from two mirrors forming a Fabry-Perot style resonator. With the aid of ion traps, atoms could be directed through the gaps of the mirrors providing the other ingredient in cavity-QED studies, the emitters.

The first experiments were conducted with atoms (Na, Cs) prepared in the Rydberg state, which could interact with cavities in the microwave regime [15, 16]. In the experiment conducted by Goy, et al., the lifetime of the atoms was reduced during the brief period of time that the atoms were coupled to the cavity. In the work by Hulet, et al., the decay rate of the atoms was inhibited due to their interaction with the cavity, resulting in an increase in the emission lifetime. Many other experiments followed and the normal-modes the of the coupled oscillator system was first observed in 1992 with the strong coupling regime and the use of cold Cs atoms coupled to a double concaved optical cavity [17, 18, 19, 20]. In the experiment by Thompson, et al., the vacuum Rabi splitting with few atoms ($N_{ave} \leq 10$) was first measured directly with a coupling rate slightly larger than the other two decay rates of the system.

The years to follow showed improvement in cavity-QED systems thus enhancing the coupling rate by increasing the finesse and reducing the effective mode volume of the cavities. These and other improvements in cavity-QED technology resulted in an explosion of quantum optics experiments. Nonlinear optical studies of atoms and photons became possible and included measurements such as nonlinear phase shifts

between two modes of a cavity mediated through by single atom [21]. Strong coupling systems also allowed for quantum non-demolition experiments on single photons [22]. In this work, atomic interferometry was used to study the phase shift resulting from the cyclic emission and re-absorption of energy from single photons stored in the cavity mode. These advances lead to the creation of "single atom" micro-laser with barium atoms. They were prepared in such a way that once they entered the optically empty cavity and coupled to the optical mode they could then act as the gain medium [23]. By the end of the 1990s, cavity-QED technology with Fabry-Perot style cavities even enabled researchers to map the trajectories of single atoms in the cavity[24]. This was done by monitoring the modulation spectrum of a transmission probe beam through the cavity to reconstruct the trajectory of the individual atoms.

This sequence of events lead to the understanding that cavity-QED systems would play an integral role in quantum information processing schemes [25, 26, 27, 28, 29, 30]. Typical of most schemes is that the fact that the atoms are used to generate, manipulate and store quantum information while the cavity provides an enhanced readout of the photons, which can then be transmitted. In this picture, atoms could be thought of as the stationary qubit and the transmitted photon is the flying qubit. Since the turn of the millennium, various approaches to cavity-QED systems have been theorized, developed and implemented, each having their relative advantages and disadvantages.

Shifting the approach away from the work horse of cavity-QED set-ups, Fabry-Perot style cavities with cold atoms, to more integrated devices was seen as a necessity because it would be difficult to scale up such a system for quantum computation or communication purposes. The tremendous overhead of the system makes it incompatible

with the type of scalability that is envisioned for the future of quantum computation. As an example, a major component of the operation traps, cools and injects atoms into the cavity. This a huge undertaking independent from the rest of the experiments and the placing of emitters in the cavity results in couplings times that last only on the order of seconds. There is always going to be a drive to decrease the complexity of the system no matter what advances have been reached and this drive has pushed technology towards smaller and more integrative devices. That is why other options for emitters and cavity geometries cavities are still under exploration. However, the Fabry-Perot class of resonators is the most advanced when it comes to optical cavity-QED studies and has yet to be surpassed by any other system design.

Microsphere, microdisk, and microtoroid systems can be used in composite cavity-QED systems with cold atoms as well as with solid-state emitters [31, 32, 33, 34, 35, 36, 37]. These devices are depicted in Fig. 1.1. Of these three types of devices, microspheres were the first type to be pursued for the prospects of strong-coupling cavity-QED due to their extremely high quality factors (as high as the $10^9$ to $10^{10}$ range) as well as their relatively small mode volumes. Locating cold atoms within the evanescent field of the cavity makes this approach difficult. Regardless, strong coupling was achieved between cesium atoms and a micotoroidal resonator in 2006 [38].

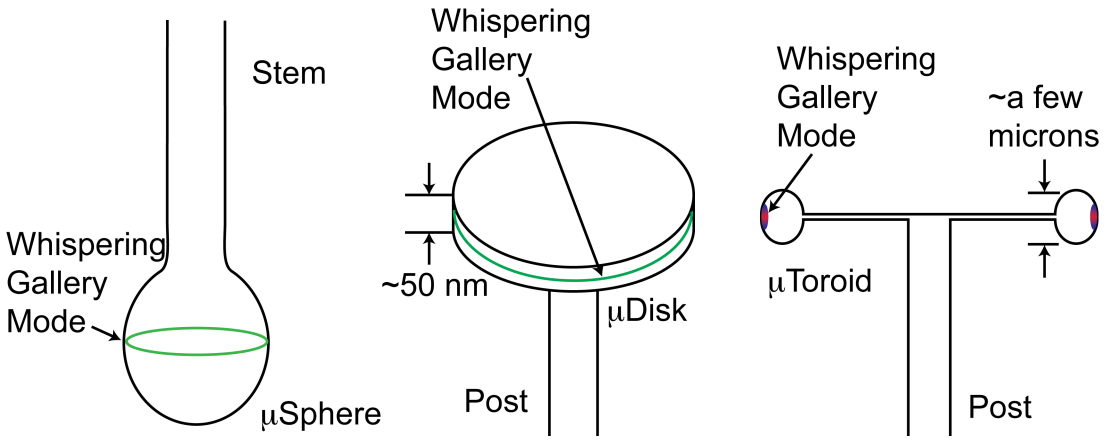


Figure 1.1: Microresonators cavities include a) microsphere b) microdisk and c) microtoroid geometries.

Other approaches developed monolithic structure where the cavity was designed with an emitter embedded into the microresonator body [39, 40, 41, 42]. The earliest of these approaches achieved the strong coupling regime with either a photonic crystal or Bragg-stack micropillar cavity with quantum dots embedded into the cavity region [43, 44]. In 2005 Peter, et al., demonstrated strong coupling between quantum dot emitters in a semiconductor microdisk. As these fabrication techniques became more mature over the past decade, the quality factor of the resonators has been steadily approaching their theoretical limit.

For specific applications, techniques are being developed to fabricate photonic crystal and microdisk devices, on an industrial scale, in order to play the role of classical or quantum light sources in integrated photonic chips [45, 46]. Figure 1.2 depicts the basic layout of a photonic crystal and a micropillar cavity. Photonic crystals are periodic structures where the modulation period is on the order of the wavelength of light that is to be interfaced with the device. Many designs are available and Fig. 1.2a shows a two-

dimensional array of holes in a triangle pattern which act as distributed Bragg reflectors. The thickness of the slab is used for partial confinement in the out of plane direction.

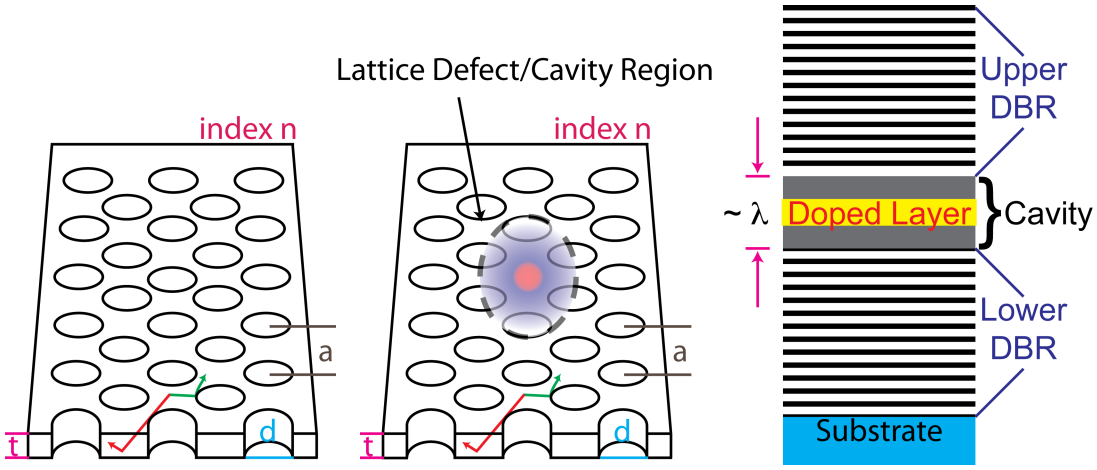


Figure 1.2: A cartoon depicting monolithic designs for a) Bragg reflector b) photonic crystal or c) Bragg-stack cavities, where the latter two designs can be used in cavity-QED systems.

True 3D photonic crystals are difficult to fabricate and by making thin slabs of crystals the structures can have some 3D photonic crystal properties without fewer technical challenges. Cavities in such structures rely on a "defect" being introduced in the periodic lattice, and if the design is done properly, mode volumes for these resonators are approximately $(\lambda/n)^3$. These mode volumes are considerably smaller than all other classes of resonators. This is shown in Fig. 1.2b. The general idea for micropillar geometries is depicted in Fig. 1.2c. Here, the planar geometry of the doped layer ensures that the light is confined in the vertical direct.

In these designs, the confinement of light in the growth direction of the substrate is typically accomplished with two mirrors, comprised of $\lambda/4$-thick alternating dielectric

material, forming a mirror pair around the doped region. The top mirror is typically less reflective than the bottom and serves as the input/output optic for the cavity. Photonic crystal cavities have the smallest mode volumes of all semiconductor cavity arrangements with volumes on the order of a cubic micron. Microdisk and micropillar cavity geometries can exhibit relatively small mode volumes that are on the order of one to ten cubic microns. However, in these monolithic cavity designs a few limitations exist, as is the case in any cavity-QED approach.

Regarding photonic crystals and micropillars, though the fabrication techniques have progressed they still limit the overall quality factor of the devices. This is primarily due to sidewall roughness, imperfections in mirror coatings and non-uniform holes in the photonic lattice. Even under ideal conditions, the theoretical values for the quality factors are less than that of microspheres. Also, the emitter's location relative to the anti-node of the cavity is hard to control, even with markers and pre-selection techniques slight misalignments in position or resonance frequencies result in a lower value for the cavity-coupling rate. In microsphere or microtoroid geometries, the major limitation for cavity-QED studies is the fact that the emitter interacts with the evanescent field of the cavity. The intensity outside of these silica microresonators is much weaker than the maximum value, which is found just inside of these devices for the most tightly confined modes. Also, these composite systems rely on positioning the emitter as close to the sphere surface as possible. Though this is an advantage in the sense that the emitter can be optimally coupled to the cavity, doing so is difficult, especially at cryogenic temperatures. One difficulty when working with cold atoms and silica microsphere is the

difficultly in trapping cold atoms within a distance from the microsphere surface that is less than the wavelength of light being used.

Low temperatures are typically required when working with solid-state atoms in order to couple their dipole moments to the cavity field and to increase the lifetime of the emitter. Currently, emitters in the solid state have numerous disadvantages when compared to naturally occurring atoms for cavity-QED applications. Engineered atoms can exhibit spectral instabilities, broad linewidths, and inhomogeneous broadening due to variations in the host material and surrounding environment that also cause shifts in the resonance frequency for the optical transition. However, proof of principle systems have been developed and are employed to probe the light-matter interaction between microcavities and emitters in the solid state.

Interesting dynamics of the cavity and emitter have been observed while operating in the different coupling regimes [47, 48]. The Bouwmeester Group has demonstrated strong coupling between self-assembled InAs quantum dots and a photonic crystal cavity fabricated from GaAs[49]. They were able to preselect an individual quantum dot with the desired properties and determine its position relative to an alignment marker on the sample surface with sub-10 nm accuracy. With this information an optimized L3-type photonic crystal was fabricated around the emitter. When these structures were investigated it was determined that seven out of ten devices showed signatures of strong coupling.

Further improvements have to be made in the future for the purpose of generating, processing and storing information with solid-state-emitter based cavity-QED systems

but there is a considerable advantage in having the emitter in the solid state. In this case the qubit is stationary and its position can be optimized relative to the cavity. This makes the operation of the system much less complicated. Solid-state emitters also allow for a broad variety of excitation wavelengths and energy level structures for the atomic states. For example, in the case of a lambda type configuration a laser could probe one transition directly, manipulating the emitter, and the other transition could be coupled to the cavity independent of the operation on the emitter. In the case of data processing, some internal state (i.e. electron or nuclear spin state) of the emitter can be prepared which can be mapped onto the photons in the cavity. The nitrogen vacancy (NV) center is a solid-state center being explored as one such emitter for cavity-QED applications [50, 51, 52, 53, 54, 55]. A major driving factor for incorporating this diamond defect into cavity-QED systems is the electron spin coherence time for the NV center can exceed milliseconds at room temperature [56].

Spin storage times of seconds can be achieved with isotopically pure samples and where the electron spin state has been mapped onto a local carbon-13 atom or the nitrogen forming the diamond color center [57, 58]. These spin-based properties paired with the centers atomic like optical properties make it an ideal candidate for spin based quantum computation schemes. The NV center is the leading spintronic candidate. The spin state of the NV center can be prepared and readout optically, and thus can be manipulated with radio frequency pulses as well as magnetic fields [59]. In high purity single crystal diamond substrates the NV center has optical transitions that are nearly spin preserving with linewidths as small as 10 MHz. Furthermore, the ground and excited states are spin-triplet orbital-doublets in a lambda configuration. In the ground state the

$m_s = 0$ electron spin state is shifted lower in energy from $m_s = \pm 1$ states, with a zero field splitting of 2.87 GHz.

These features as well as other optical and electron spin properties mentioned in later chapters motivate the work presented in this dissertation. The primary goal of this dissertation research was to come up with solutions for the technical challenges of developing of a well-controlled composite cavity-QED system. The system is comprised of i) a diamond nanopillar with nitrogen vacancy centers and ii) a silica microsphere that can support whispering gallery modes. The aim of these technological advances is to develop a system that combines the quantum control of individual photons, electron spins, and nuclear spins. Such a system can be used to realize a solid-state light-matter interface, where an electron spin can be used for optical coupling and a well-isolated nuclear spin is used as a quantum memory. The unique and diverse technical expertise developed in the course of this endeavor is presented here. This includes optical measurement techniques of the NV centers, nanofabrication of diamond nanostructures, microfabrication of deformed double stemmed microspheres, the irradiation of single crystal diamond substrates to induce NV centers near the surface and the engineering of a system that can position a diamond nanopillar near the surface of a microsphere at cryogenic temperatures with nanometer precision.

The hope is that by reducing the nanostructure size enough, the scattering induced quality factor spoiling can be reduced in order to maintain relatively small decay rates for the cavity. The fact that the NV center is a point defect makes it possible to reduced the pillar size while minimizing the effects of the dangling bonds, and other surface effects, on the optical and electron/nuclear spin properties. If this is true then with the right

starting material high quality NV centers can be positioned within tens of nanometers from a microsphere surface. The research presented here develops one possible approach for doing so and in the process develops a number of techniques to overcome typical stumbling blocks in working with microspheres for cavity-QED applications.

There will be a discussion in chapter two regarding cavity-QED and the atom-cavity dynamics in various decay/coupling rate regimes. Chapters three and four discuss the theoretical and experimental fundamentals of fused silica microspheres and the whispering gallery modes they support. Special considerations will be given to deformed microspheres. Chapter five displays a new method to tune the cavity resonance frequency and also presents a study on the evanescent field decay length of deformed microspheres. Chapter six provides some of the theoretical background behind the diamond host lattice and the color centers that dwell within its large band-gap energy. Nitrogen vacancy centers will be discussed in detail as well as possible replacements of the NV center by other diamond color centers currently being researched. Chapter seven explores the relevant optical characterization of NV centers at low temperature when it pertains to cavity-QED systems.

The fabrication of diamond nanopillars from single crystal diamond substrates will be laid out in chapter eight. This chapter also displays the resulting optical characterization of NV centers in these diamond structures at room and liquid helium temperatures. Data in this chapter includes photoluminescence and photoluminescence excitation spectra of NV centers that were present in the nanopillars from either the diamond growth process and from NV centers that were created from ion implantation. Chapter nine describes the development of a composite nanopillar-microsphere system at

room and low temperatures. Some of the techniques that are described in this chapter include a method to increase the coupling of NV centers to the evanescent field of the cavity, a way to tune the cavity resonances to the transition frequency of the center as well as a method to position a nanopillar with nanometer precision relative to the surface of the sphere at 10 K. This dissertation concludes with chapter ten, which is a summary and outlook for research revolving around a cavity-QED system that attempts to couple a NV center in diamond nanostructure to whispering gallery silica microresonator.

# CHAPTER II

# CAVITY QUANTUM ELECTRODYNAMICS AND THE JAYNES-CUMMINGS MODEL

As was mentioned in the previous chapter, the radiative dynamics of an emitter are dependent on its environment. Perturbations from its free-space properties will occur by placing it near a metallic boundary or in an optical cavity. Also mentioned in the previous chapter is the fact that there are numerous systems for studying cavity quantum electrodynamics (cavity-QED) with many of them successfully probing these dynamics. Likewise, there are just as many theoretical approaches for understanding the underlying physics, as there are types of systems. This chapter highlights some of the theoretical aspects of cavity-QED in the context of an atom coupled to a cavity mode, with a slight emphasis on silica microspheres.

The success of the Jaynes-Cummings model has been built upon by many researchers who have taken many approaches at describing the problem of an atom (or collection of atoms) coupled to a photon (or collective excitation of photons) stored in an optical cavity. Some of these approaches continue the semi-classical approach in a way that agrees with quantum treatments and experiments. A completely quantum description of the problem has also been made and in those cases, both the field and the cavity are quantized. The following section provides an overview of the relevant components of cavity-QED in a simplified semi-classical approach. The dynamics of the system are

described in different regimes dependent on the relative size of the coupling rate and the decay rates of the cavity and atom. At the end of this chapter two dimensionless parameters, which are useful in characterizing cavity-QED systems based on these rates are introduced.

## 2.1. Cavity Quantum Electrodynamics

An atomic system can be generalized as a two level system, with a ground ($|g\rangle$) and excited ($|e\rangle$) state separated by an energy $\hbar\omega_a$, if the pair of levels is isolated in energy and by optical selection rules. The two level system can represent an optically active electronic transition of an atom, either naturally occurring or engineered in the solid state, where the resonance frequency $\omega_a$ is far detuned from any other transition. In the rotating wave approximation, upon absorption of a photon with energy $\hbar\omega_a$, the two-level atom makes a transition from the ground state to the excited state. This is depicted in Fig 2.1.

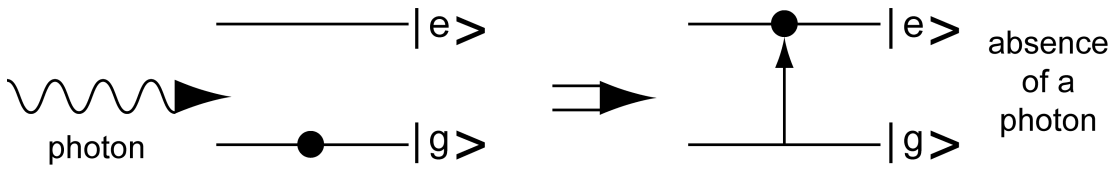


Figure 2.1: Absorption of a photon.

After a certain period of time in the excited state, the system will spontaneously relax back down to the ground state by emitting a photon as is depicted in Fig 2.2. The

spontaneous emission rate γ of this transition can be calculated using Fermi's golden rule and this rate depends on the specifics of the local environment [60]. The decay rate of the excited state is dependent on the dipole coupling strength between the atom and the density of states of the emitted photon. The atom interacts with the local electric field through its dipole moment μ. The coupling strength to the environment is dependent on the specifics of the electric field distribution. As an example, the presence of a plane metallic boundary perturbs the decay rate of an atom in addition to a frequency shift in the optical transition as a function of the distance between the plane and the atom [5]. This geometric arrangement also modifies the radiation field emission pattern for the atom.

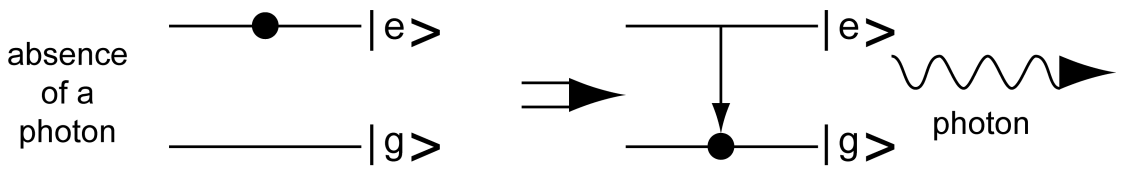


Figure 2.2: Emission of a photon.

This phenomenon can be taken advantage of to increase the interaction strength between an emitter and a single photon as well as increasing the collection efficiency of photons from the atom. The theory for these types of systems has been developed over the past half-century. With advances in optical techniques and fabrication technology over the past two decades, numerous experimental realizations have confirmed theoretical predictions as well as posing new questions and challenges. In the ideal case of a two level atom that interacts with a single mode of an optical cavity, the dynamics of

this well understood atom-cavity system is dictated by the Jaynes-Cummings Hamiltonian [61, 62]:

$$\begin{aligned}\hat{H} &= \hat{H}_{atom} + \hat{H}_{cavity} + \hat{H}_{atom-cavity\ coupling} \\ &= \frac{\hbar\omega_a}{2}\hat{\sigma}_z + \hbar\omega_c\hat{a}^\dagger\hat{a} + i\hbar[g(\mathrm{r})\hat{a}^\dagger\hat{\sigma}^- - g^*(\mathrm{r})\hat{a}\hat{\sigma}^+],\end{aligned}$$

where $g(\boldsymbol{r})$ is the cavity-coupling rate between the emitter and the cavity. Dissipative terms such as spontaneous decay or cavity input/output coupling have been left out here. The two resonances frequencies $\omega_a$ and $\omega_c$ are for the atom and cavity, respectively. The operators $\hat{a}$ and $\hat{a}^\dagger$ are the lowering and raising operators for the cavity mode of interest and the operators $\hat{\sigma}_z$, $\hat{\sigma}^+$ and $\hat{\sigma}^-$ represent the atomic inversion, raising and lowering operators, respectively, for the two level atom.

The first two terms in (2.1) represent the free atom and free cavity Hamiltonians. The last term in this expression represents the Hamiltonian for the cavity-field interaction, which is attributed to the coupling between the dipole of the atom and the electric field of the relevant cavity mode. The details of the dipole moment interaction is hidden in the cavity coupling rate $g(\boldsymbol{r})$. For a fixed dipole, the spatial dependence comes from the variation of the electromagnetic field within the cavity mode volume. In the case where the interaction was maximized the emitter is located at field intensity with the polarization of the electric field parallel to the dipole moment. Under these conditions, the dipole coupling rate, $g(\boldsymbol{r})$, between the electric field and the atomic transition is given by [63]:

$$g(\boldsymbol{r}) = \left(\frac{\mu^2 \omega_c}{2\hbar\varepsilon_0 V_m}\right)\Psi(\boldsymbol{r}) \equiv g_0 \Psi(\boldsymbol{r}). \tag{2.2}$$

In this expression, $\boldsymbol{r}$ represents the center of mass location of the emitter, $\mu = \left|\langle g|\vec{\varepsilon}\bullet\vec{R}|e\rangle\right|^2$ represents the atomic dipole matrix element and $\Psi(\boldsymbol{r})$ is the spatially dependent wave function describing the cavity mode with mode volume:

$$V_m = \int \left|\Psi(\boldsymbol{r})\right|^2 d^3 r. \tag{2.3}$$

This is a generic form of the cavity coupling rate and a more exact form specific to an emitter coupled to a fundamental whispering gallery mode (WGM), with transverse magnetic polarization, in a fused silica microsphere is give by [64]:

$$g(\boldsymbol{r}) = \gamma_\perp \Psi_{s,n,l,m}(\boldsymbol{r})\sqrt{\frac{3c\lambda^2}{4\pi\gamma_\perp V_m}} \tag{2.4}$$

where $\gamma_\perp$ is the transverse decay rate of the emitter, $\Psi_{s,n,l,m}(\boldsymbol{r})$ is the field distribution function for a WGM with *s* polarization (TE or TM) and with WGM numbers ($n$, $l$, $m$) that are described in more detail in chapter three.

Equation (3.20) of chapter three gives an analytical expression for the cavity mode volume $V_m$ of a WGM supported by fused silica microspheres with the mode numbers $n = 1$ and for $l \approx m$; these are the modes of interest for cavity-QED studies because the mode volume is the smallest in such cases. These expressions can be used to estimate the relative size of the dipole coupling rate $g_0$. This value also corresponds to one half the frequency for vacuum Rabi oscillations for an atom at position **r**, initially in the ground state, with a single photon in the cavity and in the absence of dampening. A

value for $g(\boldsymbol{r})$, for the case of an NV center coupling to a WGM described spatially by $\Psi_{s,n,l,m}(\mathbf{r})$ with mode volume $V_m$, can be estimated by using an expressions for $\gamma_\perp$ given by:

$$\gamma_\perp = \frac{1}{2}\Gamma_{freespace}(\lambda) = \frac{4(\pi e X_{eg})^2}{3\hbar\lambda^3}, \tag{2.5}$$

where $X_{eg}$ is the dipole matrix element for the transition. For a WGM, supported in a 30 micron diameter microsphere with index of refraction 1.46, described by the mode numbers $n$ =1 and $l = m$ = 300 coupled to an NV center ($\gamma_{NV^{-1}} \approx 10$ ns) located just outside of the microsphere surface, the value for $g(\boldsymbol{r})$ is approximately 50 MHz is obtained. A value of 0.2 is used for $|\Psi_{s,n,l,m}(\mathbf{r})|$ just outside of the sphere surface and it is assumed that the dipole is parallel to the field.

The dynamics of this coupled oscillator system can be described through the equations of motion for the atomic dipole $p(t)=<\hat{\sigma}^-(t)>\exp(i\omega_\circ t)$ and cavity field $\alpha(t) = <\hat{a}(t)>\exp(i\omega_\circ t)$, where $\omega_\circ$ is the frequency of the driving field. As mentioned before this analysis is done in the weak excitation regime, which corresponds to $<\sigma_z>$ = -1. In the rotating frame of the driving field, the spontaneous decay of the emitter and the cavity field damping are described by the set of linear equations:

$$\begin{aligned} \dot{p}(t) &= -\gamma(1+i\Delta)p(t) - g^*(\boldsymbol{r})\alpha(t) \\ \dot{\alpha}(t) &= -\kappa(1+i\theta)\alpha(t) - g(\boldsymbol{r})p(t), \end{aligned} \tag{2.6}$$

where decay mechanisms have been introduced. Equation (2.6) has an atomic detuning term $\Delta$ ($\equiv$ $(\omega_a - \omega_0)/\kappa$) and the term $\theta$ ($\equiv$ $(\omega_c - \omega_0)/\gamma$) is the cavity detuning from the laser frequency $\omega_0$. Damping terms have been added to these equations in order to account for the fact that a cavity and atom have a finite lifetime, which is depicted in Fig. 2.3. The cavity decay rate, $\kappa = 2|t|^2/\tau_{roundtrip}$, where t is the reflectivity of the two mirrors and $t_{roundtrip}$ is the time to make a round trip in the cavity. The atomic transition rate for the two-level system is related to the transition lifetime through $\tau_{eg} = \gamma^{-1}$. For certain cavity geometries $\gamma = \gamma_\perp = \gamma_\parallel/2$, including the class of resonator that is being considered in this dissertation [65].

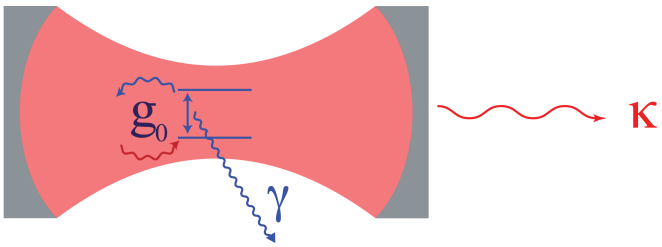


Figure 2.3: A cartoon depicting the relevant rates in cavity quantum electrodynamic systems. The relative size of the atomic, $\gamma$, and cavity, $\kappa$, decay rates as well as the cavity coupling rate, $g$, dictate the dynamics of the system.

With the assumed forms for $\alpha(t)$ and $p(t)$, the eigenvalues $\lambda$ for this system can be determined by solving for the roots of a characteristic equation with the form:

$$y(\lambda) = [\lambda + \kappa(1 + i\theta)][\lambda + \kappa(1 + i\Delta)] + g_0^2. \tag{2.7}$$

For the case of zero detuning the roots are given by the expression:

$$\lambda_{\pm} = \left(\frac{\kappa+\gamma}{2}\right) \pm \sqrt{\left(\frac{\kappa-\gamma}{2}\right)^2 - g_0^2}. \tag{2.8}$$

2.1.1. Weak Coupling Regime Bad-Cavity Limit

The dynamics of this coupled oscillator system depends on the relative size of κ, γ, and $g$. In the weak coupling regime, where $g < (\kappa, \gamma)$, there are two possible situations. With $g^2 << |\kappa - \gamma|/2$, the condition where $\kappa << \gamma$ is called the bad- or broad-cavity limit. If the emitter is driven resonantly the cavity and the emitter dynamics will follow an exponential decay:

$$\begin{aligned} p(t) &\propto e^{-\lambda_- t}\cos\omega_+ t, \\ \alpha(t) &\propto \frac{1}{V_m \kappa}\left(e^{-\lambda_+ t} - e^{-\lambda_- t}\right)\sin\omega_+ t, \end{aligned} \tag{2.9}$$

where:

$$\omega_+ \approx \kappa + \frac{g^2(\omega_c - \omega_a)}{(\omega_c - \omega_a)^2 + \kappa^2}. \tag{2.10}$$

The decay rates with detuning are given by the expression [66]:

$$\begin{aligned} \lambda_- &= \gamma - \frac{g_0^2/\kappa}{\left(\frac{\omega_c - \omega_a}{\kappa}\right)+1}, \\ \lambda_+ &= \kappa + \frac{g_0^2/\kappa}{\left(\frac{\omega_c - \omega_a}{\kappa}\right)+1}. \end{aligned} \tag{2.11}$$

Only terms that were first order in ($g^2/\kappa$) are used in these expressions. The term associated with the cavity decay rate $\lambda_+$ is greater than the emitter decay rate $\lambda_-$. After time scales on the order of $\lambda_+^{-1}$, the dynamics of the emitter still plays a role in the cavity field evolution. After this short period of time, the emitter and the cavity continue to decay exponentially at the same modified rates.

In this regime, the emitter dominates the decay rate and the oscillation frequency of the composite system. The cavity acts to suppress the emitter decay rate for large detuning and enhances the emission near resonance. There is also a shift in the emitter resonance frequency. This shift results in a pulling of the emitter frequency towards the cavity resonance due to an interaction between the two harmonic oscillators. This shift has been described as arising from a perturbation of the free-space mode density by the presence of the cavity mode [67]. All the other cavity resonances are treated as part of the free-space mode density when the emitter is excited directly, in the presence of a cavity, at a frequency near the cavity resonance.

### 2.1.2. Weak Coupling Regime Good-Cavity Limit

With $g^2 << |\kappa - \gamma|/2$ , but in the limit where $\kappa << \gamma$ (called either the good- or narrow-cavity limit) the cavity dynamics are perturbed by the presence of the emitter. However, in this case the cavity field is dictated by the properties of the resonator. The dynamics of this coupled system is described by the equations:

$$p(t) \propto e^{-\lambda_- t} \cos \omega_+ t,$$
$$\alpha(t) \propto \frac{1}{V_m \gamma}\left(e^{-\lambda_+ t} - e^{-\lambda_- t}\right) \sin \omega_- t, \tag{2.12}$$

where:

$$\omega_- \approx \kappa + \frac{g^2(\omega_c - \omega_a)}{(\omega_c - \omega_a)^2 + \gamma^2.} \tag{2.13}$$

The two eigenvalues for the coupled oscillator system are expressed as:

$$\lambda_- = \kappa - \frac{g^2 \gamma}{(\omega_c - \omega_a)^2 + \gamma^2}$$
$$\lambda_+ = \gamma + \frac{g^2 \gamma}{(\omega_c - \omega_a)^2 + \gamma^2.} \tag{2.13}$$

In this picture the dipole moment for the emitter can be thought of as a source of radiation that wants to be released into its environment. The sharp cavity mode "feels" the presence of the dipole that can cause a cavity resonance $\delta\omega_c$ shift of:

$$\delta\omega_c \approx -\kappa(g^2 / 2\kappa\gamma)\frac{\gamma(\omega_c - \omega_a)}{\gamma + (\omega_c - \omega_a)^2}. \tag{2.14}$$

From this perspective the cavity dynamics are being modified by the presence of the atom and the evolution of the field in the cavity has the form of exponential decay. In this scenario, a short period of time after exciting the emitter $\sim\lambda_-^{-1}$ the dynamics for the cavity is purely dependent on the cavity parameters. In the previous case, the cavity dynamics were not solely dependent on the cavity and after the shorter decay time on the order of $\lambda_-^{-1}$ only the emitter influence remained on the cavity. In this latter case, the

dynamics are set by the cavity after short time scales and the power ($\propto|\alpha(t)|^2$) decay rate from the cavity is:

$$\Gamma = 2\left(\kappa - \frac{g^2\gamma}{(\omega_c - \omega_a)^2 + \gamma^2}\right). \tag{2.15}$$

The concept of driving the cavity or emitter resonantly is an important one because it set the perspective of the problem. When the coupling rate is negligible and a laser drives the atom resonantly, the atom mediates the energy for the system and the cavity is influenced by and influences the radiation dynamics of the emitter in a specific way depending on the physical situation; i.e. detuning, decay rates and the alignment between the dipole and cavity field distribution, etc. In the case where the cavity is driven directly, the above equations can be used to describe the system and the roles of the atom and cavity should be reversed in the interpretation. In either case however, the cavity field and atomic state follow an exponential decay.

### 2.1.3. Intermediate Coupling Regime

The range of rates where:

$$\frac{(\kappa - \gamma)^2}{4} < g^2 < \frac{\kappa^2 + \gamma^2}{2}, \tag{2.16}$$

is called the intermediate coupling regime. In this discussion, and the one that follows below describing the strong coupling regime, it will be assumed that the cavity and the emitter frequencies are resonant ($\omega_a = \omega_c = \omega$) with one another. In the over-damped

regime $|\kappa - \gamma| > 2g$, there is exponential decay with rates that are slightly less than their free-space values. This deviation from their free-space values is slightly different for the cavity and the emitter while the oscillation frequencies of the emitter and cavity modes are degenerate. In the under-damped regime $|\kappa - \gamma| < 2g$, the exponential decay rates are again modified, however, the decay rates for the atom-cavity modes are equal but, in this case, the oscillation frequencies are not.

### 2.1.4. Strong Coupling Regime

In the strong coupling regime, where $g > (\kappa, \gamma)$ the dynamics of the coupled system is drastically different from these other cases [68]. The most notable difference is the oscillatory behavior in the emission spectra. The normal modes of the composite system exhibit energy oscillations between the cavity mode of interest and the emitter for time scales on the order of $1/(2g)$ and the single-photon Rabi frequency $2g$ is the maximum rate with which a quanta of excitation can be exchanged between the cavity and the atom. The eigenfunctions describing the atomic dipole and cavity field are expressed as:

$$p(t) \propto \left( \cos\Omega_{Rabi} t + \frac{\kappa - \gamma}{2\Omega_{Rabi}} \sin\Omega_{Rabi} t \right) \cos\omega t \; e^{-\left(\frac{\kappa+\gamma}{2}\right)t}$$

$$\alpha(t) \propto \frac{1}{\Omega_{Rabi} V_m} \left( \sin\omega t \sin\Omega_{Rabi} t \right) \; e^{-\left(\frac{\kappa+\gamma}{2}\right)t}, \tag{2.17}$$

where:

$$\Omega_{Rabi} = \sqrt{g^2 - \left(\frac{\kappa - \gamma}{2}\right)^2}. \tag{2.18}$$

In this case the power emitted by the oscillators is represented by a normal-mode splitting in the frequency domain. This behavior is illustrated in Fig. 2.4a. In the time domain the power emitted by the sources exhibit exponential decay with an oscillatory behavior superimposed on them. This is a result of the coherent exchange of energy between the two oscillators whose power emission as a function of time is out of phase from one another. Figure 2.4b is a plot of this behavior. A major point to be made is that in the strong coupling regime a single photon can be emitted by the atom and then reabsorbed by the atom from the cavity before it leaves the system through some irreversible decay channel.

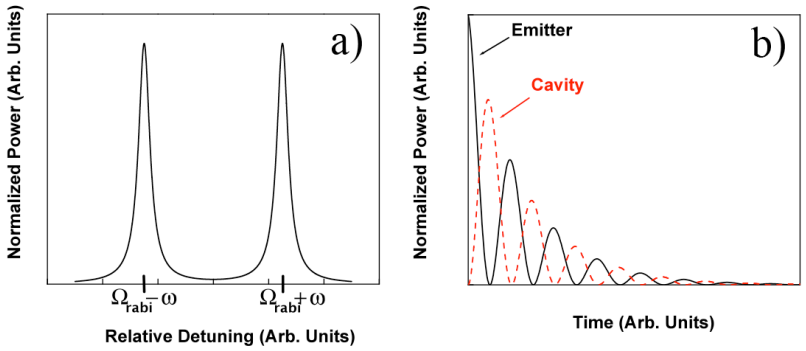


Figure 2.4: Normal mode splitting for the strongly coupled oscillators and ringing in the emission spectrum in the a) frequency or b) time domain.

It is useful to characterize cavity-QED systems in terms of two dimensionless parameters. These parameters describe the sensitivity of the system dynamics in terms of

the gain or loss of a single photon or atom. The critical photon number $\gamma_{critical}$ describes the number of photons it takes to saturate the emitter response by the cavity field is expressed as:

$$\gamma_{critical} = \frac{\gamma^2}{2g_0^2}. \tag{2.19}$$

A similar quantity that describes the sensitivity of the system is the number of strongly coupled atoms that are required to modify the cavity field. This quantity is called the critical atom number:

$$N_{atom} = \frac{2\gamma\kappa}{g_0^2}. \tag{2.20}$$

Amongst the necessary conditions for strong coupling to be observed by a given system design, the critical atom and photon numbers should both be much less than unity. Under such conditions, the introduction or removal of one atom or photon could have profound consequences on the dynamics of the system. This results in a non-classical and nonlinear response of the system to such changes. Typical quantum optical systems, such as lasers or cold atoms, have critical numbers for photons or atoms in the millions. In systems such as these, the dynamics is not perturbed by the removal or addition of a single light or matter quanta.

In an ideal case for the nanopillar-microsphere system under investigation, the values of $\gamma_{critical}$ and $N_{atom}$ approach 0.002 and 0.08, respectively, when $\gamma$ and $\kappa$ set to 10 MHz and when $g$ is set to 50 MHz. Holding $g$ constant, and setting $\gamma$ to 100 MHz and $\kappa$ to 50 MHz, more realistic values for these decay rates are 0.02 and 4 for $\gamma_{critical}$ and $N_{atom}$,

respectively. This value of *g* assumes that the dipole moment for the nitrogen vacancy center optimal was aligned to the field and that the emitter experiences the maximum expected electric field strength possible just outside of the spheres surface. These parameters are possible with the current technology of used to couple microcavities to NV centers in diamond. Many other factors play a role in determining the feasibility of such a composite system and during the course of this research numerous experimental arrangements were pursued and are described in later chapters in this dissertation.

## 2.2. Electromagnetically Induced Transparency Mediated Through a Cavity

Before the advances of the last decade of the 20th century, many photons were used to observe a nonlinear response in an optically dense medium [69, 70, 71, 72]. Electromagnetically induced transparency (EIT) falls into this class of experiments and is a phenomenon where an opaque medium is rendered transparent to a probe beam, in a narrow spectral region, when a control field is applied under the appropriate conditions. The energy level diagram for a lambda system is depicted in Fig. 2.5. In this lambda system the two ground states $|1\rangle$ and $|2\rangle$ are dipole coupled to a common excited state $|3\rangle$. The driving fields for level $|1\rangle$ to $|3\rangle$ and $|2\rangle$ to $|3\rangle$ are at frequencies $\omega_{31}$ (control) and $\omega_{32}$ (probe), respectively. In this case the two levels are both spectrally detuned by the same amount $\Delta$. The decay rates from $|1\rangle$ to $|3\rangle$ and $|2\rangle$ to $|3\rangle$ are $\Gamma_{31}$ and $\Gamma_{32}$, respectively and the $|2\rangle$ to $|1\rangle$ transition is 'dipole forbidden'.

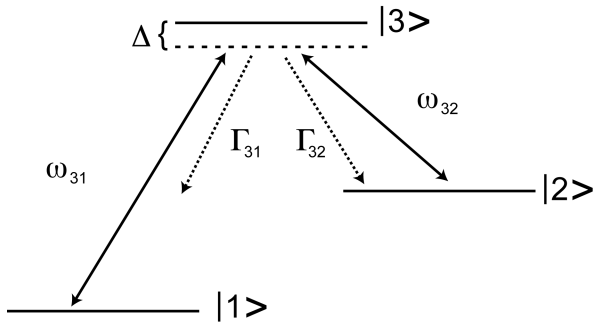


Figure 2.5: An energy level diagram depicting a lambda system.

Under the appropriate conditions, the probe and control field can drive a coherent process resulting in destructive interference between the two pathways leading to a strong modification of the real and imaginary parts of the linear susceptibility, which relate to the refractive and absorptive characteristics of the material, respectively. Specifically, the mediums' absorption of the probe goes towards zero and the refractive index passes through the vacuum value within the $\omega_{31}$ resonance. In the dipole approximation the interaction Hamiltonian between the electric fields, and their respective transitions, takes on the form $\boldsymbol{\mu}\bullet\mathbf{E}$ where $\boldsymbol{\mu}$ represents the dipole moment for the transition and $\mathbf{E}$ represents the electric field at the dipole location with amplitude $E_0$. Under the rotating wave approximation, and in a convenient rotating frame and in this eignestate basis, the Hamiltonian for the system can take on the form:

$$H = \begin{bmatrix} 0 & 0 & \Omega_p \\ 0 & 0 & \Omega_c \\ \Omega_p & \Omega_c & 2\Delta \end{bmatrix}, \tag{2.21}$$

where $\Omega_c(t)$ (= $\boldsymbol{\mu}_{31}\bullet\mathbf{E}_c/\hbar$) and $\Omega_p(t)$ (= $\boldsymbol{\mu}_{32}\bullet\mathbf{E}_p/\hbar$) are the time dependent Rabi frequencies for the control and probe, respectively. The eigenstates of (2.21) are expressed in terms of the bare states of the system. For "adiabatically slow" changes in the time dependent Rabi frequencies one of the three eigenstate in this rotating frame has no contribution from the common excited state:

$$\left|a^0\right\rangle = \cos\theta\left|0\right\rangle - \sin\theta\left|1\right\rangle, \tag{2.22}$$

where the two angles have the relationships:

$$\tan\theta = \frac{\Omega_p}{\Omega_c}, \tag{2.23}$$

If the system evolves into this state the system is said to be in the 'dark state'; there is no population in the leaky excited state and therefore the population "sits" in this configuration. In real systems there are of course other decay mechanisms at play. It is possible for the two lower states to decay; these decay rates must be much smaller than the two other rates, however, in order to trap the population for a considerable amount time. In the case of an NV center, a lambda system can be arranged between a common excited state and either the $m_s = 0$ state and one of the two $m_s = \pm1$ states or both of the $m_s = \pm1$ states. In the latter case the degeneracy between these two sublevels can be lifted with a static magnetic field and the common state may arise from excited state mixing due to strain in the sample. In any case there is a decay channel that takes the $m_s = \pm1$ spin states to the $m_s = 0$ state.

Through a coherent process, two laser beams can adiabatically drive the lambda system into the dark state. This process has been coined STIRAP for stimulated Raman adiabatic passage [73, 74]. Initially, if the system is prepared to be in $|1\rangle$ and a strong control beam is applied to the system, the system starts off in the dark state with $\theta = \pi/2$. As the control beam is turned down and the probe beam is ramped up the population is transferred from $|1\rangle$ to $|2\rangle$ with little to none of the population going into the excited state. The system can also be driven into a superposition of the two states depending the dynamics of the two fields [75]. Fleischhauer, et al., and the references therein, provide a detailed account of these dynamics.

Cavity-QED system can be substituted for one of the electromagnetic fields and reducing the number of photons necessary in that beam in order to induce a nonlinear response from the emitter; the number of emitters can be reduced as well [76, 77, 78, 79, 80]. In the work by Mucke, et al., EIT was demonstrated between an atom that was quasi-permanently trapped inside the cavity, which itself acted as the probe. They continue to demonstrate an increased contrast of the vacuum-Rabi splitting and decreasing transparency for the composite system as atoms are added, one at a time, until a total of seven are loaded into the system.

The following chapters of this dissertation will outline an approach that has developed a robust cavity-QED system that can be used to demonstrate unique dynamics between a NV center in a diamond nanopillar coupled to the whispering gallery modes of a silica microsphere. As will be discussed in detail in chapter six, a mature protocol has been developed to generate, store and manipulate quantum information from the NV

center's electron- and nuclear-spin state. A solid-state system where the matter qubit is stationary moves the concept of quantum networks forward. Like the Fabry-Perot style cavity-atom systems describe in the last two chapters, the composite system described here has many components that have required independent investigation, optimization and integration.

# CHAPTER III

# THEORY OF WHIPSERING GALLERY MODES IN SILICA MICROSPHERES

This chapter outlines the theoretical features of whispering gallery modes (WGMs) supported by silica microspheres that are relevant to the cavity quantum electrodynamics (cavity-QED) experiments conducted in this research. The following section gives a simple geometric picture of the situation where light rays are bound in a microsphere after repeated reflections from total internal reflection. From this vantage point some useful parameters can be deduced that help to describe the field distribution of the WGMs resonances. Section 3.2 approaches the problem using Maxwell's equations. With the appropriate boundary conditions, the analytically solution of the field inside and outside of the microsphere can be derived. In that section, a Helmholtz wave equation approach is taken to describe the solutions for this spherically symmetric case. In the final section of this chapter, a scalar approach gives a more intuitive understanding of the field distribution inside and outside of the microsphere.

## 3.1. Whispering Gallery Modes from a Basic Total Internal Reflection Perspective

Whispering gallery modes can be thought of as a bound state of light that is trapped in an optical resonator due to repeated reflections. Consider a microsphere with radius $a$ and index of refraction $n_s$ that is surrounded by air ($n_{air} \approx 1$). Under the

appropriate conditions, a plane wave of light with wavelength λ can make many round trips within the microresonator structure by repeatedly reflecting off of the sphere-air interface. If the plane wave is incident on the inner surface of the microsphere at an angle greater than the critical angle $\chi_{c,}$ defined as:

$$\chi_c = \sin^{-1}(1/n_s), \tag{3.1}$$

the plane wave will be totally internally reflected. If the microsphere is perfect, every subsequent reflection will be at this same angle $\chi$. When the trip path length is an integer number of the wavelengths, constructive interference occurs, allowing for a build-up of energy. Long-lived states of trapped light formed in the resonator as a result of total internal reflection are called WGMs. In large spheres ($\lambda << a$) the rays of light travel near the surface of the sphere and peregrinate with a path length that is approximately $2\pi a$. In this intuitive picture, we get a tangible number for one of the mode numbers $l$, which is used to describe a WGM, and is given by:

$$l \approx 2\pi a n_s / \lambda. \tag{3.2}$$

At the interface where total internal reflection occurs, there are two components of the transmitted wave vector **k**, the parallel and perpendicular component. For totally internally reflected light, the perpendicular component is imaginary and represents an exponential decay of the electric field with increasing distance from the sphere surface.

## 3.2. Vector Wave Equation Approach to Whispering Gallery Modes

Maxwell's equations, which describe the behavior of electromagnetic fields in materials with permittivity, magnetic permeability and charge conductivity, are the starting point in describing the electric field (**E**) inside of a microsphere [81]. Solving Maxwell's equations for the electric field distribution inside a homogenous dielectric microsphere, with index of refraction $n_s$, can be approached as a vector wave problem. This problem can be cast into the form of a Helmholtz equation, which describes the stationary equations for a monochromatic field, as is expressed as [82]:

$$\nabla^2 \vec{E} + (n_s k)^2 \vec{E} = 0, \tag{3.3}$$

where k = w/c is the wave number in vacuum. In spherically symmetric systems, such as a silica microsphere, the problem of solving the vector equation can be simplified to solving a scalar equation for the wave function $\Psi$:

$$\nabla^2 \Psi + (nk)^2 \Psi = 0. \tag{3.4}$$

This scalar solution can be then be used to reconstruct the electric field distribution [81]. For the sake of simplicity, only the transverse electric (TE) field will be considered below. The electric field of this mode is polarized perpendicular to the plane defined by the WGM. The electric field polarization for the TE, and that of the transverse magnetic (TM), mode is depicted in Fig. 3.1,

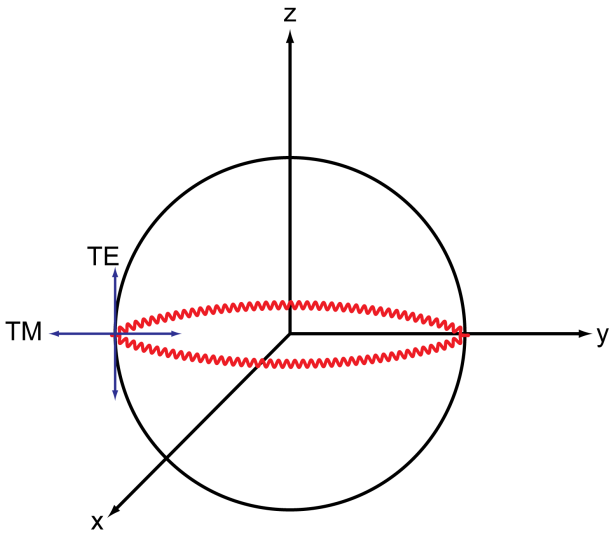


Figure 3.1: The transverse magnetic mode is polarized in the plane of propagation, while the transverse electric mode is polarized perpendicular to this plane.

where the propagation plane is in the x-y plane. In the case of spherical symmetry, the electric field for WGMs with TE and TM polarization can be recovered from the scalar solution $\Psi$ through the pair of transformations:

$$\begin{aligned} &\text{TE modes}: \ \vec{E} = \nabla \times (\vec{r}\Psi) \\ &\text{TM modes}: \ \vec{E} = \nabla \times \nabla \times (\vec{r}\Psi). \end{aligned} \tag{3.5}$$

Solutions to (3.4) are separable, and in a spherical co-ordinate system are described by the equation:

$$\Psi_m^l(r,\theta,\phi) = z_l(n_s kr)\mathrm{Y}_m^l(\theta,\phi), \tag{3.6}$$

where $z_l(n_s kr)$ is a spherical Bessel function of any kind and $\mathrm{Y}^l_{\mathrm{m}}(\theta,\varphi)$ are the spherical harmonic functions [83]. The expression (3.6) for a system consisting of a dielectric

sphere, having an index of refraction $n_s$, with radius $a$ and surrounded by air (n ≈ 1) takes the form:

$$\Psi_m^l(r,\theta,\phi) = \begin{cases} \sum_{l,m} a_{lm} j_l(nkr) \mathrm{Y}_m^l(\theta,\phi), & r \le a \\ \sum_{l,m} b_{lm} h_l^{(1)}(kr) \mathrm{Y}_m^l(\theta,\phi), & r > a \end{cases} \tag{3.7}$$

where $j_l(nkr)$ and $h_l^{(1)}(kr)$ are the spherical Bessel and Hankel functions, respectively, of the first kind. The condition that this solution, and its first derivative, should be continuous across the boundary of the microsphere creates a set of equations:

$$\frac{b_{lm}}{a_{lm}} = \frac{j_l(nkr)}{h_l^{(1)}(kr)}, \tag{3.8}$$

and:

$$\alpha_{lm}(kr) = nlj_{l-1}(nkr) - n(l+1)j_{l+1}(nkr) - \frac{j_l(nkr)}{h_l^{(1)}(kr)}\left[lh_{l-1}^{(1)}(kr) - (l+1)h_{l+1}^{(1)}(kr)\right] = 0. \tag{3.9}$$

These characteristic equations define the eigenmodes, or more specifically the WGMs, supported by a microsphere with diameter $a$ and index of refraction $n_s$. These WGMs are described by the mode numbers $n$, $l$, and $m$ as well as the polarization of the electric field. The mode number $n$ describes the radial distribution of the electric field and takes on integer values. The mode number $l$ corresponds to the total angular momentum of the WGM and $m$, which takes on the values $-l$, … 0 … $+l$, describes the $z$-component of the angular momentum. The angular distribution is characterized by the spherical harmonic function for a given $l$ and $m$. In the case of a perfectly spherical microsphere, modes with different $m$ but with the same $l$ are degenerate. However in

practice, due to the fabrication technique and the presence of a thin fiber stem, the degeneracy of these modes is lifted.

A WGM with a large value of $l$, and with $|m| \approx l$, will support modes with $|l - m| + 1$ lobes in the θ-direction, with a maximum angular extent expressed by the equation:

$$\theta_{\max} = \frac{\pi}{2} + \cos^{-1}(m/l) \tag{3.10}$$

The angular distribution of the electric field about the microsphere surface can be approximated [84]:

$$\mathrm{I}_m^l(\theta,\phi) \propto \left| H_{l-|m|}(l^{1/2}\cos\theta)\sin^m\theta\exp(im\phi)\right|^2, \tag{3.11}$$

where $H_{l-|m|}$ is a Hermite polynomial. The expression given in (3.11) can be used to plot the field intensity across specific cross sections of the microsphere. Figure 3.2 shows the field intensity for three different values of $|l-m|$ in a 30 micron diameter microsphere.

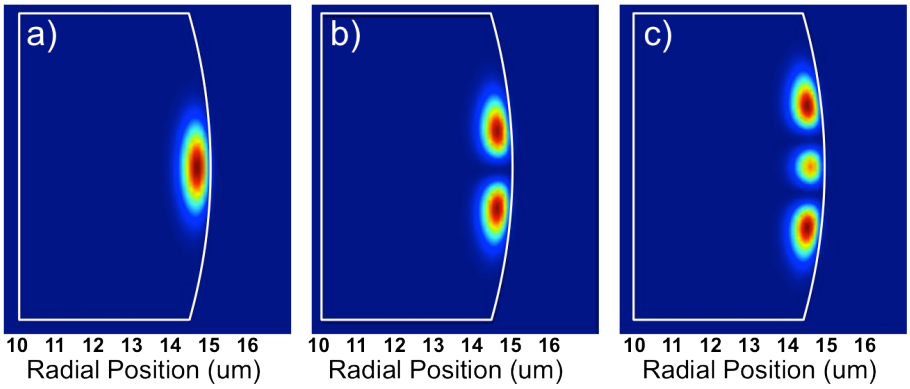


Figure 3.2: False color field intensity distributions for the a) $|l - m| + 1 = 1$ b) $|l - m| + 1 = 2$ and c) $|l - m| + 1 = 3$ modes. In these plots the parameters were as follows: 30 micron sphere diameter, mode wavelength at 637 nm, $l = 210$, $n = 1$ and the index of refraction was 1.45.

As can be seen from Fig. 3.2, these particular modes with a resonance at a wavelength at 637 nm ($l = 210$), are centered near the physical equator of the microsphere ($\theta \approx \pi/2$). Furthermore, the most tightly confined WGMs in the angular direction have $l = |m|$ and as the difference between $l$ and $m$ becomes larger the angular distribution of the electric field increases. For cavity QED studies in general, and in particular with NV centers, the need to couple a quantum emitter to the WGM of a silica microsphere makes it necessary to use the most tightly confined modes. This is due to the fact that the coupling rate between the cavity mode and the emitter is inversely proportional to the square root of the effective mode volume. Thus decreasing the mode volume increases the coupling rate. Figure 3.3 below shows a cross sectional plots for the field intensity distribution along the azimuthal direction for the three plots in Fig. 3.2. Obviously, cavity QED studies should be carried out at wavelengths that correspond to

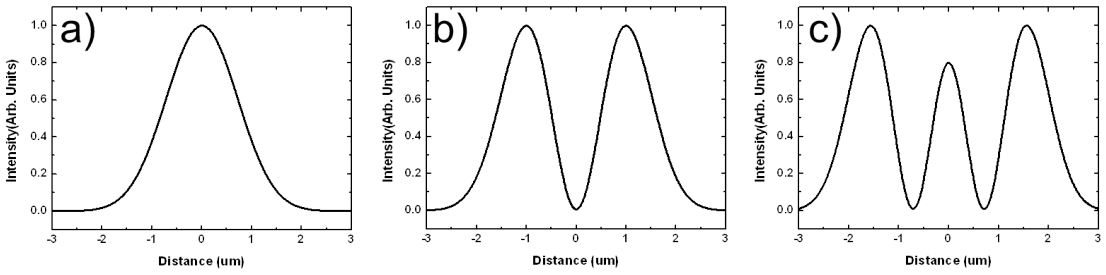


Figure 3.3: Plots depicting cross sections of the electric field intensity distribution for the a) $|l - m| + 1 = 1$ b) $|l - m| + 1 = 2$ and c) $|l - m| + 1 = 3$ modes shown in figure 3.2.

the absorption of the emitter. However, to increase the interaction and observe any cavity enhanced or suppression of the emission from the emitter, WGMs with $l = |m|$ should be used.

Figure 3.3 displays some other points that should be taken into consideration when attempting to couple an emitter to the WGMs of a microsphere. When positioning an emitter relative to a mode of the microsphere, the higher order modes exhibit nodes and antinodes in the field distribution and the anti-nodes can vary in intensity. Aligning a diamond nanopillar to these higher order modes creates the possibility that the nanopillar is interacting with a less intense anti-node or that the pillar could drift into one of the nodes of the field distribution over time. Aligning to the fundamental mode has similar difficulties, but when working with this mode it is easier to observe and understand any variations in their relative position due to the fact that the field intensity distribution is less complicated. Also, the extent of the modes in this angular direction (approximately parallel to the sphere stem in this work) is displayed in these plots. The transverse extent of the fundamental mode is approximately 2 microns at FWHM. For the lobes of the higher order modes, the entire extent can vary from a few microns to tens of microns.

Another feature of WGMs to consider is the depth of penetration within the microsphere interior as a function of the mode number $l$. For the same microsphere the value of $l$ for two WGMs can be the same but the wavelengths will vary. This gives rise to two different WGM structures that results from the rays of light traversing different trajectories. The angle of incidence for one of the modes will be smaller than the other. When the mode is tightly confined to the surface of the sphere (large angles relative to the normal of the sphere) the mode number $l$ can be approximated by (3.1) above. For smaller angles this does not hold and the mode penetrates deeper into the sample and will have to make more round trips to repeat the path length in phase [85].

Furthermore, for a WGM that follows the approximation in (3.1) for the value $l$, while holding the other mode numbers constant, a smaller (larger) value of $l$ ($\lambda$) will result in a larger mode volume. To visualize this, two false color plots of WGMs in a 30 micron diameter microsphere with $n = 1$ are plotted in Fig. 3.4. The difference between these two plots is the mode number $l$, with $l = 210$ for Fig. 3.4a and $l = 100$ for Fig. 3.4b. However, the difference in the field distribution in these plots due to varying $l$ was accomplished by changing the value of $\lambda$ for the simulation from 637 nm to 1270 nm.

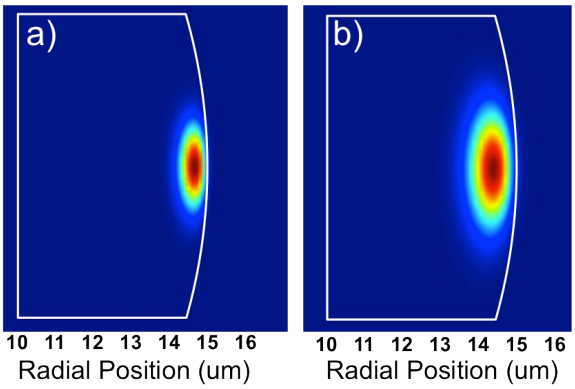


Figure 3.4: False color plots for two whispering gallery modes with $n = 1$ and $l$ (= $m$) set to a) 210 and b) 100.

The electric field extends deeper into the microsphere for smaller values of $l$ (larger values of $\lambda$) and therefore increases the mode volume for this particular cavity resonance. The electric field distribution follows a similar trend for WGMs at the same wavelength but with varying values of $l$ as was mentioned above. The false color plots shown in Fig. 3.5 are of the radial distribution for WGMs with $n = 1$, $n = 2$ and $n = 3$. These plots are calculated by numerically solving for the roots of (3.8) and (3.9) for a particular $l$ (= $m$ = 210) and with their corresponding values for $n$. As can be seen from

these plots, $n$ characterizes the number of antinodes in the electric field along the radial direction.

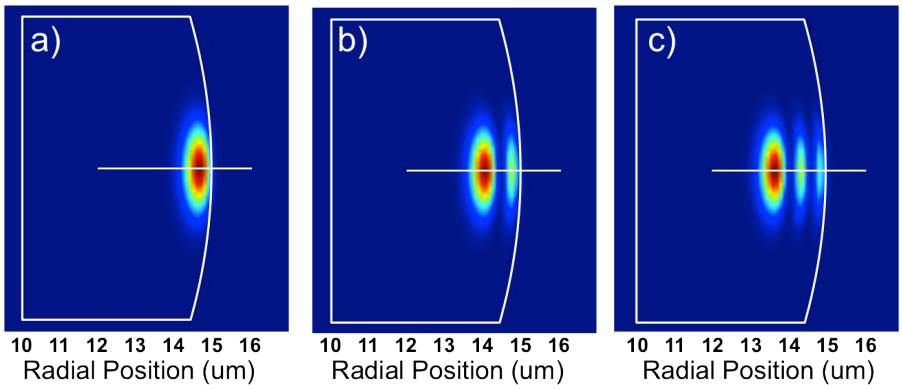


Figure 3.5: False color plots depicting the electric field distribution for a) $n = 1$, b) $n = 2$ and c) $n = 3$ WGMs with the corresponding radial distribution plots for the respective modes. The black line in plots a, b and c are guides for the eyes for the plots in figure 3.6.

## 3.3. A Scalar Perspective on Whispering Gallery Modes

By rewriting the scalar wave equation to resemble Schrödinger's equation, another approach can be taken in order to understand the features of WGMs. This approach might be more intuitive for scientists who have experience quantum mechanics since it approaches the problem from a more familiar perspective. The features of WGMs supported by a dielectric microsphere, with an index of refraction $n_s$ and diameter $a$ (surrounded by air) can be thought of as a quantum mechanical analogy to that of a particle in a potential well. First, rewriting the Helmholtz equation given in (3.4) as:

$$-\nabla^2\psi + k^2(1-n_s^2)\psi = k^2\psi, \tag{3.12}$$

creates a scalar form that resembles Schrödinger's equation [86, 87].

Drawing an analogy between Schrödinger's equation and (3.12), the $k^2(1-n_s^2)$ term can be thought of as the potential energy term of a Hamiltonian describing this system. In this picture the $k^2$ is associated with the energy of the wave function, or energies of the eigenfunctions, that satisfy the characteristic equations given in (3.8) and (3.9). In the case of microspheres with its spherical symmetry, including the discontinuity at the surface in the index of refraction, separation of variables can be used. A differential equation for the radial distribution $R_l(r)$ of the electric field can be written as:

$$-\frac{d^2R_l(r)}{d^2r} + \mathrm{V}_l(r)R_l(r) = k^2R_l(r) \tag{3.13}$$

The potential energy term $\mathrm{V}_l$ (r) can be written as the sum of two parts:

$$V_l(r) = k^2(1-n_s^2(r)) + \frac{l(l+1)}{r^2} \tag{3.14}$$

or in this specific case (3.14) can be written more clearly as:

$$\mathrm{V}_l(r) = \begin{cases} k^2(1-n_s) + \dfrac{l(l+1)}{r^2}, & r<a \\ \dfrac{l(l+1)}{r^2}, & r<a \end{cases} \tag{3.15}$$

In the form presented in (3.15), the first term of the effective radial potential $\mathrm{V}_l(r)$ can be associated with the discontinuity in the index of refraction across the sphere surface. The second term in this expression can be connected with the conservation of

momentum term in the quantum analogue. The potential described by (3.15) is depicted in Fig. 3.6. In this representation, WGMs can be thought of eigenstates that are bound in the potential described by (3.15), with energy $k^2$, where the energy for the mode is less than the potential height at the sphere radius $a$. It should be noted that the shape of the potential well is determined by the energy of the state; i.e., the potential is dependent on the value of $k$.

For a specific $l$, there is a discrete set of WGMs that can live within the depth of the well. For large $l$ values, this range of $k$ is bound by the top and bottom of the well and is defined as:

$$k_{\min} = \frac{(l+0.5)}{n_s a} < k < k_{\max} = \frac{(l+0.5)}{a} \tag{3.16}$$

where, for large $l$ the approximation $l(l+1) \approx (l+1/2)^2$ was used.

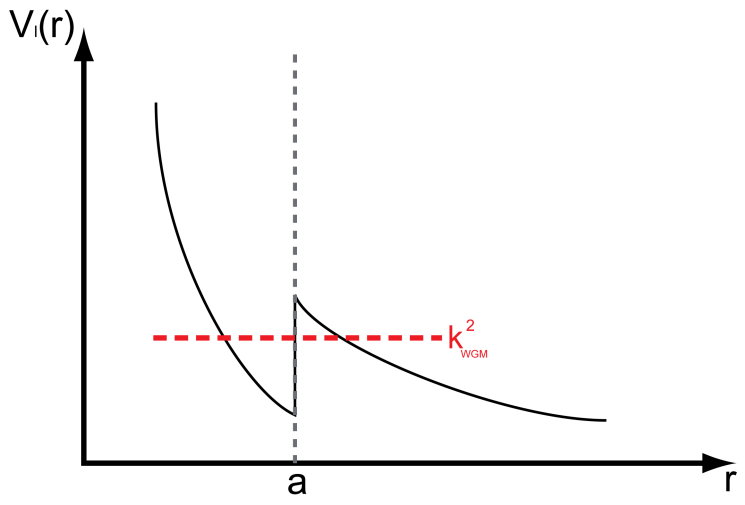


Figure 3.6: The effective potential for a microsphere with radius $a$, and uniform index of refraction $n_s$, surrounded by air.

Cross-sectional plots along the radial direction in a microsphere are shown Fig. 3.7. These plots correspond to the false color images presented in Fig. 3.5. From these plots it is clear that as *n* increases the field intensity maximum shifts towards the center of the sphere and the evanescent field decay length increases. However, the maximum value for the intensity of the evanescent field outside of the sphere decrease as *n* increases.

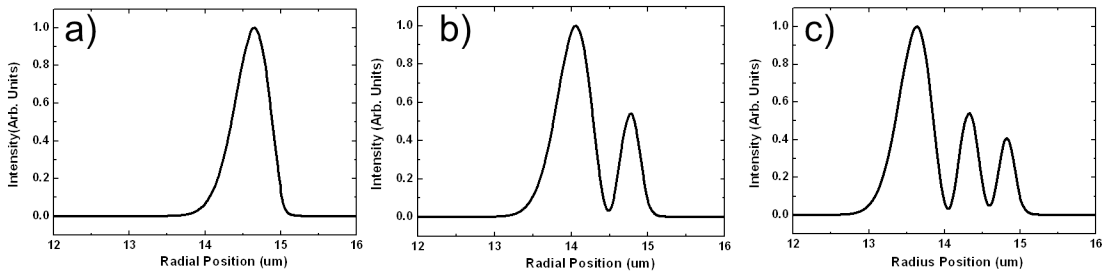


Figure 3.7: Cross sectional plots of the modes shown in figure 2.6 along the sphere radius, in the plane of propagation, for whispering gallery modes with $l = m$ =210 and with a) $n$ =1, b) $n$ =2 and c) $n$ =3.

As was mentioned in the previous section, modes with the same wavelength but with different *l* values have different electric field distributions in the radial direction. Again, this is due to the fact that these modes will have different angles of incidence and therefore require a different number of round trips to complete a single unique path length in phase. A cross sectional plot for the radial distribution shown in Fig. 3.4b is shown in Fig. 3.8. This plot should be compared with a similar plot in Fig. 3.7a for the radial distribution of the electric field intensity for Fig. 3.4a. For the WGM with a larger value of *l* (210 for Fig. 3.7a) the electric field distribution along the radial direction has a non-zero value near 13.7 microns out from the center of the sphere. At the surface of the sphere the field decays exponentially. For the same sphere size and with all of the other

parameters held constant except with *l* set to 100, the electric field has a non-zero value at about 13 microns out from the sphere center.

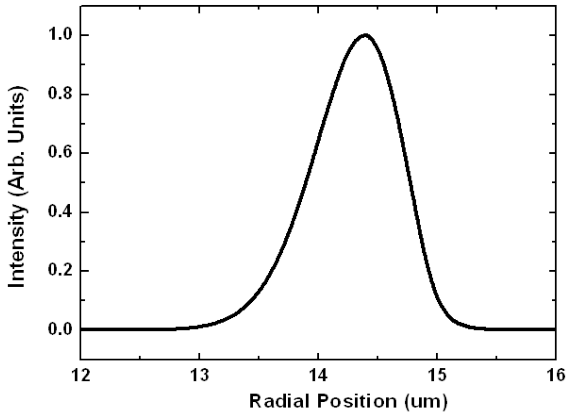


Figure 3.8: The radial distribution for a whispering gallery mode with l and m set to 100 and n set to 1. The electric field distribution spreads deeper into the interior of the microsphere when compared with figure 3.7a.

To easily quantify the decay length of the WGMs outside of the sphere surface, for modes with $n = 1$, the complicated function for the electric field outside of the microsphere can be approximated as [88]:

$$\exp(i\alpha z), \tag{3.17}$$

for large values of *l*, where $\alpha \approx (2\pi/\lambda)(1-n_s^2)^{-1/2}$. In (3.17) $z$ represents the distance from the surface of the sphere in the redial direction. Another expression can be given for the radial extent $\Delta R$, describing the evanescent field decay length from the sphere surface. For a WGM with the radial number *n* and angular mode number *l* (=m), $\Delta R$ can be approximated by the equation [89]:

$$\frac{\Delta R}{a} = 2.2\left[\frac{n-0.25}{n_s X_n^l}\right], \tag{3.18}$$

where $X_n^l$ is the dimensionless size parameter. This size parameter relates the size of the microsphere to the wavelength through the formula:

$$X_n^l = 2\pi a / \lambda. \tag{3.19}$$

Even though the field distribution is complicated by the vector nature of the spherical harmonics, an approximate equation for the mode volume of a particular WGM for a given value of *l* and *m*, when *n* = 1, can be expressed as [90, 91]:

$$V_{WGM} = \frac{\left(\int E^2 d^3 r\right)^2}{\int E^2 E^2 d^3 r} = 3.4\pi^{3/2}\left(\frac{\lambda}{2\pi n_s}\right) l^{11/6}\sqrt{l-m+1}. \tag{3.20}$$

For a WGM at 637 nm, described by the mode numbers *n* = 1 and *l* = *m* = 400, in a silica microsphere ($n_s$ = 1.46) with a diameter of 30 microns, the volume that the mode would occupy is approximately 380 cubic microns. When compared to the total volume of the microsphere, which is approximately 11,500 cubic microns, only 3% of the actual volume of the sphere is occupied by this WGM mode.

# CHAPTER IV

# FABRICATING SILICA MICROSPHERES AND EXCITING WHISPERING GALLERY MODE RESONANCES

Whispering gallery modes (WGMs) supported by silica microsphere structures have been researched extensively in an experimental sense; this chapter discusses the details relevant to the research conducted for this dissertation. The section that follows describes the techniques that were used to fabricate fused silica microspheres in the Wang Lab. The fabrication set-up was simple to use and was arranged in a way to make spheres with diameters less than 100 microns; larger spheres are possible with minor changes to the set-up. The fabrication of deformed microspheres will also be discussed.

Section 4.2 explains the methods used to excite whispering gallery modes in microspheres with an emphasis on the free-space coupling technique. The free-space coupling technique is the primary method with which microspheres are excited in the Wang Lab. A detailed description is given so that other researchers can recreate these techniques with minimal confusion. After that section, the optical spectrum for a single microsphere is displayed and discussed. For the sake of this discussion all of these data were taken within an hour of fabricating the sphere in order to eliminate any irregularities due to quality (Q) factor degradation or frequency shifts.

## 4.1. Fabricating Fused Silica Microspheres

The concept of fabricating a silica microsphere is simple to understand, however, implementing this technique to fabricate a microresonator that can support high-Q WGMs, while maintaining small mode volumes, takes practice, patience and finesse. The procedure begins with a piece of optical fiber that has been vertically suspended for heating with a focused $CO_2$ laser (Synrad 10W). With the aid of a small weight attached to the bottom of the optical fiber a thin fiber taper is drawn out as it melts. Once the thin fiber taper is produced, the tip can be quickly heated with the $CO_2$ laser forming a nearly spherically symmetric microsphere. A spherical shape results from the surface tension in the molten glass. Both the stem and a slight elongation in the vertical direction, due to the pull of gravity, break the spherical symmetry of the microsphere. This basic fabrication concept is depicted in Fig 4.1. However, in practice, care and skill are required to produce a microsphere that has the desired optical and physical properties necessary to conduct cavity QED studies with nitrogen vacancy centers in diamond nanopillars.

To fabricate the desired microsphere system for cavity QED studies, an experimental set-up such as the one shown in Fig. 4.2, was used. In this arrangement, the fiber was mounted to a three dimensional stage allowing for the position of the optical fiber to be controlled independent of the focused laser beam and the imaging system. Furthermore, the fiber was mounted in a rotation stage that enabled it to be accurately positioned. This made it possible to heat the fiber and the microsphere on all sides with

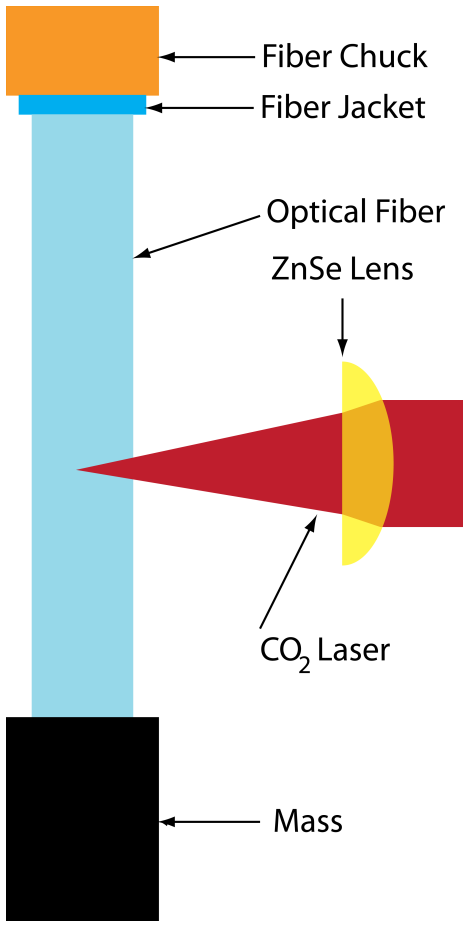


Figure 4.1: A cartoon depicting the basic concept and components used in the fabrication of fused silica microspheres from optical fiber.

the $CO_2$ laser. The $CO_2$ laser output was focused with a 24.5 mm focal length plano-convex ZnSe lens. The position of the ZnSe lens was controlled via a 3D stage and allowed for precise control of the focal position and spot size when heating the fiber. For better control over the amount of laser power focused onto the optical fiber, a 50/50 beam splitter was placed in between the laser output and the focusing lens. Without the beam splitter the laser power required to melt the optical fibers, ranging from 125 to 300 microns in diameter, would have been at the threshold of the $CO_2$ laser, making it difficult to fabricate microspheres under systematic and repeatable conditions.

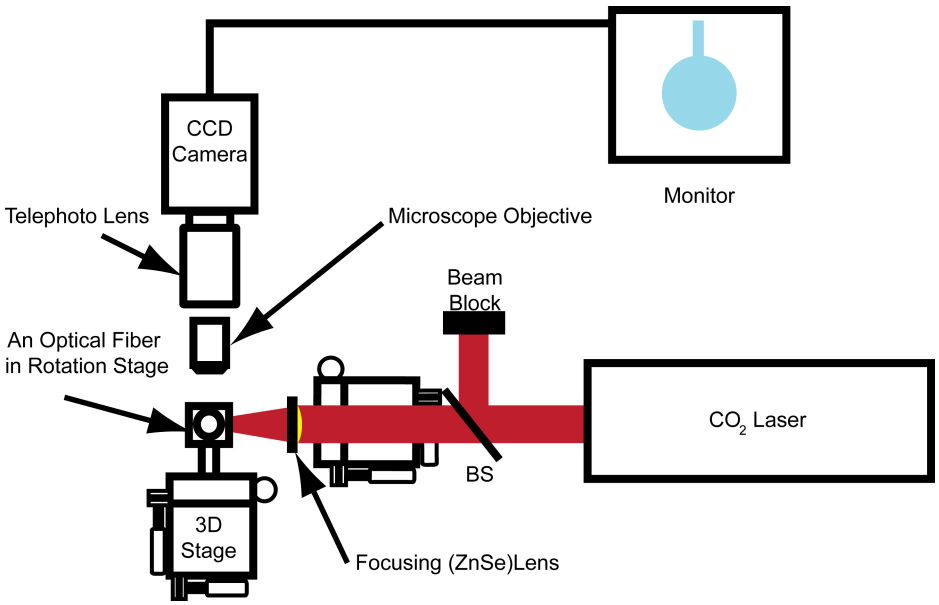


Figure 4.2: A diagram depicting the $CO_2$ laser set-up used to fabricate fused silica microspheres.

In order to monitor the fabrication process, a high magnification microscope objective (Mitutoyo M Plan Apo 100X) and telephoto lens were used to form an image of the fiber on a CCD camera whose output was displayed on a monitor. The apparatus was set-up in a way so that the focus of the imaging arm and the $CO_2$ laser overlap where the fiber is mounted. The fiber could be imaged with either bright field or dark field illumination. During fabrication, backfield illumination was typically used as it produced sharper images of the optical fiber.

The first step taken to fabricate a microsphere was to prepare a piece of optical fiber approximately 30 mm long before it was mounted into a fiber chuck. It was important to choose the appropriate optical fiber and prepare it properly before mounting it into the sphere-making set-up. If there was any contamination in the region of the fiber that was to be used to form the resonator it could be incorporated into the microsphere,

leading to a reduction in the Q-factor of the WGMs or it could have caused a splitting in the Lorentzian lineshape [92, 93]. To prepare the fiber 15 mm of the fiber jacket was stripped away with the appropriate mechanical stripping tool. Next, the cladding of the fiber was cleaned with methanol to remove any particles or residue from its surface.

A multimode fiber (Thorlabs EMT200) was used in this research. This brand of fiber had a high purity silica core that was 200 microns in diameter. It should be noted that this particular fiber was chosen for a number of reasons. First, this particular fiber had a high purity core, which reduced the absorption of light caused by OH- molecules typically found in optical fibers [94, 95]. Second, the cladding could be easily removed with the $CO_2$ laser leaving behind a negligible amount of residue in the vicinity of the fiber where the stem and sphere were to be fabricated. Third, it had a core diameter that made it easy to fabricate microspheres with straight thin stems up to 4 millimeters long. Finally, when optical measurements of the WGMs were made, it was found that this type of fiber could be clamped in such a way that made the system rigid and less susceptible to vibrations.

Once the fiber was stripped and cleaned, it was mounted in a rotation stage and vertically suspended from a 3D stage. This was done by mounting the fiber in a fiber chuck with only 1 to 2 millimeters of the jacket exposed below the face of the chuck. A weight was then attached to the free end of the fiber to help draw out the stem as it was heated with the $CO_2$ laser. The cladding was typically removed with a current of 1.64 Amps, which was a value experimentally determined to only melt the cladding but not melt the glass. With this power setting, the glass surface was cleaned without melting the

glass. The cladding of the fiber was heated on all sides with $CO_2$ laser to remove any contamination on the surface.

When drawing out a thin taper from the fiber, the laser beam was defocused by about 60 microns. This allowed for a slow and consistent melting of a large section of fiber. Using this type of optical fiber and laser focus, a current of approximately 2.0 Amps was applied to the $CO_2$ laser. Ideally, the laser beam was adjusted horizontally towards the fiber until the desired rate of melting and stretching occurred. Once the fiber began drawing out at a smooth and continuous rate, no changes to the beam path were made until the required length of stem was fabricated. At that point the beam was quickly retracted to stop the melting process. After this step had been successfully completed, the unnecessary portion of fiber below the stem was removed with a tightly focused beam. To make a microsphere at the end of this thin piece fiber, a small amount of material was left at the end of the thin stem. The mass of fiber would have a width that was roughly equal to the diameter desired for the microsphere.

After fabricating a thin stem with a mass of fiber at the end, it becomes necessary to position the laser focus in the center of the monitor. This makes the fabrication of spheres easy and is necessary when deforming microspheres with laser pulses. Additionally, this knowledge becomes important when a second stem was to be attached to the bottom of the microsphere, and will be discussed in the next chapter. To determine the beam position, the mass of fiber that was to become a microsphere was slightly above the focus laser focus with it centered in the monitor. Small adjustments to the laser beam position were made horizontally to determine where the most intense heating occurred. The laser would be focused at that point during the remaining steps of the fabrication

procedure. Once this alignment had been achieved horizontally, a spherical shape was achieved by "dunking" the mass of fiber into the laser beam repeatedly.

At this point the laser current was at 1.65 A and the lens was defocused by roughly 35 microns. Time was taken to rotate the fiber during this process so the equatorial plane of the sphere was nearly perpendicular to the sphere stem. If the sphere wasn't rotated during the fabrication process, the optical axis would be tilted from the plane perpendicular to the stem making the excitation of WGMs difficult. The difference in heating and not heating the microsphere from all sides is displayed in Fig. 4.3. Attention should be paid to the sample tilt when bringing a nanostructure into the mode volume of the WGM. Under certain geometries for the physical position of the optical equator, the alignment process can become difficult or impossible. Considerations of the stem tilt should also be made. This is done in order to avoid contacting the sample with

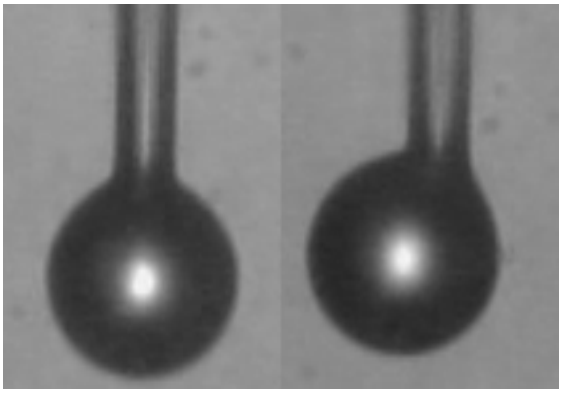

Figure 4.3: An image of a microsphere which was fabricate by heating it with a $CO_2$ laser on a) both and b) only one side. If the optical plane is tilted is too much relative to the sphere stem aligning a WGM to a nanostructure becomes difficult.

the stem before the mode volume of the resonance interacts with the object of interest.

To produce a deformed microsphere two efficient techniques are available to the experimentalist. The first method merges two spheres, roughly half the diameter of the final sphere diameter, together to form a deformed sphere [96]. The amount of deformation can be controlled by repeatedly re-heating the microsphere. The second method utilizes pulses from the $CO_2$ laser to deform the microsphere. For this dissertation, the second method was used to fabricate deformed microspheres. When the sphere was pulsed, a laser current of 1.45 A was typically used. The pulses were applied on both sides of the sphere.

## 4.2. Exciting Whispering Gallery Modes in a Fused Silica Microsphere

To efficiently excite a WGM in a silica microresonator, it was necessary to produce an evanescent field near the surface of the resonator that which was mode-matched to the relevant WGM. There is a number of methods to excite WGMs in a resonator and it is typically accomplished with an optical coupler [97]. The two most common optical couplers used to excite WGMs in microsphere are either a high index prism or a tapered optical fiber. These two methods are illustrated in Fig. 4.4. Figure 4.4a depicts how light can propagate from the prism into the microsphere across a sub-micron gap, via frustrated total internal reflection [90, 98]. By changing the angle of incidence of the light in the prism, different radial modes can be selectively excited.

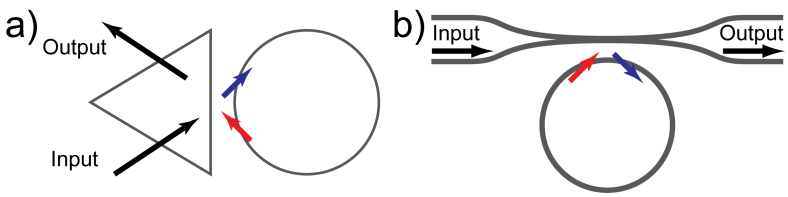


Figure 4.4: Using a) a prism or b) a tapered fiber can be an efficient way to couple light in and out of whispering gallery modes supported by silica microspheres.

Adiabatically tapered fiber can be used as another efficient way to excite WGMs in fused silica microspheres [99]. This general concept is depicted in Fig 4.3b. Tapered fibers were fabricated by stretching both ends of a single mode optical fiber (Newport F-SE), which had a glass core and glass cladding, while it was being heated with a hydrogen torch. The tapered region was typically 10 to 20 millimeters long and at its thinnest point the diameter ranged from one to two micrometers. In the tapered region of the fiber, the glass cladding that surrounds the core becomes negligible and the fundamental mode is guided in the thin silica fiber by the surrounding air. At a wavelength near 637 nm, tapered fibers with diameters less than 2 microns produce a significant evanescent field that extends out into the surrounding air.

For the most tightly confined WGMs in a microsphere, with the lowest radial mode number $n$ =1 and with $l \approx m$, the propagation constant for the mode is :

$$\beta = \frac{kl}{X_{nlm}}, \tag{4.1}$$

where $k$ is the free-space propagation constant, $X_{nlm}$ is the resonant size parameter for the WGM described by the mode numbers $n$, $l$ and $m$. For fiber diameters in the range of 1.4

to 3 microns, the propagation constant of the WGM can correlate to the propagation constant of the tapered fiber via the equation:

$$\beta^2 = (kn_f)^2 - \frac{(2.405)^2}{\rho^2}, \tag{4.2}$$

with less than 1% error. In this equation $n_f$ is the index of refraction for the tapered fiber and $\rho$ is the diameter of the tapered fiber at its thinnest point. Due to the exponential decay of the evanescent field from the surface of the coupler, the gap between the microsphere surface and the coupler should be on the order of half the wavelength of light being used to excite the WGM. With the use of a tapered fiber and under the appropriate conditions nearly one hundred percent of the light from the fiber can be coupled to a WGM resonance [100].

When conducting room temperature experiments with the composite diamond-microsphere system, outside of any special chamber, a tapered fiber was used to couple light into and out of the resonator. However, for low temperature experiments, WGMs were excited with the use of a free-space excitation technique. The coupling efficiency of this method was much less than in the tapered fiber or prism approaches. It was typically on the order of 5 percent. A major benefit of this free-space coupling technique was that no additional element had to be positioned inside of a preservation chamber or in an optical cryostat. The free-space coupling technique utilizes directional escape from slightly deformed microspheres and can be thought of as a time reversal of that process.

When the input laser beam is properly focused and positioned near the surface of the microsphere, at a location where evanescent escape occurs, high-Q optical modes can

be excited [101]. These points occur at regions 45° away from the short or a long axis of the deformed microsphere. This is shown schematically in Fig. 4.5. In order to excite modes efficiently and easily with the free-space technique, the sample should be excited on a specific side and in a specific direction, as is depicted in the figure.

The free-space set-up used for either room temperature or low temperature experiments is shown in Fig. 4.6. Not shown in the figure is the fact that both a tunable diode laser and a dye ring laser, with emission wavelengths at 637 nm, were coupled into the single mode fiber. A portion of the emission from both lasers was picked off and sent to a wavelength meter to monitor the laser frequency and to determine the resonance frequencies of the WGMs. For the purposes of lock-in detection both of these sources were chopped with a mechanical wheel before they were coupled into the fiber.

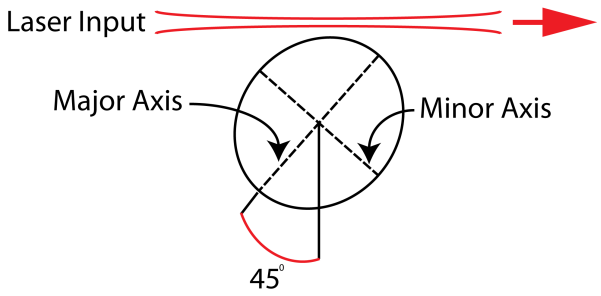


Figure 4.5: The laser input to the microsphere should be focused at points 45° from either the major or minor axis and from a direction, which goes from a shallow to steep angle.

The output from the single mode fiber was directed to a 10X long working distance microscope objective (MITUTOYO M Plan Apo 10X) and was slowly

diverging. To accomplish this, a 5X microscope objective (NEWPORT M-5X) with a clear aperture of 6.0 mm was used as an output coupler from the fiber.

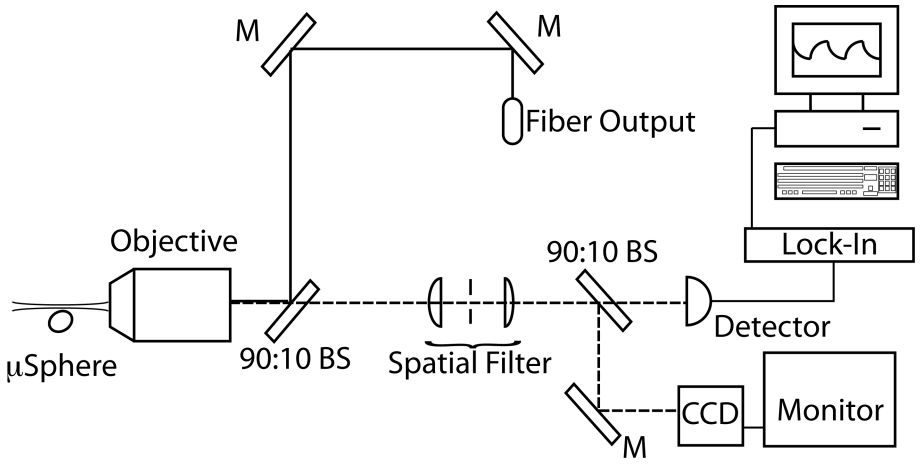


Figure 4.6: The free-space excitation set-up used to excite deformed microspheres at room and cryogenic temperatures. The mechanically chopped laser source comes out of a single mode fiber and is guided by mirrors (M) and a beam splitter (BS) to a microscope objective that couples the lasers to the microsphere. The back emission (dotted line) is directed to a detector and CCD camera after passing through a spatial filter.

The position of the output coupler objective relative to the fiber surface was such that after propagating a distance of 22 cm, the beam went through a focus. This results in a divergent beam that slightly under-fills the 24.0 mm diameter clear aperture of sphere coupling objective. This coupling objective was 68.6 cm away from the focus of the beam. With this type of input beam for the second objective the beam that was focused near the microsphere surface could be better mode matched to the microsphere's far-field emission pattern.

When the microsphere was on resonance, the same microscope objective that couples the tunable laser sources to the resonator also collected the back-emitted light. A

spatial filter was used to reduce the scattered laser light from the microsphere. A 90:10 beam-splitter was used to direct a small fraction of the light to a CCD camera to be able to visually monitor the system while scanning over a WGM resonance. The remaining 90% of the signal is focused onto a silicon diode detector that is connected to a lock-in amplifier. An image of a deformed microsphere when the excitation laser is on and off resonance with a WGM is shown in Figure 4.7. In Fig. 4.7a, the spot on the left was due to the scattering of the focused laser. Figure 4.7b is an image of the microsphere when the laser frequency on resonance with an $l = m$ WGM.

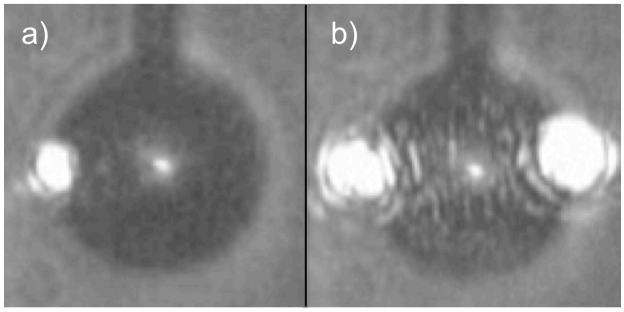


Figure 4.7: A CCD image showing a microsphere with a laser a) off and b) on resonance. There is scattered light on the left hand side of the sphere both on and off resonance.

## 4.3. Deformed Microspheres

An asymmetry in a microsphere not only lifts the degeneracy of optical modes with varying $m$, but under the appropriate degree of deformation other interesting characteristics can be observed. Asymmetric resonators have been studied experimentally and theoretically in many optical systems including cylindrical and

spherical resonators [102, 103]. Some of the initial studies were carried out on aerosol droplets. As the droplets fell, changes in the resonance behavior and emission patterns of these microresonators were studied due to oscillations of the droplets' shape. Unlike spherically symmetric resonators, the ray dynamics inside deformed resonators have been shown to be chaotic and the rays do not conserve the angle of incidence [104]. In the context of this dissertation, the most prominent and interesting feature of deformed microsphere is the directional emission pattern for the radiation that leaks out of the cavity [105]. This feature is a result of refractive escape as the rays orbit around the microsphere; it has also been termed dynamic eclipsing. In a deformed microsphere, the angle of incidence is no longer conserved and as the ray propagates around the equator there are points where the angle of incidence approaches the critical angle. The ray dynamics inside of the microsphere have been theorized from a mixed phase-space perspective, through the Poincare surface of sections, and visualized by plotting the angular position of the ray about the trajectory versus the sine of the angle of incidence. This work showed that there are trajectories in the phase-space, for various modes, with both chaotic and stable trajectories associated with random disconnected points and islands of stability, respectively.

At the points where the angle of incidence approaches (or is less than) the critical angle, refractive escape occurs, resulting in an enhanced directional emission. The onset of directional emission occurs with deviations from a perfectly spherical shape as small as 0.5%. When the deformations of the microsphere is kept below 2%, WGMs can be supported with Qs approaching $10^8$ [106]. The resulting Q for a WGMs that exhibits directional emission varies and depends on the degree of deformation [107]. For large

eccentricities (~0.067) low Q modes are detected in the directional emission pattern [96]. When the eccentricity of the microsphere is less than 0.012, high Q modes are primarily detected. For light rays bound in microsphere with a deformation that is less than 2%, the emission is found to emanate from regions of the sphere which are 45° from a symmetry-axis. These are the points in the phase-space diagram where the angle of incidence approaches the critical angle for the light rays that propagate about the sphere.

This refractive escape results in a directional emission pattern that can be taken advantage of for optical coupling purposes; experimental considerations will be made in the following section. Essentially, if one considers time reversal of this process, at the locations where evanescent escape occurs, it should be possible to efficiently couple light into a resonator by mode matching a laser source at the surface of the sphere. This indeed has been shown with prism coupling, but more importantly with a free space excitation technique [108]. By appropriately focusing light at these points, coupling efficiencies approaching 50% have been obtained. Typically, however, coupling efficiencies are on the order of five to ten percent.

## 4.4. Whispering Gallery Mode Features

Whispering gallery modes supported by fused silica microspheres are most notable for their exceptionally high-Q factors in conjunction with their relatively small mode volumes. The high quality factor of a WGM is mainly a consequence of the low absorption of energy from the high purity optical fibers from which the resonators are fabricated. The fabrication process results in a smooth surface with root-mean-squared

surface fluctuations on the order of 0.3 nm [109]. As defined in the famous text book by D. Jackson, Classical Electrodynamics, the Q is defined as 2π times the energy stored in the cavity divided by the power lost per unit cycle [81]:

$$Q = \omega_0 \frac{Energy\ Stored\ by\ the\ Cavity}{Power\ Lost\ by\ the\ Cavity} = -\omega_0 \frac{U}{dU/dt}, \tag{4.3}$$

where $\omega_0$ is the resonance frequency of the WGM and $U$ is the total energy. This equation can be rewritten in the form of a differential equation whose solution has the form:

$$U(t) = U_0 \exp(-\omega_0 t/Q). \tag{4.4}$$

The total energy in the resonator decreases exponentially as a function of time, with a time constant $\tau$ equal to $Q/\omega_0$. By transforming the expression into the frequency domain, it can be shown that the frequency distribution of the energy in the cavity has a Lorentzian line shape, with full-width-half-maximum of $\Delta\omega = Q/\omega_0$ [110]. The time constant $\tau$ and the decay rate $\kappa$ for a cavity mode can be related through the expression $Q = \omega_0\tau = \omega_0/\kappa$.

The overall Q of a microsphere is the sum of numerous contributing factors:

$$\frac{1}{Q_{total}} = \sum_i \frac{1}{Q_i}. \tag{4.5}$$

When utilizing fused silica microspheres under experimental conditions similar to those in this work, the resulting $Q_{total}$ is limited by the optical absorption $Q_{abs}$ of the fiber used, scattering $Q_{scat}$ from surface contamination within and on the surface of the cavity, the

cavity surface roughness $Q_{s.r.}$ and from moisture $Q_{mois}$ that accumulates on the microsphere surface over time. Quality factors exceeding $10^9$ have been reported for fused silica microspheres in other work [32]. These high Qs are typically lost within a few minutes after being fabricated due to the condensation of water on the surface. By storing microspheres in inert gases, such as helium, a microsphere can be studied for an extensive period of time (read months) with minimal degradation of the Q-factor as a result of water moisture or surface contamination. High purity telecommunication grade fiber, the cladding of which could be easily removed, was used for the experiments. It was important to reduce the amount of cladding and contamination on the fiber core surface before forming the microsphere, as this material could be incorporated into the microsphere itself. When conducting experiments at liquid helium temperatures, it was important to use research grade helium (99.9999% He) gas in the sample space to prevent the condensation of "ice" on the microsphere from other gases that freeze out at liquid helium temperatures.

Enlarging the size of the cavity can increase the Q of a microsphere. However, increasing the size of a microsphere also increases the mode volume of the WGMs. This would decrease the interaction strength of the mode with the emitter. The finesse of a cavity is a unit-less measure of the cavities ability to store light. It takes into consideration both the cavity length (volume) and linewidth. The finesse $F$ of a cavity is related to the free spectral range (FSR) of a cavity through the expression [111]:

$$F = \frac{FSR}{\delta\nu}, \tag{4.6}$$

where $\delta\nu$ is $\omega/2\pi$. The FSR is a measure of the distance, in either frequency- or wavelength-space, between two consecutive WGMs in a cavity with the same value of $l$. In terms of WGMs in a microsphere with radius $a$, the frequency and wavelength representations of the FSR can be expressed as $c/(n_s\, a)$ and $\lambda_c^2/(2\,\pi\, n_s\, a)$, respectively. For a resonator with a diameter of 30 microns at a wavelength of 637 nm the FSR would be approximately 2.17 THz or 2.94 nm. As mentioned before, due to the method with which these optical resonators are fabricated there is a slight deformation in the equatorial plane perpendicular to the stem. This lifts the degeneracy of modes with varying $m$ and the spacing of these modes is on the order of a few to tens of gigahertz.

The lifting of this degeneracy for WGMs with different $m$, but with the same $n$ and $l$ values, as a result of a slight deformation in the microsphere causes a variation in the path length for these modes. An expression, to first order, relating the frequency shift $\Delta\omega$ of various $m$ modes, within same $n$ and $l$ family, to the ellipticity $\varepsilon$ of the cavity is given by [88]:

$$\frac{\Delta\omega}{\omega} = \pm\frac{\varepsilon^2(l^2 - m^2)}{4l^2} \tag{4.7}$$

In this expression the plus sign refers to an increase in frequency due to a flattening of the sphere at the poles. The minus sign represents a decrease in the resonance frequency resulting from a deformation that can be imagined as a stretching of the microsphere from the poles. By measuring the FSR and the mode spacing between various $m$ modes, it is possible to accurately measure the size of the microsphere and the amount of deformation in the sphere as a result of unintentional or intentional deformation of the microresonator.

## 4.5. Excitation Spectrum of Whispering Gallery Modes

The excitation spectrum for WGMs supported in a fused silica microsphere is illustrated in this section. The modes are excited with the free-space excitation technique described in the previous section. The data in this section represent the optical features of WGMs supported in microspheres fabricated for this dissertation. All of these data below were taken from the same sphere, within an hour of fabrication, under ambient conditions outside of an isolation chamber. If measurements of the same sphere were to be made hours or days later, the spectrum would exhibit completely different features. Firstly, the quality factor for the WGMs would degrade quickly due to accumulation of water moisture [112]. The Q would then continue to degrade at a slower rate over time. This was generally the case, unless serious mishandling of the microsphere was to occur such as dust falling on the sphere or from bringing the sphere in contact with a dirty sample surface. Placing the microresonator in a chamber with high purity helium gas is an ideal solution for long-term measurements.

In such a chamber, and under ambient conditions, it was possible to use the same sphere for optical studies for weeks, or even months, if the apparatus containing the sphere is properly operated. Changes to the WGMs structure can still occur even if it were preserved in some type of chamber. The most notable change was the slight shift in the resonance frequency of the WGMs as a result of temperature fluctuations of the microsphere. The temperature dependence of the resonance frequency will be discussed in section 4.4. There can also be a slight shift in the spacing between modes with the same $n$ and $l$ value but with varying $m$ due to a temperature change [113]. This shift is

negligible at room temperature and is set by the initial deformation of the sphere during the fabrication process. However, in order to mitigate these inevitable shifts, the data below originates from the same sphere all within an hour of its fabrication as was mentioned above.

The deformed microsphere was made with the same telecommunications grade fiber and fabrication technique mentioned in section 4.1. The sphere had a 35 micron diameter. The stem was one millimeter long, with a slight angle from the vertical, and it had a 10 micron diameter at the location where it joined the sphere. Initially, finding WGMs in a microsphere is accomplished by conducting a coarse scan with the tunable diode laser. This coarse tuning is achieved with the aid of a movable grating in the laser diode head. With the grating the emission wavelength of the laser can be tuned over many nanometers.

Figure 4.8 below shows the coarse scan spectrum for the microsphere described above. The scan rate was 0.04 nm per second. Displayed here is the family of modes associated with two different $l$ values for this particular microsphere at these wavelengths. At this wavelength, a microsphere with a 35 micron diameter has a theoretical free spectral range (FSR) of 2.68 nm. The experimental value for the FSR was measure to be 2.64 nm. The data acquired for these scans were taken after the coupling to the modes with $l \approx m$ was optimized. This is evident from the fact that the WGM intensity measured for lower order modes is greater than that for the higher order modes. For the case of this microsphere, within a family (same $n$ and $l$ value) these higher order modes are found at wavelengths that are longer wavelengths than the lower order modes.

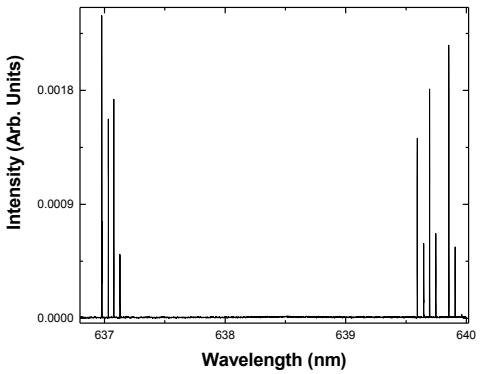


Figure 4.8: This plot shows a coarse scan over 3.5 nm. The free spectral range of the microsphere is 2.64 nm.

With a finer frequency scan, higher resolution data can be obtained. This can be accomplished by applying a smooth DC voltage sweep across a piezo in the laser head. When the scan range is centered on the first three modes in the family ($l = m$, $l = m + 1$ and $l = m + 2$) the WGM structure can be studied in more detail. Figure 4.9 displays such a scan for the second family (higher wavelength) in Fig. 4.8 above. The spacing between these modes is 24.4 GHz for the first pair (left most) and 21.3 GHz and second pair of modes (right pair).

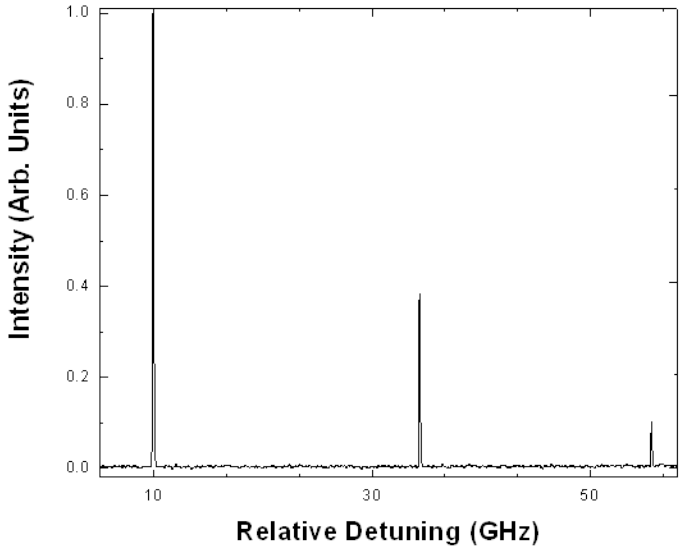


Figure 4.9: Data showing a higher resolution scan of the first three modes in this microsphere.

Figure 4.10a shows the data obtained when the diode laser was scanned as slow as possible across the $l = m$ resonance. From this plot, a linewidth of 19 MHz can be inferred. To obtain more data points, the dye ring laser was used to excite this same mode and is shown in Fig. 4.10b. This mode had a linewidth, as was determined from this laser, of 19 MHz as well. However, for sharper features the ring laser is necessary to acquire enough data points to accurately measure the linewidth of the cavity resonance. The corresponding Q value for this mode is $2.5 \times 10^7$. The Q for the sphere did not change for the entire hour while the data for this section was being acquired.

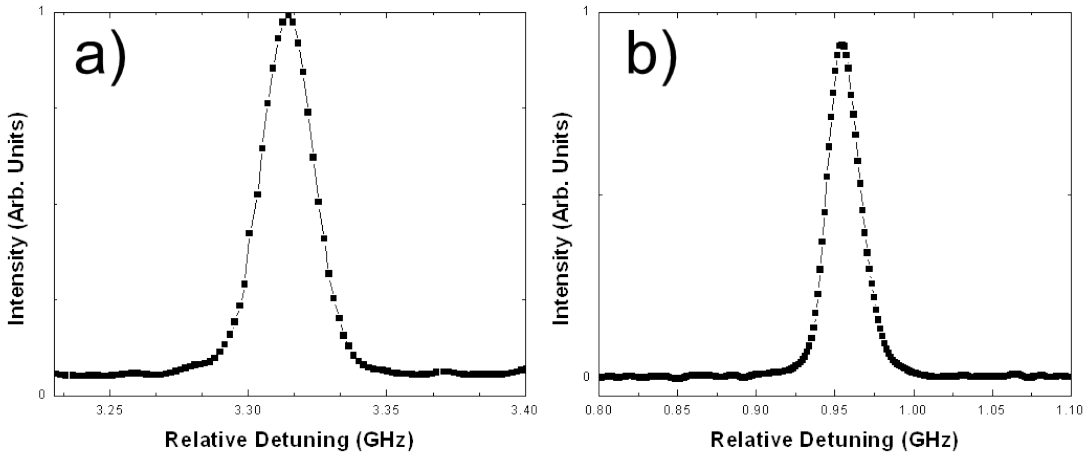


Figure 4.10: Higher resolution scans of the fundamental mode with the a) diode and b) dye laser.

# CHAPTER V

# EXTENDED EVANESCENT FIELD LENGTH AND TUNING CAVITY RESONANCES IN DEFORMED MICROSPHERES

This chapter describes two novel approaches developed to overcome some of the limitations of fused silica microspheres used in cavity quantum electrodynamics (cavity-QED) studies. The following section discusses a study of the evanescent field decay length at various points on a deformed microsphere. The evanescent field decay length of a deformed microsphere was up to four times longer at locations where refractive escape occurs when compared to the symmetry axis of a microsphere. These are the same regions that can be used for free-space coupling.

Section 5.2 discusses another method developed during this dissertation to overcome another disadvantage in using microspheres for cavity-QED. This second issue relates to the fact that there was no way to control the cavity resonance frequency during the microsphere fabrication process. Therefore, some method is required to tune the cavity resonances without reducing the quality (Q) factor of the resonator. By stretching the stems of a deformed double-stemmed microsphere, (DDSS) the resonance frequency of the whispering gallery modes (WGMs) could be tuned at liquid helium temperatures and in a way that was compatible with the rest of the experimental requirements.

## 5.1. Extended Evanescent Field Decay Length in Deformed Microspheres

As was discussed in section 4.3, the angle of incidence for a light ray trapped in a deformed microsphere varies from region to region as it reflects off of the interior of the structure. At specific regions along the ray trajectory the angle of incidence approaches the critical angle. The evanescent field decay length $l_e$ formed at the interface of two materials, as a result of total internal reflection, for a plane wave at a wavelength $\lambda$ and with and incident at angle $\chi$ relative to the surface normal can be expressed as [114]:

$$\frac{1}{l_e} = \frac{2\pi}{\lambda}\sqrt{\frac{\sin^2\chi}{\sin^2\chi_c} - 1}. \tag{5.1}$$

In this scenario, the medium with the higher index has a critical angle $\chi_c$. As can be seen from (5.1), as the angle of incidence approaches the critical angle, decay length approaches infinity. Since the angle of incidences is not conserved in a deformed sphere the evanescent field decay length will vary from position to position as it propagates along its orbit in the optical plane of the sphere. The decay length at regions where the angle of incidence approaches the critical angle were compared to axisymmetric regions of a deformed microsphere as is shown if Fig. 5.1. This study was performed on a deformed microsphere with the use of a tapered fiber probe. The probe was positioned in the equatorial plane of the sphere and was translated at normal incidence to the sphere surface with the aid of a piezo-electric actuator.

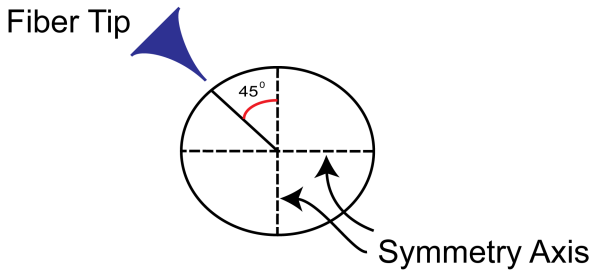


Figure 5.1: The evanescent field decay length of a deformed microsphere was probed with a fiber tip.

The fiber tip served as a scattering source when it was within the evanescent field of the mode. This approach was modeled after a previous high-spatial-resolution study of WMGs in silica [115]. In the work by Menezes, et al., a homebuilt near-field scanning optical microscope was developed to probe the spatial properties of WGMs in silica microspheres with 100 nm diameter fiber tips. Their set-up was successfully used to experimentally map out the intensity distribution of WGMs with various mode distributions with a spatial resolution that was on the order of $\lambda/(2n_s)$. In the case of the work presented in this section, the fiber tip simply acted as a scattering source that resulted in a degradation of the optical Q-factor.

The diameter of the fiber was approximately 1 micron. The fiber tip was fabricated by etching an optical fiber in a 1:20 buffered oxide solution [116]. In order to have precise control of the gap between the fiber and the sphere surface, the probe was mounted on a 3D piezoelectric stage. The microsphere was excited with the free-space coupling technique mentioned in chapter four. The probe station was mounted on a rail that could be rotated. The rotation point was below the microsphere; this allowed the angular position of the tip to be controlled relative to the surface of the resonator. The emission intensity and linewidth of the WGM was monitored as a function of the fiber tip

position relative to the surface of the sphere. The sequence of measurements started with the fiber tip in contact with the surface of the sphere and was then pulled away. Once the linewidth of the WGM was recorded at each of these positions the corresponding Q-factor could be calculated.

The measured Q-factor of the deformed microsphere as a function of the tip-sphere distance is shown in Fig. 5.2. The data in this plot was taken at two different points along the ray trajectory. The data corresponding to the region of the sphere along a symmetry axis are displayed in open circles. It should be noted that at these locations the evanescent field decay length was found to be insensitive to the deformation. With the aid of this location, the position 45 degrees from a symmetry axis could be found. The data collected at this point is depicted in Fig. 5.2a by the filled square labels. Figure 5.1b shows extended data for a non-axisymmetric location, the lines are just guides for the eye.

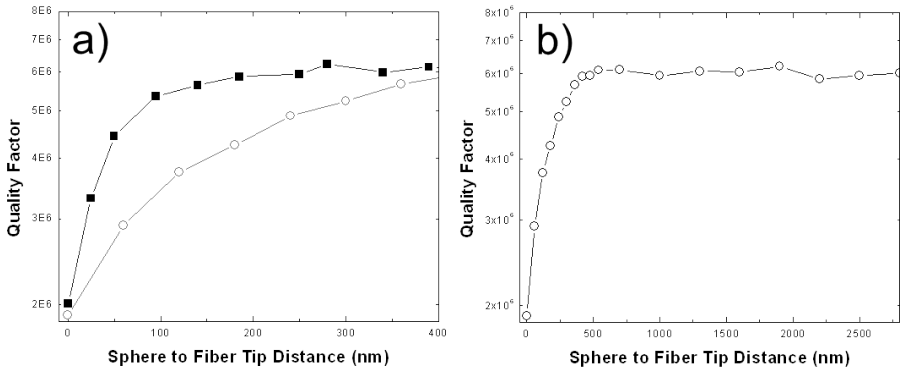


Figure 5.2: a) Data showing the quality factor spoiling at a symmetry point (open circles) and 45 degrees from a symmetry axis (filled boxes) for a deformed microsphere. b) An extended data set taken from the anti-symmetric point of the microsphere.

It was experimentally determined that at a symmetry point of a deformed microsphere, the scattering induced Q-spoiling ended approximately 100 nm from the samples surface. This agreed well with the theoretical predicted value given by (5.1) for the evanescent field decay length, at a wavelength of 637 nm, for a non-deformed microsphere for a WGM with $n = 1$ and $l = m$. However, at a point 45 degrees away from a symmetry axis, the Q-spoiling caused by the presence of the fiber tip ended at a distance 400 nm away from the microsphere surface, for the same cavity resonance. This was nearly a four-fold increase in the evanescent field decay length when compared to a point near a symmetry axis. Such an increase in the evanescent field decay rate is significant for cavity-QED studies because it allows for the coupling to quantum emitters located deeper beneath a sample surface. Furthermore, if a given quantum emitter positioned were to be below the surface of a substrate, an enhanced decay length could be used to increase the interaction strength of the WGM and the emitters dipole.

## 5.2. Tuning the Resonance Frequency of Whispering Gallery Mode

This section discusses another novel approach that was developed over the course of this research. The technique discussed in this section enables the resonance frequency of WGMs to be tuned over a broad range, with high precision and at cryogenic temperatures. The need for WGM tuning results from the fact that it is necessary to match the cavity resonance with the optical dipole transition of a nitrogen vacancy (NV) center. When fabricating microspheres, it is not possible to control the resonance frequency of the WGM. Therefore, it is necessary to have the ability to tune the optical

resonance, with a resolution that is comparable to the linewidth of the WGM, after a microsphere is fabricated.

In addition to the resolution requirements, the tuning range should be a significant fraction of the cavity free spectral range. The need for broad tuning range capabilities is a result of large environmentally induced variations in the optical transition frequencies of NV centers in diamond. Previous experimental techniques have been developed to tune the WGM resonances of silica microspheres at room temperature [117, 118]. In these studies, mechanically stretching or compressing the microsphere with a piezoelectric transducer resulted in a shift in the resonance frequency of a WGM.

Since cavity-QED studies with NV centers must be conducted at liquid helium temperatures, the tuning of the WGM resonance frequencies should be compatible with these harsh environmental conditions. These previous methods were not successful at tuning the resonance frequency of a WGM at cryogenic temperatures, due to the fact that the expansion/contraction range of piezoelectric materials decreases at cryogenic temperatures. To overcome this obstacle, a commercially available piezo-driven nano-positioner (Attocube Systems, model ANPz51) was used to mechanically stretch the two stems of a deformed double-stemmed microsphere system (DDSS).

Deformed double-stemmed microspheres can be fabricated by attaching a long thin stem to the bottom of a single stemmed microsphere. More specifically, DDSSs were fabricated by placing a second stem in contact with the bottom of a microsphere and then pulsing the two with a $CO_2$ laser. During this process the second stem is attached to the sphere as well as deforming the microsphere for free-space excitation. Typically the

first pulse deformed the sphere and attached the bottom stem to the sphere. The sphere was then rotated by 180° and pulsed again. The second pulse deformed the other side of the sphere, but more importantly, it secured the second stem to the microsphere. Figure 5.3 is an image of DDSS with a 40 micron diameter.

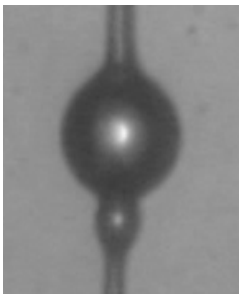

Figure 5.3: An image of a 40 micron diameter deformed double-stemmed microsphere.

Once the DDSS was fabricated it could be optically characterized. If the resonator did not show optical modes, or if it did not display the desired optical characteristics, it was repulsed a number of times before a new DDSS was to be fabricated. Repulsing the DDSS a few more times could shift the WGMs while maintaining relatively high-Q resonances. The direction and amount of the shift was not possible to control, but it was worth trying since it required considerable less time compared to making a whole new DDSS. With regard to a single stemmed microsphere, repulsing the sphere a number of times was possible before fabricating a new sphere as well.

The DDSS could be stretched with the two modes of an Attocube positioner, which allow for the mechanical displacement of samples with sub-nanometer resolution,

over millimeter long travel ranges, at cryogenic temperatures [119, 120]. With the model used in our experiments, the slip-stick motion of the positioner could generate a total mechanical displacement of 2.5 mm. The second mode used a DC voltage offset to expand and contract a piezo element inside the positioner. This allowed for mechanical displacements with nanometer resolution.

Another criterion for the tuning scheme, in the context of the composite system, is that the method used to tune the resonance should not inhibit the ability to approach the microsphere surface with a diamond nanopillar etched from a bulk sample. To avoid the stems touching the sample surface before the mode could be interfaced with a diamond nanopillar, the stems of the DDSS were approximately 3mm long. An added benefit of having the long thin stems for the DDSS was the durability of the system. Deformed double-stemmed microspheres with short thin stems were found to be brittle and tended to break easily when mounting them to the nano-positioner.

To study the feasibility of this approach the tuning system was tested in a helium flow optical cryostat with the DDSS cooled to 10 K. The system had a temperature stability of 0.1 K. The resonance frequency shift of a 40 micron diameter DDSS was measured with the free-space excitation technique at a wavelength near 637 nm. For the data presented in this section, a single tightly confined ($l = m$) WGM with a linewidth of 65 MHz was monitored. Figure 5.4 shows the experimental data obtained when the WGM resonance was shifted with the use of the long-range step tuning method.

When using the step tuning procedure in this experiment, the nano-positioner was operated in the slip-stick (step) mode, with an applied voltage of 25 volts per step. Due

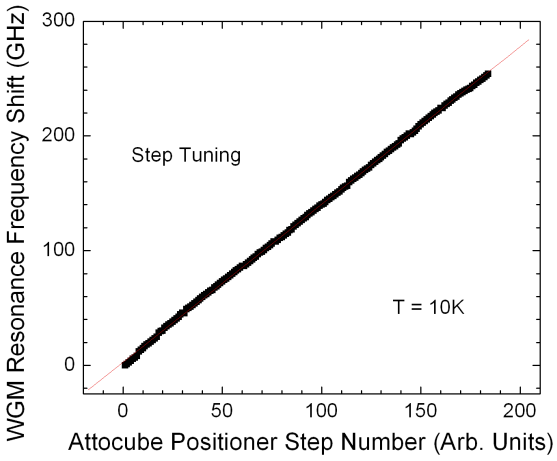


Figure 5.4: Step tuning of a whispering gallery mode in a silica microsphere at 10 K. The nano-positioner was operated in step mode with a 25 V step size.

to the broad tuning range, the WGM resonance was measured with a tunable diode laser. A total of 183 steps were taken to achieve an overall resonance shift of 250 GHz. A total WGM resonance frequency shift that was greater than 450GHz was achieved before the DDSS snapped. This was accomplished with a total of 329 steps of the nano-positioner. For this particular mode and under these experimental conditions, the coarse tuning method had an average step size of 1.37 GHz.

Figures 5.5a and Fig. 5.5b shows the experimental results when this same WGM was tuned with the Attocube positioner in the DC-offset mode. These results were obtained after the resonance frequency of the WGM was shifted over 100 GHz with the step tuning approach. During this fine mechanical tuning, the WGM resonance was measured with a tunable dye ring laser. In Fig. 5.5a, a 10 V increment in the DC offset was used. This resulted in an approximate frequency shift of 500 MHz per step. Figure

5.5b had 1 V increments applied to the DC offset. This resulted in an approximate frequency shift of 50 MHz per step.

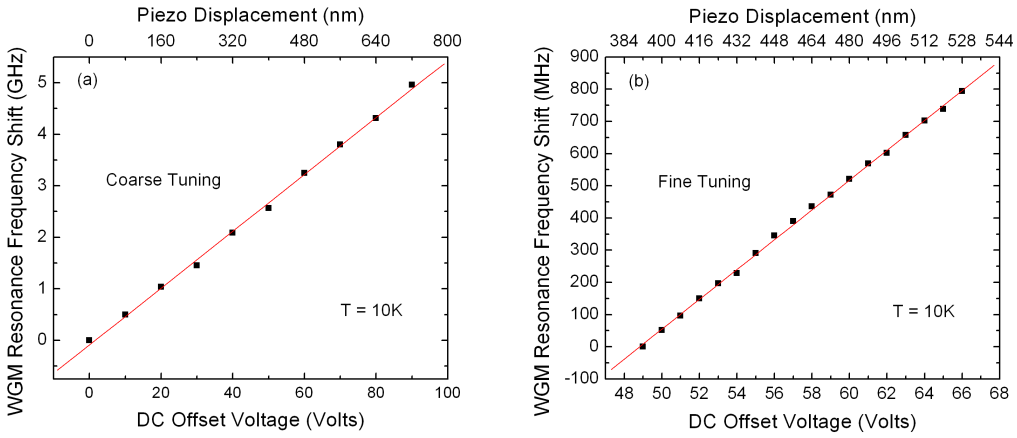


Figure 5.5: Tuning of a whispering gallery mode in a silica microsphere at 10 K with the DC offset step size of the nano-positioner set to a) 10 V and b) 1 V.

In order to achieve the finest frequency shift of the WGM resonance, the DC-offset increment step size of the nano-positioner was reduced to 0.1 V. The resulting frequency shift for the WGM resonance was less than 10 MHz as can be seen from Fig. 5.6. It should be noted that this was accomplished with the use of the Attocube controller. Smaller step sizes in the frequency shift could possibly be achieved with a higher resolution external voltage source. It was found that the coarse and fine tuning processes were reversible and there was little "backlash" in shifting the resonance frequency back to a previous value. Furthermore, the clamping and stretching of the two stems did not alter the Q-factor of the WGM.

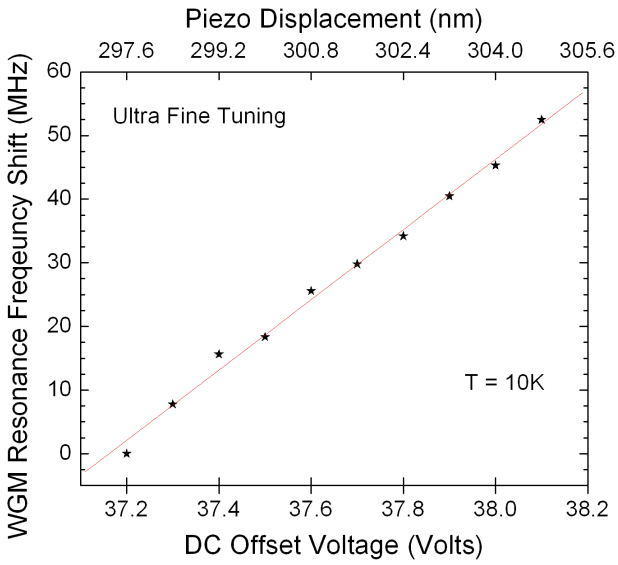


Figure 5.6: Tuning of a whispering gallery mode in a silica microsphere at 10 K with the DC offset step size of the nano-positioner set to 0.1 V.

The frequency shift of a WGM resonance, $\Delta\nu$, induced by stretching the two poles of a microsphere can be attributed to two factors. One contributing factor is due to the change in the geometrical shape of the resonator and the other results from a modification in the index of refractive for fused silica. As was shown in studies previously referenced, the frequency shift due to the index change is small compared to the change in the optical path-length. To lowest order the resonance frequency shift, $\Delta\nu$, can be shown to be:

$$\Delta\nu = -\frac{\Delta d}{d}\nu, \tag{5.2}$$

where $\Delta d$ is the strain-induced increase in the microsphere diameter. The linear slope shown in Fig. 5.4, Fig. 5.5a, Fig. 5.5b, and Fig. 5.6 indicate that the strain-induced change in the sphere diameter was linearly proportional to the mechanical displacement

of the nano-positioner. Using (5.2) and the experimentally observed slopes, an experimentally determined effective Poisson ratio for the DDSS system, $\Delta d/\Delta z$, was found to be 0.0005. Here $\Delta z$ is the mechanical displacement of the nano-positioner. For comparison, the Poisson ratio for fused silica at room temperature is 0.17. It is thought that the use of long and thin fiber stems greatly reduces the effective Poisson ratio of the DDSS system, enabling a more precise mechanical control of the sphere diameter and thus the frequency of the WGM resonance.

With a WGM resonance frequency of 470957 GHz in a 40 micron diameter microsphere, a frequency shift of 10 MHz corresponded to a change in the sphere diameter of 0.85 pm; the stretching of the silica microsphere enabled the for reproducible and continuous tuning of the WGM resonance with a resolution better than 10 MHz. The ratio of the frequency shift over the mechanical displacement, $\Delta v/\Delta z$, for the DDSS used in this study was 6 MHz/nm. This ratio is considerably smaller than the ratio of 100 MHz/nm found in earlier experimental studies where the systems featured short and thick fiber stems.

A number of advantages result from having a smaller resonance frequency shift to displacement ratio, which is a consequence of the systems effective-Poisson ratio. First, a frequency tuning on the order of 10 MHz was realized with sub-nanometer, rather than picometer, mechanical displacements of the positioner. Secondly, fluctuations in the mechanical system from environmental (helium gas flow, vibrations, etc.) lead to comparatively small fluctuations in the frequency of the WGM resonance during operation.

## 5.3. Other Notable Tuning Methods

There are other methods for changing the size and shape of a microsphere to tune the resonance frequencies of the WGMs. One approach is to chemically etch the sphere with a dilute solution of hydrofluoric (HF) acid [121]. In the work by White, et. al., microspheres with various sizes were used to study the effects of etching a microsphere in dilute solutions of HF. The HF solutions had concentrations ranging from 0.1 to 1 percent. This technique resulted in fractional shifts of the resonance frequency $\delta\lambda/\lambda$ on the order of $10^{-7}$. When the sphere diameter was 100 microns, a fractional shift on this order corresponded to a decrease in the radius on the order of 10 pm. This equates to a 3% silica monolayer removal from the microsphere. Smaller frequency shifts for the WGMs were possible with steps sizes on the order of 130 MHz or a diameter reduction of 0.2 pm. With this tuning technique an overall frequency shift of 430 GHz was possible.

Another approach that can be used to shift the resonance frequency of a WGM is to intentionally condense an inert gas, like Xenon, on the surface of the sphere when the sphere is cooled to liquid helium temperatures [122]. With this method the resonance of a photonic crystal slab was shifted over 4 nm at 10 K. However, such a technique is not compatible with fused silica microspheres, and is less than ideal for cavity-QED experiments, because this process would lead to a degradation of the quality factor. Similarly, the etching method is only suitable for room temperature or biological applications because the residual moisture on the surface of microsphere would have a detrimental effect on experiments at cryogenic temperatures.

Another commonly used method to tune the WGMs of a microsphere, while maintaining high-Qs, can be achieved by changing the temperature of the resonator. The resonance frequency shift of WGMs in a microresonator due to thermal changes comes from both a physical size change, a change in the sphere diameter $\delta a$, and from a change in the index of refraction, $\delta n_s/\delta T$ [123, 124, 125, 126]. An expression for the change in wavelength as a function of temperature for fused silica microresonators is given by:

$$\Delta\lambda = \lambda\left(\frac{1}{n_s}\frac{\delta n_s}{\delta T} + \frac{1}{a}\frac{\delta a}{\delta T}\right)\delta T \tag{5.3}$$

In the case of fused silica the change in index of refraction as a function of temperature, $\delta n_s/\delta T$, monotonically increases from 4.2K to 300K and stays positive throughout this range. Unlike the index of refraction the coefficient of linear expansion, $\alpha = (1/a)(\delta a/\delta T)$ changes sign at 200K. At values below 200K, $\alpha$ is negative while above this temperature its value is positive [127, 128]. For temperatures below 20 K the resonance shift is dominated by the thermal expansion term while at higher temperatures (> 77 K) the change in index of refraction as a function of temperature dominates the shift.

The shift in the resonance can be accomplished by either placing the microsphere in a helium bath environment and changing the temperature of that bath, or by optically pumping the microsphere with a secondary laser source. For cavity QED studies, tuning the cavity resonance by changing the bath temperature is effective only over the range of temperatures where the quantum emitter has atomic-like optical transitions. For NV centers, this range is from 0K to 20K and has been used in previous cavity QED studies

with some success [106]. When the microsphere is at temperature of 18.5 K, the values for $\alpha$ and $\delta n/\delta T$ are $-0.6810 \times 10^{-6}$ per Kelvin and $0.8118 \times 10^{-6}$ per Kelvin, respectively.

# CHAPTER VI

# DIAMOND PROPERTIES AND THEORY OF NITROGEN VACANCY CENTERS

The diamond lattice and its large band-gap energy is an ideal host for engineered color centers from the UV to the IR [129]. Doped diamond crystals can have emitters isolated from one another with sharp resonances or they can be densely packed, acting in concert with one another, producing transmissive/absorptive windows through the substrate. The transparency and variety of colors that diamond samples can take on depends strongly on the quantity and type of structural damage, as well as the concentration(s) and type(s) of impurities in the host lattice. The following section details some of the physical and optical properties of diamond. Section 6.2 describes some basic defect centers in diamond. These defects are some of the most well studied color centers hosted in a solid-state medium and are comprised of either a vacancy in the lattice or an interstitial carbon atom.

Section 6.3 discusses the most heavily researched optically active defect in diamond, the nitrogen vacancy (NV) center. It comes in two flavors: neutral and negatively charged. The negatively charged version is more relevant for cavity quantum electrodynamics (cavity-QED) experiments due to its energy level configuration and atomic-like linewidth. The neutral NV center plays an important role in the negatively charged versions dynamics due to charge fluctuations in the local environment.

However, the purpose of section 6.3 is to motivate the NV center as a quantum emitter for cavity-QED applications.

Section 6.4 looks at the advantages and disadvantages of NV centers as a solid-state atom for cavity-QED experiments. The main drawback comes from the large percentage of photons that are emitted into the phonon sided band. As a single photon source, NV centers have low photon count rates and cannot be spectral distinguishable due to their broad (~100nm) emission spectra. Also, it is uncertain how close an NV center can be located from the diamond surface and still exhibit stable and narrow optical linewidths. Examples of alternative color centers being researched in diamond will be discussed in section 6.5.

## 6.1. Diamond Basics

Diamond is the most popularized and well-known carbon allotrope. Figure 6.1 depicts the unit cell of the diamond lattice structure. The "diamond" unit cell of the diamond crystal lattice can be visualized as two face-centered cubic lattices offset by (1/4$a$, 1/4 $a$, 1/4 $a$) of the unit cell. The value of the lattice constant $a$ is 3.567 Å [130]. There are two carbon atoms in the crystallographic unit cell. In this geometry, a single carbon atom is bonded to four neighboring carbon atoms in an $sp^3$ atomic configuration, with tetrahedral symmetry and a bond length of 1.54 Å.

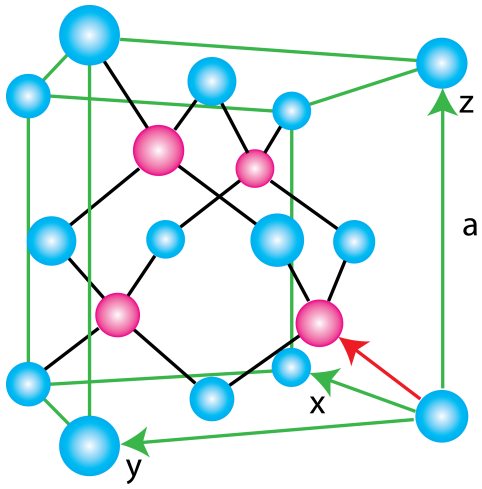


Figure 6.1: A figure depicting the unit cell of diamond.

Diamond stands out as a material due to the fact that it out performs other substances in many categories. As a naturally occurring material, it has the largest thermal conductivity, it is the hardest material, it has the highest Young's modulus, the widest optical band-gap and the largest number density of atoms [131]. It is also chemical inert and biocompatible, making it an ideal marker in biological application [132, 133]. Table 6.1 is a small collection of physical, electrical, thermal and optical properties of diamond. Depending on the sample, naturally occurring diamond crystals can be transparent from the deep UV (~220nm) to the far infrared. The transparency of diamond in general, and at specific wavelengths, is determined by the substrates surface roughness and absorption due to defects in the lattice. Any absorption or emission observed in the visible or near infrared is due to some defect in the lattice that is called a color center.

| Property | Value/Description |
|---|---|
| Lattice Structure | Diamond Cubic, Two FCC lattices offset by $a(1/4, 1/4, 1/4)$ |
| Lattice Spacing, $a$ (Å) | 3.567 |
| Concentration (per $m^3$) | $17.6 \times 10^{22}$ |
| Band-Gap Energy (eV) | 5.46 – 5.6 |
| Index of Refraction, n (near 637 nm) | 2.4111 |
| First Order Raman Line ($cm^{-1}$) | 1332 |
| Thermal Conductivity (W per m*K) | $2 \times 10^3$ |
| Young's Modulus (GPa) | 1220 |
| Dielectric Constant | 5.7 |
| Density (kg per $m^3$) | $3.516 \times 10^3$ |

Table 6.1: A collection of physical and optical properties of diamond.

The average value of the refractive index of diamond over the visible spectrum, $n_d$, is 2.418. An approximate expression for the index of refraction of diamond as a function of wavelength is given by [134, 135]:

$$n^2 = 1 + \frac{0.3306\lambda^2}{\lambda^2 - (175.0)^2} + \frac{4.3356\lambda^2}{\lambda^2 - (106.0)^2}, \tag{6.1}$$

where λ is the wavelength of light in nanometers. The birefringence of a diamond substrate results from stress variations in the substrate, deformations near inclusions, growth sector boundaries and variations in both the type and concentration of impurities in the lattice. Therefore, for optical applications single crystal diamond (SCD) substrates that have minimal crystal damage, deformations and impurities are ideal. The presence of birefringence is easy to observe in a diamond substrate and can be done with a microscope with difference image contrast (DIC) capabilities [136]. Figure 6.2 displays

images taken with an optical microscope with (Fig. 6.2a) and without (Fig. 6.2b) DIC optics in place. The crack near the bottom right can be seen with the standard set-up. However, without the DIC capabilities sub-surface variations in the sample would go unnoticed. With this knowledge it is possible to study variations in the optical properties of color centers due to strain or dislocations.

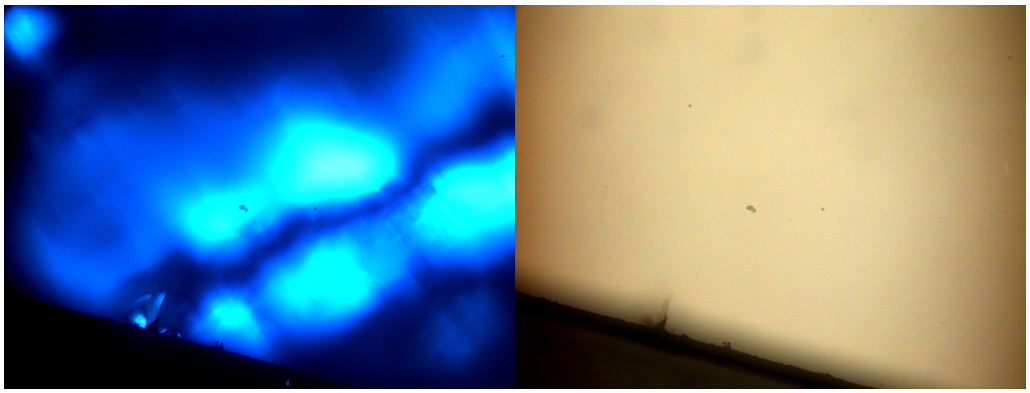

Figure 6.2: Images of a single crystal diamond substrate a) with and b) without difference image contrast optics in place showing the birefringence in the sample.

The classification of diamond is based on its optical absorption due to the presence of nitrogen, boron, and hydrogen related defects and the electron paramagnetic absorption due to substitutional nitrogen atoms [137]. Diamond crystals classified as type I include substrates that exhibit optical and paramagnetic absorptions due to impurity related centers that are predominately nitrogen defects. Approximately 98% of naturally occurring diamond samples have nitrogen concentrations that are detectable through optical absorption [138]. Nitrogen is not uniformly distributed in type I diamond crystals and impurities in these samples form in concentrated areas or in clusters. There are many subcategories of type I diamond samples and for the purposes of this

dissertation only the most relevant classes of diamond related to this work will be mentioned. Type Ia samples are characterized by the fact that no signs of absorption due to single substitutional nitrogen impurities can be observed.

Diamond samples that fall into this grade can have nitrogen atoms that form into aggregates, which are non-paramagnetic, however. Within this sub-category of type Ia diamond, substitutional nitrogen atoms in the lattice are limited to concentrations on the order of $10^{16}$ per cubic centimeter. Type Ib diamonds are characterized as samples where the dominant impurities are paramagnetic nitrogen atoms that are single substitutional defects in the lattice. Naturally occurring diamond samples are rarely type Ib. In diamond substrates of this type, a majority of the nitrogen is uniformly dispersed but there are regions where nitrogen aggregates to form clusters. Most synthetic diamonds are type Ib, most notably substrates that are grown utilizing a high temperature high-pressure method. The distinctive feature of type Ib diamonds is the broad absorption spectrum below 500 nm along with absorption peaks at 275nm, 370nm, 7400 nm, 7800 nm, 8800 nm and 9100 nm. The most common color centers found in type Ib samples are the neutral and negatively charged nitrogen vacancy center.

Type II diamond samples are characterized as not showing any optical or paramagnetic absorption related to nitrogen impurities. Diamond substrates of this type are rare in nature and account for less than 2 percent of all naturally occurring diamond samples. The nitrogen concentration in type II crystals are less than $10^{17}$ per cubic centimeter, or 1 ppm, and are transparent down to 230 nm. Type IIa diamonds are defined as having extremely low concentrations of boron as well as nitrogen. The dominant characterizing feature of type IIa diamonds is the fundamental absorption

continuum below 220nm. Diamond substrates grown utilizing a chemical vapor deposition technique typically fall within this category. Chemical vapor deposition is the growth technique that was used to fabricate the diamond substrates were used in this work. The substrates used in this dissertation fall within the type IIa category.

## 6.2. Defects in Diamond

Just like many other semiconductor materials, the physical and optical properties of bulk diamond substrates can be modified or engineered by introducing defects in the lattice. Techniques are being developed to systematically modify the optical properties of diamond substrates during its growth. When the primary purpose for a diamond substrate is the resulting optical properties of color centers hosted in the crystal lattice, the samples are generally grown employing the chemical vapor deposition technique. However, the tight and strong $sp^3$ hybridized carbon-carbon bonds hinders the incorporation of impurities into the lattice. The ability to controllably grow color centers in diamond substrates at a specific depth or location, as can be done with quantum dots via molecular beam epitaxial techniques, has only recently been reported [139]. However, the most efficient and precise way to modify the optical properties of diamond or create color centers is to irradiate the sample with high-energy particles such as electrons, neutrons, protons, or ions. Irradiation with high-energy particles not only implants the desired impurities into the lattice, but also damage the crystal lattice.

Following the implantation process the substrate is typically annealed at a temperature above 600° C. In doing so the lattice damage caused by the irradiation

process is reduced and helps the implanted impurities relax into a lattice site. A majority of optically active defects in diamond involve impurities coupled to some intrinsic structural defect, such as vacancies or interstitial atoms. Irradiation serves two purposes then: (i) implanting the relevant ions and (ii) inducing the lattice defects necessary to create a color center [140]. Therefore, irradiating samples with impurity ions not only controls the composition of the defects being created, but induces the lattice vacancies that play an important role in the creation of optically active color centers.

The optical properties, quantity and depth below the substrate surface where the defects are produced as a result of ion implantation can be controlled to some degree through a number of experimental "knobs" [141]. These include the type of diamond being irradiated, ion energy and flux, the type and chemical combination of species being implanted, the temperature of the sample during implantation, the angle of the incoming particles relative to the crystal lattice orientation and the time and temperature with which the sample is annealed after being irradiated.

There are more than 500 identified color centers in diamond that are a result of vacancies, dislocations, impurities and complexes in the lattice that create energy levels within the 5.5 eV band-gap. This large band-gap energy of diamond is advantageous because both the excited and ground state of a dipole-allowed transition needs to lie within this range and is the dominant reason why there are such a variety of color centers in diamond. The simplest defects in diamond are called intrinsic. They are formed through either an interstitial carbon atom(s), vacancy(ies), or some combination of the two, in the lattice. Whether, naturally occurring, or produced via electron or neutron irradiation, the most stable configuration of this class of defects is the split <100>

interstitial called the R2 color center [142, 143]. It exhibits an optical absorption line at 735 nm and can be annealed out of the lattice by raising the sample temperature above 475C.

The vacancy center in diamond is can be in two charge states; the negatively charged and neutral vacancy center. The neutral charge state is labeled as the GR1 color center and exhibits a ZPL line at 740nm [137]. The abbreviation GR stands for general radiation. It is one of the most studied color centers that originates from a point defect in a solid and is the most prominent feature of any type of irradiated diamond. However, its intensity is dependent on the impurity level of the sample. When a diamond sample is at a temperature above 600° C, the vacancies become mobile and migrate in the lattice reducing the lattice stress induced by the incorporation of impurities. As a result new complexes may form and the number of vacancies reduces. If the number of GR1 defects is monitored while a substrate is being annealed, a decrease in the intensity, and eventual disappearance, of the zero phonon line (ZPL) will be observed.

Vacancies play a fundamental role in forming color centers in diamond because other elements that are larger than carbon cause a local expansion in the lattice as they are incorporated into the dense diamond structure. A vacancy adjacent to the impurity reduces the distortion in the lattice caused by its presence. When annealing a diamond sample at a temperatures above 600° C, and less than 1150° C, only vacancies are mobile in the lattice. In this range of temperatures, if an impurity happens to neighbor an empty lattice site it can relax into the vacancy. If there is no empty lattice site, the impurity will remain as an interstitial. As the vacancies become mobile they can combine with the impurities to lower the amount of lattice distortion. Vacancies play another important

role in forming color centers. The electrons associated with the dangling bonds that surround the vacancy can become part of the electronic structure of the resulting complex.

Nitrogen is the most common impurity related defect in diamond [144]. Nitrogen is typically present during the growth process, especially in naturally occurring diamonds, and its atomic size is similar to carbon. In the previous section, it was discussed that different classes or types of diamond are distinguished by the amount of nitrogen content contained in the substrate and its distribution. It is well established that this impurity has been attributed to a large number of the known color centers in diamond [145]. Nitrogen plays a unique role in forming optical defects throughout the entire spectral range that is studied in diamond; the exact cause has yet to be determined. There are numerous forms of nitrogen complexes that are optically active: single substitutional and interstitial nitrogen atoms, centers that are comprised of multiple nitrogen atoms, nitrogen atoms coupled to one or more vacancies in the lattice or to other impurities. Furthermore, nitrogen related defects are the most studied impurity related defects in diamond, especially the negatively charged nitrogen vacancy (NV) center.

## 6.3. Nitrogen Vacancy Centers

When a substitutional nitrogen atom is placed at a lattice site, it creates a deformation along the (111) lattice direction with the adjacent carbon atom [146]. If the nitrogen atom is adjacent to a vacancy in the lattice, however, a NV center is formed and the deformation in the crystal is reduced [147]. This configuration is a lower energy state

of the lattice, making the pairing of a substitutional nitrogen atom with a neighboring vacancy in the lattice a more favorable arrangement. Figure 6.3 is a diagram depicting the structure of a NV center where the bonds towards the vacancy represent dangling bonds of the neighboring carbon atoms and the substitutional nitrogen atom. The NV center can be found in two charged states; the neutral charged state ($NV^0$) or the negatively state ($NV^-$) [148]. The $NV^0$ state of the defect center has five electrons; 2 unpaired electrons from the nitrogen atom and three electrons from the dangling bonds of the carbon atoms surrounding the vacancy site. This form of the color center exhibits a ZPL emission at 575 nm with a phonon sideband that extends up in wavelength near 620 nm.

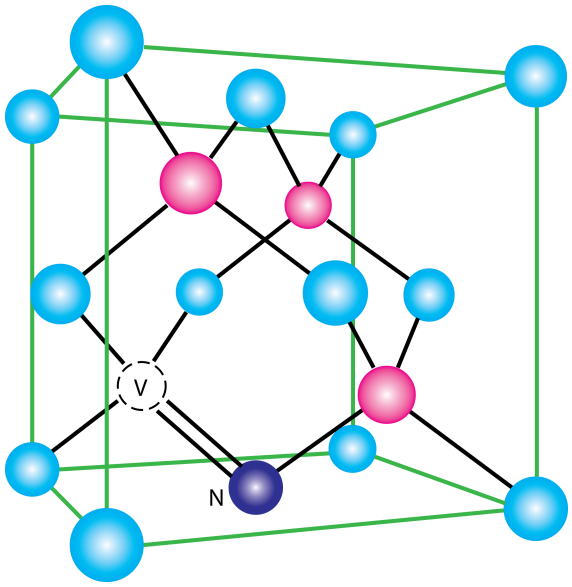


Figure 6.3: A figure depicting a nitrogen vacancy center in the unit cell of diamond.

The negatively charged version of the NV center has these same five electrons, two from the nitrogen atom and three from the carbon atoms, plus an extra electron

captured from another defect in the lattice. This extra electron originates from some other impurity, most likely another nitrogen atom, in the lattice. Unless specifically mentioned, the use of the term NV center will refer to the negatively charged version of the defect throughout this dissertation. The electronic energy level structure of the NV center is depicted in Fig. 6.4 and is based the most current research, both theoretically and experimentally.

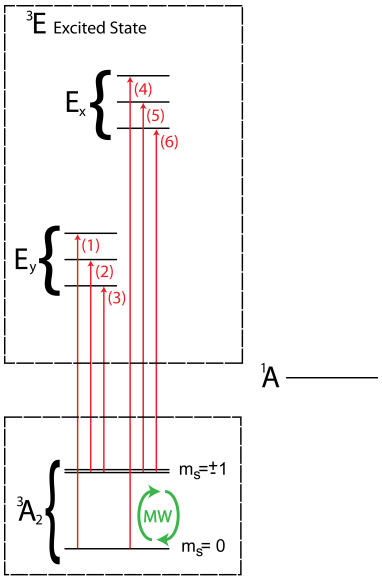


Figure 6.4: The energy level diagram for the negatively charged nitrogen vacancy center in diamond.

Through optically detected magnetic resonance (ODMR), electron spin resonance (ESR), spectral hole-burning, and Raman heterodyne experiments the ground state electronic structure of the NV center has been determined to be a $^3A_2$ spin triplet system [149, 150, 151, 152, 153, 154]. Spin-spin interactions between the electron captured from the lattice and one of the unpaired electrons of the neutral center results in a splitting of the electronic ground state [155]. The splitting that results from this

interaction results in a separation between the $m_s = 0$ spin singlet level, $S_z$, and the spin doublet $m_s = \pm 1$ states, $S_x$ and $S_y$, by 2.87 GHz. In this nomenclature, the z-axis points along the NV center symmetry axis.

The excited state structure has $^3E$ characteristics and is a spin triplet orbital doublet [156]. The relative spacing between the various energy levels is specific to each individual NV center due to environmental variations from sample to sample and from region to region in a sample. Between the excited and ground states lies a meta-stable singlet dark state [151]. Even though the first recorded observation of the NV center was made in the early 1960s by L. du Perez, and has been feverishly studied over the past decade, a complete understanding of the dynamics and mechanism that govern the excitation and emission process has not been fully developed [157, 158, 159]. Studies are still being conducted to tease out these final details.

The optical transitions between the $^3A_2$ ground states and the $^3E$ excited states are associated with a zero-phonon line transition near 637 nm and a broad emission spectrum into the phonon sideband from 640 nm to 800nm. There are six, nearly spin conserving, optical transitions between the excited and ground states. This configuration is depicted in Fig 6.4 [160]. The excited state structure depends on the local environment of the NV center and is heavily influenced by strain that is transverse to the z-axis of the color center; in particular, the difference in energy between $E_x$ and $E_y$ orbitals and the relative positions of the electron spin sublevels [160, 161].

The excited state energy level spacing is therefore different for every NV center and needs to be determined experimentally. Furthermore, the spectral stability of a NV

center is strongly influenced by its local environment making the choice of a specific sample application specific [162]. Also, there are four distinct dipole orientations of the NV center resulting from the fact that there are four possible lattice positions for the vacancy neighboring the nitrogen atom [163, 164]. The relative spacing between these levels is a result of spin-spin interactions, spin-orbit interactions, local electric and magnetic fields in addition to lateral and transverse strain. Figure 6.5 illustrates what role these various mechanisms play in shaping the final excited state energy level structure for an NV center, which follows a theory developed by Ph Tamarat, et al. [165].

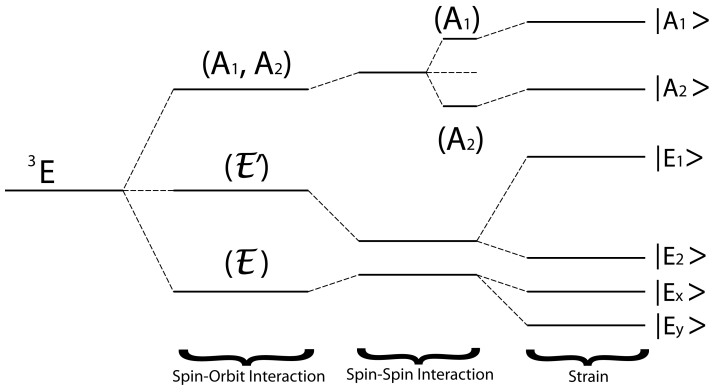


Figure 6.5: A schematic depicting how spin-spin, spin orbit and strain interactions split the excited state spin-sublevels.

The $^3$E state branches off into three levels due to spin-orbit interactions that are doubly degenerate and are denoted as $E$, $E'$, and ($A_1$,$A_2$) according to the irreducible representations of the $C_{3v}$ representation. Through a spin-spin interaction the $E$, and $E'$ levels shift in energy, while the $A_1$ and $A_2$ levels both shift in energy and split. Strain along the NV center symmetry axis causes a linear shift in the energy levels while strains

perpendicular to this axis cause a shift as well as a splitting of the $E$ and $E'$ levels. As was mentioned before, it has been established that a non-radiative metastable state lies between the excited and ground states. It is unknown how these various internal interactions, strain or local electric and magnetic fields impact this meta-stable level.

The metastable state is thought to play an important role in the NV center's dynamics when optically excited [166]. The decay rate from the excited state $S_z$ level to this metastable state is much less than that of the $S_x$ and $S_y$ levels. In other words, there is a higher probability of decay from the $S_x$ and $S_y$ excited states to the metastable state. Figure 6.6 depicts this difference in decay rates to and from the metastable state, which results in a spin dependent fluorescence intensity. The asymmetry in the decay rates into the metastable state causes the fluorescence from the $m_s = 0$ ground state to be 20% brighter when compared to the NV center being excited from the $m_s = \pm 1$ states. This phenomenon is used to detect the spin state of the NV center at room temperature [167].

There is a higher probability that once in this metastable state, the NV center will decay into the $m_s = 0$ ground state. The fact that the decay rate of the NV center from the metastable state to the $m_s = 0$ level is greater than that of the $m_s = \pm 1$ levels, leads to an all-optical method to polarize the spin state. Polarization of the NV centers electron spin state can be accomplished after only a few optical cycles. These features lead to a convenient all-optical spin preparation and read out technique based on the average spin state [168]. This can be done at room temperature making the NV center a leading for spin qubit. Recently, a technique has been developed to determine the electron spin-state

with a single-shot readout method [169]. This is done via resonant excitation at liquid helium temperatures.

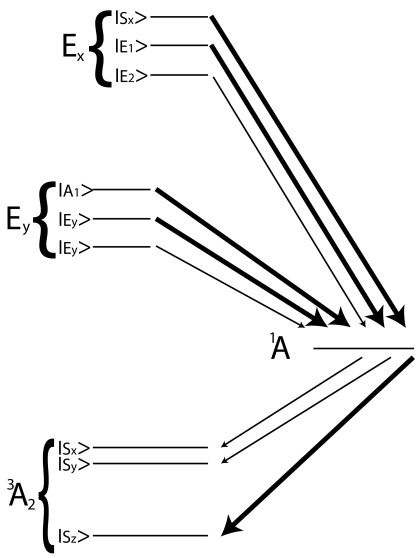


Figure 6.6: An energy-level diagram depicting the likely hood of decaying from excited state to the metastable state and from the metastable state to the ground state sublevels. The bolder lies depicting the transition are more likely than the thinner lines.

In addition to optical manipulation of the NV center, applying RF magnetic fields at 2.87GHz can manipulation of the electron spin state. Continuous wave experiments allow for the detection of electron spin resonances of the $m_s = \pm 1$. As the RF field is swept across the ground state splitting frequency of 2.87 GHz, an OMDR dip characteristic of the NV centers can be observed. This is depicted in Fig. 6.7 and was obtained by collecting the fluorescence from a single NV center at room temperature.

In the presence of an externally applied magnetic field these two states are split with a shift that is approximately $\pm m_s \bullet 2.8$ MHz/Gauss [170]. Figure 6.8 shows a splitting

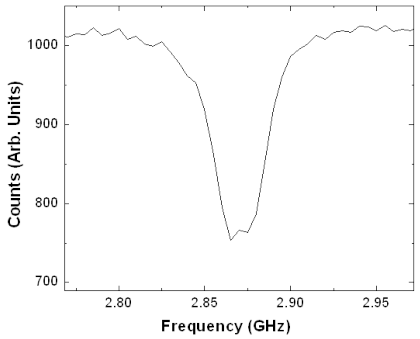


Figure 6.7: An optically detected magnetic resonance dip observed from a nitrogen vacancy center in a ppb sample at 300K.

in the OMDR dip when a magnetic field is applied to the NV center. When pulsed RF magnetic fields are applied a number of experiments can be done resulting in the observation of Rabi oscillations and Ramsey Fridges [171]. With pulsed RF field measurements it has been determined that the spin coherence time of a NV center in a 99.8% carbon-12 lattice can be as long as 1.8 ms at 300K without any pre- or post-processing techniques [172, 173]. It should be noted, applying CW or appropriately timed RF pulses to populate all of the spin states in the ground levels is necessary to see all six optical transition show in Fig. 6.4; a static field would be used to lift the degeneracy of the $m_s = \pm 1$ states and to shift the resonances.

## 6.4. Advantages and Disadvantages of NV Centers

Every quantum emitter has its advantages and disadvantages when considering a particular application. The nitrogen vacancy center is currently the leading candidate for spin-based quantum information processing (QIP) applications due to a number of

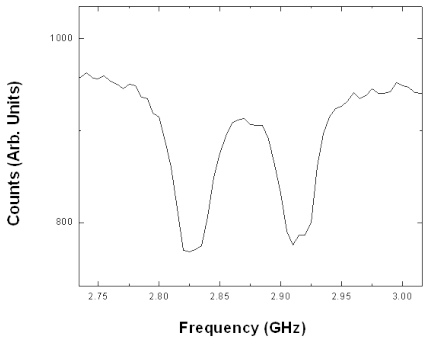


Figure 6.8: A splitting in the optically detected magnetic resonance dip as a result of an external magnetic field.

favorable attributes which include: the electron spin state can be optically i) polarized and ii) readout in addition to ii) the mature protocol that is available to manipulate the spin-state which can have iv) a long coherence time. Diamond substrates that contain minima forms of impurities and defects, as well as being nearly (>99.8%) composed of carbon-12, support centers where the electron-spin coherence time can exceed milliseconds at room temperature. By mapping the electron spin state of a NV center onto the nuclear-spin state of a neighboring carbon-13 atom, in conjunction with dissipative decoupling techniques, a solid-state spin qubit can be accessed with a coherence time exceeding a second at room temperature [174, 175]. Alternatively, the electron spin state can also be mapped onto the nitrogen atom comprising the NV center, extending the coherence time of the system.

Another advantage in using NV centers for quantum information processing applications is the fact that there already exists a mature protocol to optically prepare and readout the NV center electron-spin state in addition to the ability to manipulate them with RF pulses and externally applied magnetic and electric fields [176, 177, 178].

Optical properties that make the NV center an ideal candidate for QIP applications include the fact that the ZPL emission from an NV center has a nearly transform limited linewidth at cryogenic temperatures [179]. The energy level state structure of the NV center is nearly understood, including the presence of a metastable state lying between the ground and excited states that is used for optical readout techniques. At liquid helium temperatures, there is a growing suite of techniques which can be called upon in order to optical manipulate the electron-spin state of the NV center [180, 181].

A decade of extensive research has lead to a mature understanding of the optical and electron spin dynamics for the NV center. These optical and electron-spin features make NV centers an appealing candidate for numerous applications from QIP to quantum metrology [182, 183, 184, 185]. However, a major roadblock in the broad adoption of the NV center as a quantum source of light is the fact that only 4% of the total photons emitted go into the ZPL, resulting in a small oscillator strength [186]. This makes the utilization of NV center unfavorable in implementations that require spectrally indistinguishable photons and efficient spin–photon entanglement.

The dominance of a phonon-assisted decay into the sideband results in only a few thousand counts per second emitted into the direct dipole transition. Counting rates at these levels could be inadequate for the implementation of advanced QIP protocols based on the coupling between spin states and optical transitions within reasonable data acquisition times. To move beyond this and other limitations of the NV center, while taking advantage of diamond as a host medium for quantum emitters, the optical and electron-spin properties of alternative diamond based color centers are being studied. This is being done to determine the feasibility of implementing these new color centers in

advanced QIP and quantum metrology applications. The aim is to find centers with superior optical properties, with similar electron-spin properties including manipulation and readout, when compared to the NV center.

## 6.5. Other Interesting Color Centers in Diamond

Recently, a new host of diamond based quantum emitters have emerged which could have superior optical properties when compared to the NV center. These color centers include the silicon vacancy center (Si-V), the nickel-based center (Ne-8) and the chromium-based color center (currently proposed as the UM2 center) [187, 188, 189, 190]. As of now, only a few groups are investigating the optical properties of these defect centers. The goal stated by these groups is to develop a detailed picture of the chemical composition, as well as physical, optical and electron spin properties for these diamond-based emitters. There is also a need to develop an understanding of the energy level structure and their interaction with externally applied fields. This work is done in collaboration with other groups who are developing and refining processes to systematically fabricate these color centers in single crystal diamond or diamond nanocrystals. As mentioned before, there are two was of doing so: (1) through direction ion implantation and (2) during the growth of the crystals.

The Si-V center consists of a silicon atom and a vacancy in a 'split-vacancy configuration'; the silicon impurity sits at a lattice site but relaxes towards a vacancy. This color center has been successfully created via ion implantation and during sample growth. Fluorescence from the Si-V center was first reported in 1981 by Vavilov, et al.

[191]. Off resonant excitation is typically done with laser radiation at a wavelength centered near 680 nm. The Si-V center is a single photon source at room temperature with a ZPL transition at 738 nm. This color center exhibits a weak phonon sideband under ambient conditions. Lifetime measurements have been conducted on the center determining that the excited state lifetime is on the order of 1 to 5 nanoseconds [192, 193]. The linewidth of the ZPL for this center has been measured to be as low as 0.7 nm at room temperature. Color centers of this type have been found in diamond nanocrystals with a measured photon count rate of up to $3.5x10^6$ counts per second.

Another diamond color center that can possibly replace the NV center is based on a nickel impurity and has been labeled as the NE8 center. It consists of a substitutional nickel atom surrounded by four nitrogen atoms. When it is excited off resonantly at a room temperature near a wavelength of 700nm its emission shows signatures of being a single photon source. The ZPL is near 800 nm and has a weak photon emission into a phonon side; in some centers it has been observed that the phonon sideband extends up to 850 nm. The linewidth of the ZPL for this color center is approximately 1.8 nm at room temperature and the Debye-Waller factor is on the order of 0.7. This is an order of magnitude greater than that of the NV center. The excited state decay rate and photon counting rate is similar to that of an NV center. This center can be created most efficiently via chemical vapor deposition growth of diamond nanocrystals.

The chromium color center is also a single photon source at room temperature. Its structure has yet to be fully determined. However, it is know to have one interstitial chromium atom. The chromium-based color center is excited off resonantly at a wavelength centered near 700nm. The ZPL is near 770 nm and exhibits a weak sideband

near 780 nm. At room temperature, the ZPL has a linewidth of approximately 4 nm (FWHM) and at liquid helium temperatures the linewidth has a minimum measured value of 4 GHz. This minimum linewidth at low temperatures is not intrinsic to the color center and is thought to be limited to spectral diffusion or dephasing mechanisms. Optically, this is the sharpest color center in diamond after the NV center. It displays an excited state decay time of approximately 1 ns and has a Debye-Waller factor greater than 0.9. The photon emission rate for the center is $5 \times 10^5$ counts per second at a saturation power of about 3 mW. These numbers are specific to the experiment referenced above, when a 0.65 NA objective was used at an excitation wavelength of 710nm. Also, these figures for the counting rate were reported from chromium centers created approximately 10nm below the surface of high purity SCD via co-implantation of chromium and oxygen ions.

The main advantage of these color centers, when compared to the NV center, is the higher fraction of photons that are emitted directly into the ZPL. The fact that these single photon sources emit most of their photons into the ZPL can enable them to be incorporated into advanced QIP applications. Another advantage of these color centers is the fact that the emission is in a spectral region where the background from diamond is weak. Emission in this spectral region is also beneficial for the transmission of information emitted from these color centers. Attenuation of optical signals at a wavelength near 690 nm (the center of the NV center spectrum) double that of 770 nm. Furthermore, the demands on color translation for the emission from these color centers would be less than that of the NV center. Color translation is used when the information

from one quantum emitter is to be mapped onto another quantum emitter in different quantum architectures that are based on different quantum sources of light [194, 195].

In conclusion, the NV center sets a high bar for these emerging diamond based color centers. None of these emitters currently show narrow atomic-like transitions between the ground and excited states. However, it is expected that the linewidth for these emitters can be improved as fabrication techniques improve. Also, the energy level structure and chemical composition of these emitters has yet to be completely understood. Little work has been published on how external magnetic and electric fields would modify the emission properties of these color centers. In the work by T Müller, et al., it was shown that the emission wavelength of chromium centers could be shifted with an applied electric field. In this same work, the emission characteristics were unaffected by an applied magnetic field along the dipole direction. At the time of writing this dissertation, and to the best of my knowledge, there was no published work on the electron-spin characteristics of these color centers let alone any means to detect or manipulate the electron-spin states. These factors will determine whether or not another color center will become the next generation of diamond based emitters, or if the NV center will continue to outperform them.

# CHAPTER VII

# DIAMOND EXPERIMENT

This chapter discusses the two experimental techniques employed to optically characterize native and irradiation induced nitrogen vacancy (NV) centers in single crystal diamond (SCD) substrates. With these techniques the suitability of various SCD samples was studied for cavity quantum electrodynamic (cavity-QED) studies. The first optical characterization method used a non-resonant laser to excited NV centers. This allowed for the detection and characterization of NV centers by collecting the photoluminescence (PL) emission into the zero phonon line (ZPL) and into the phonon sideband. This approach did have an effect on the local environment, which in turn has an effect on the electron spin and optical properties of the emitter. The second technique, called photoluminescence excitation (PLE), used a laser source that was resonant with one of the six optical transitions mentioned in the previous chapter. This technique required the diamond sample to be cooled down to temperatures at or below 10K.

Filtering out the laser source and the ZPL, and detecting only the photons emitted into the sideband allowed for the investigation of the homogenous linewidth and spectral stability of the specific transition. Sections 7.1 and 7.2 will describe the concept of PL and PLE and the following section will describe the experiment. Sections 7.5 and 7.6 will describe the optical properties of NV centers in diamond substrates at ~300 K and 10 K, respectively. The data in these sections are for color centers that were created during

the growth process. Section 7.7 of this chapter will discuss the considerations taken when implanting nitrogen ions into SCD sample. In sections 7.8, PL data for NV centers in regions of samples that were irradiated with nitrogen ions will be discussed. Photoluminescence excitation data will be presented in section 7.9.

## 7.1. Photoluminescence of Nitrogen Vacancy Centers

Non-resonant and resonant excitation techniques can be used to study the optical and electron spin properties of NV centers. In general, PL is the absorption and subsequent emission of electromagnetic radiation from an optically active material. Non-resonant measurements excite NV centers into an above-band state that then relaxes down (non-radiatively) to one of the six $^3$E electronic excited states. Following this, the NV center relaxes back to the ground state by emitting a photon. A Jablonski diagram is depicted in Fig. 7.1 for the case of an NV center being excited off-resonantly.

Photoluminescence excitation is a non-contact and non-destructive process that has been extensively used to characterize various semiconductors materials and the emitters they host [196, 197, 198, 199, 200]. In addition to exciting the color center, photons of sufficient energy will effect the local environment through an interaction with the lattice and other defect centers in the crystal. Following the excitation process, the electronic state relaxes back to a lower energy state by releasing phonons into the lattice in addition to releasing a photon. With phonon coupling taken into account, the energy of the photons that are absorbed or emitted corresponds to the energy difference of the electronic states of the material, plus the corresponding number of lattice vibration quanta

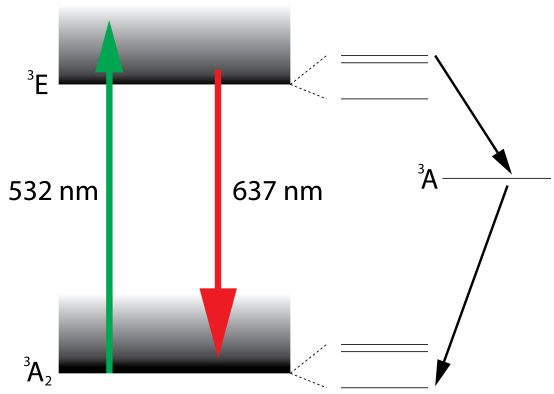


Figure 7.1: Non-resonant excitation takes the nitrogen vacancy center to an above-band excited state. The system relaxes by through radiative and non-radiative processes.

during the energy transfer [201].

Details of the optical and electron spin properties of the emitter and how the lattice impacts these properties can be deduced with the use of various pulsed or continuous wave experiments [202]. When exciting an NV center off resonance the laser source typically has a wavelength near 500 nm. For the purposes of this dissertation, PL experiments were conducted for a number of measurements with a continuous wave Nd:YAG laser at 532 nm. Photoluminescence experiments helped determine the optical properties of NV centers induced via the implantation of nitrogen ions and to see how the spectrum from these centers compared to those that were created during the sample growth, at both room and low temperature. Another application of this technique was to locate diamond nanopillars fabricated from SCD that contained NV centers. Once a diamond nanopillar was determined to have NV centers, PL measurements were used to determine the effects that the nanopillar fabrication had on the optical properties of emitter in the pillars. Photoluminescence experiments were also used to determine the

nanopillars that would be used in the composite system discussed in chapter nine. These results will be discussed in chapter eight of this dissertation.

## 7.2. Experimental Principles of Photoluminescence Excitation

Another optical measurement technique used to characterize NV centers in bulk diamond or diamond nanopillars which were naturally occurring or induced via ion implantation, was accomplished with the use of a resonant excitation technique. Resonant excitation was used in the study of specific optical transitions of an NV center. The process that was used to resonantly excite (and therefore detect and manipulate) the various optical transitions of a NV center is called photoluminescence excitation (PLE). These measurements must be conducted at liquid helium temperatures (<10K). It was easiest to work at the edges of the ZPL when spectrally isolating the transition frequencies of a single NV center. This region might be called 'the wings' of the inhomogeneous distribution. Figure 7.2 depicts the general idea behind this technique, which can be thought of as an absorption measurement.

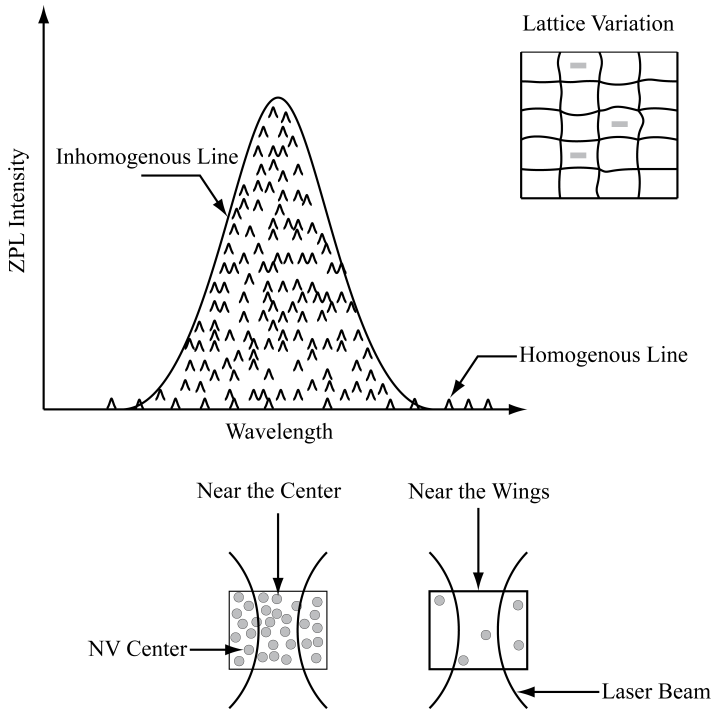


Figure 7.2: The inhomogenous linewidth reflects the variation in the center frequencies of the homogenous linewidths for the ensemble of emitters in the excitation space. The center frequency of the laser source, the region of the sample under study and the excitation volume all play a roll in defining the excitation space.

This approach is widely used to optically characterize individual color centers and molecules to address the atomic like transitions for coherently control of quantum emitters [203, 204, 205]. Due to variations in the diamond lattice and local impurity concentrations of each color center, the resonance frequencies associated with the six electronic transitions will vary from center to center. This distribution of ZPLs for NV centers results in an inhomogenously broadened line-shape for the ensemble, which is the superposition of the homogeneous linewidths for each individual emitter. To reduce the excited state structure of two NV centers overlapping in the same frequency space, low-

density samples were used to spatially isolate emitters. With the diamond substrate cooled to temperatures at or below 10K, single NV centers can be spectrally isolated by scanning the output of a tunable laser, with a spectral bandwidth narrower than the homogenously broadened transition, near the wings of the ZPL distribution.

When the laser frequency becomes resonant with a single transition, it drives that resonance causing emission into the ZPL and the phonon sideband. The homogenous linewidth of a particular transition was measured by filtering out the resonant laser (and the ZPL), and detecting only the photons emitted into the phonon sideband. Utilizing the PLE measurement technique not only allows for the excitation and manipulation of each transition amongst the six optical transitions, it also allows the researcher to monitor the spectral stability of that NV center over time. The instantaneous linewidth and relative frequency of a transition was determined by acquiring data while a laser was scanned across a transition while detecting the emission.

Two-dimensional contour plots were made from these individual plots by stacking them one after another. These plots were used to visualize the spectral stability of the NV center found in ppm or ppb samples. This was used to determine if either of these two types of diamond substrates were suitable for cavity-QED experiments. This method was also used to determine the typical linewidth for a NV center found in various types of samples, both naturally occurring and created via ion implantation.

## 7.3. Experimental Set-Up

The optical measurements described in the previous two sections were carried out with the use of a home built confocal microscope. A diagram of the confocal set-up is shown in Fig. 7.3. In this set-up, three laser sources could be used to investigate the optical properties of NV centers. For PL experiments, a frequency doubled Nd:YAG laser (Coherent Verdi-5) operating at 532 nm was used. Its emission was passed through a 532 nm bandpass filter (Thorlabs FL05532-10) to reject unwanted laser radiation at other wavelengths. For PLE experiments two types of lasers were employed. Coarse-grained, long-tuning-range scans were taken with a tunable (~8 nm) diode laser (New Focus Velocity 6304) with a center wavelength near 637 nm. To conduct higher spectral resolution scans, an external cavity frequency-stabilized tunable dye ring laser (Coherent 899-21) was operated at 637 nm (Exciton Kiton Red 620). After the diode and ring laser sources had their outputs steered onto the same optical path, the emission was cleaned up with a bandpass filter (Thorlabs 635-10). The path of the two resonant lasers was then aligned with that of 532 nm laser. This allowed any of the laser sources to be focused onto the same NV center under investigation simultaneously.

These three lasers were reflected off of a 90:10 beam splitter and directed to an 0.60 numerical aperture 40X magnification microscope objective (Olympus LUCPLFLN40) that was used to focus the laser sources on, and collect the emission from, NV centers in the diamond substrate. The microscope objective had a working distance of 3.4 mm and had a correction collar to compensate for cover slips up to 2 mm

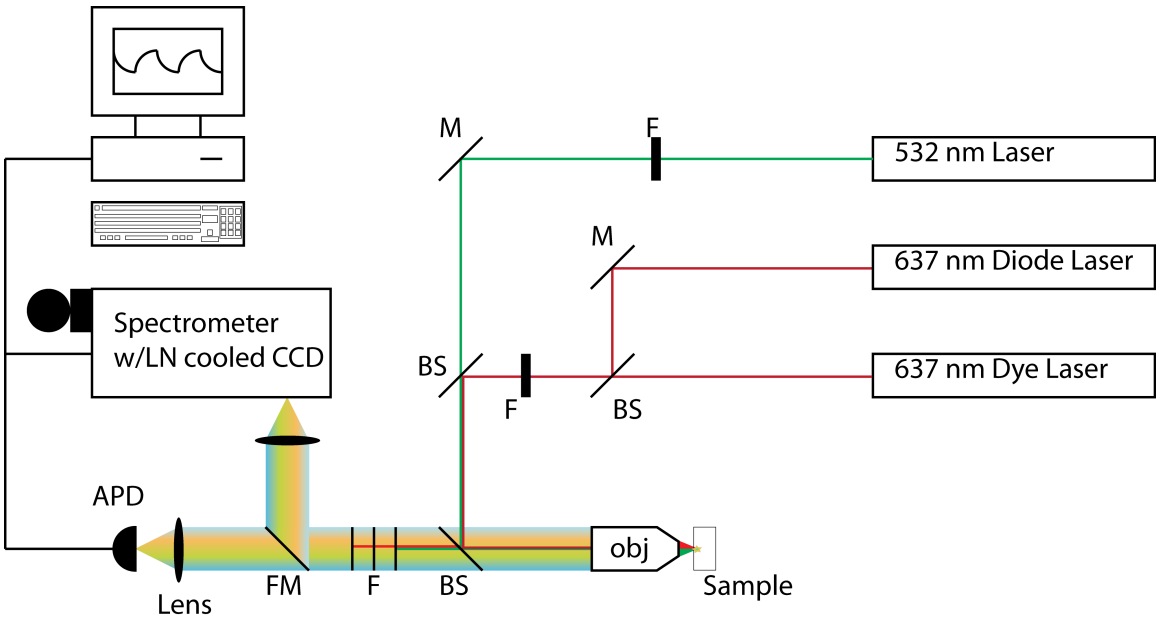


Figure 7.3: A schematic showing the basics of the confocal microscope. Three laser sources were cleaned up with filters (F) and guided onto the same principle axis with mirrors (M) and beam-splitters (BS) guiding all three sources to the same microscope objective (obj). The fluorescence from the sample went through a set of filters to remove the lasers and could then be coupled to either an avalanche photodiode (APD) or steered to a spectrometer with a flip mirror (FM).

thick. This cover slip correction feature was necessary when performing optical measurements of NV centers at liquid helium temperatures. In the case of low temperature studies, the samples were mounted on the end of a cold finger cryostat (Advanced Research System LT-103) with a modified vacuum shroud. This cold finger configuration is shown if Fig 7.4. The modified vacuum shroud allowed the sample to be placed as close as possible to the cryostat window. The sapphire window was 2 mm thick. The correction collar compensated for the presence of the cryostat window between the sample and the objective.

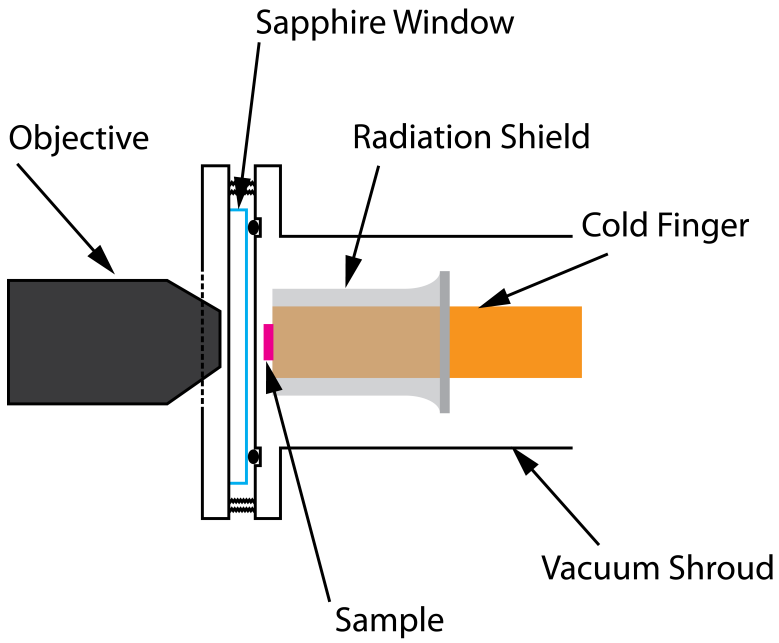


Figure 7.4: An image of the confocal set-up where the microscope objective meets the sample when the sample is mounted in an optical cryostat.

After the NV center was excited, its emission was collected and directed through a series of filters before being sent to a detection set-up. The emission from the NV center could be detected and characterized with either a spectrometer (Princeton Instruments, Acton Research SpectraPro 2500i) fitted with a liquid nitrogen cooled charge-coupled device (CCD, Princeton Instruments Spec-10) or an avalanche photodiode (APD, Perkin-Elmer SPCM-AQR-16-FC). Depending on the type of optical measurement being conducted a different combinations of filters were used. For PL spectroscopy measurements, a single 532 nm laser line filter (Kaiser HSPF-532.0-1.0) was used before the signal was detected. For PLE experiments, a laser line filter at 637 nm (CVI 60761649-637.0nm) and a long pass filter (CVI Razor Edge ® Long Pass 647) with a cutoff wavelength of 647 nm were used. The laser line filter cuts out a majority of the laser back reflection from the sample surface, while the long pass filter ensures that

only the phonon sideband was being detected. If pulses of green were used during the PLE measurements, then all three filters were in the detection path.

The signals from the spectrometer and the APD were then sent to a computer to acquire and store the data. Commercially available software from Acton Research is used to operate the spectrometer. When taking PL spectrum from bulk diamond substrate, the laser power from the Verdi focused onto the sample surface was in the range 0.1 mW to 500 mW. This is the laser power at the clear aperture of the microscope objective. The integration time of the spectrometer was on the order of 1 second to 600 seconds. This wide range of laser powers and integration times was necessary because of the different NV center concentrations in the SCD substrates. When conducting PL measurements of the highest purity samples at room temperature, higher powers and/or longer integration times were necessary to acquire a signal from the samples. When the samples were cooled to liquid helium temperatures, lower laser powers were used with shorter integration time.

When the APDs were being operated in Geiger mode to detect photons, the transistor-to-transistor logic output of the APD is counted with a counting card (PCI 6602 National Instruments) installed in the computer. This mode of detection can be used with either the off resonant or the resonant excitation technique. When exciting the NV centers off resonantly, there were no issues with the NV center going dark. However, with resonant excitation, there was a probability of the NV centers going into the metastable dark state or photoionizing. In the case of resonant excitation it was necessary to minimize the amount of time that the NV center is continuously excited.

During resonant studies of NV centers, lasers were scanned over the transition frequency of the NV center to avoid the issue of exciting the NV center for too long. Scanning the laser across the NV center resonance does not completely eliminate the issue of an NV center going dark; considerations regarding the amount of laser power that was focused on the defect, as well as how fast the scan speeds were necessary, were also necessary. The wavelength of the diode laser could be coarsely scanned from 632 nm to 639 nm with minimum steps size of 0.01 nm. However, to study the narrow linewidths of NV centers with the diode laser, the fine tuning capabilities of the laser were necessary. With the use of a function generator, the frequency output was scanned over 60 GHz by applying a ±3 V to a piezo element in the cavity. The linewidth of the diode laser was less than 300 kHz. The dye laser can also be scanned internally or via the function generator. It had a maximum scan range of 30 GHz with a linewidth that was less than 1 MHz.

When conducting PLE experiments, the laser wavelength was centered near the tail edge of the ZPL; specifically, on the blue-side of the zero phonon line. Depending on the sample under investigation, and its temperature, the wavelength that corresponds to this spectral position would vary and was found by using the coarse tuning of the diode laser and the wavelength meter. As the output frequency of the diode laser was scanned across the ensemble of NV centers in the excitation volume, the spectral distribution of the NV centers was measured. To cut out as much background radiation as possible the excitation/collection plane was imaged onto a multimode fiber. Coupling to a pinhole (core of a fiber in this case) reduces the number of photons that do not originate from the region of interest.

7.4. Optical Properties at 300 K

At room temperature, NV centers in bulk substrates exhibited a weak and broad emission into the ZPL. Most of the photons were emitted into the phonon sideband over an emission ranging from 640 to 800 nm. Figure 7.5a shows the PL emitted from an ensemble of NV centers in a CVD grown diamond substrate containing a nitrogen concentration in the >1 ppm range. This sample was excited with a laser power of 0.29 mW and the integration time of the spectrometer was set to 1 second. Figure 7.5b is a plot of the PL collected from a sample with a nitrogen concentration in the >5 ppb range. It was excited with 100 mW of power and the integration time was 60 seconds.

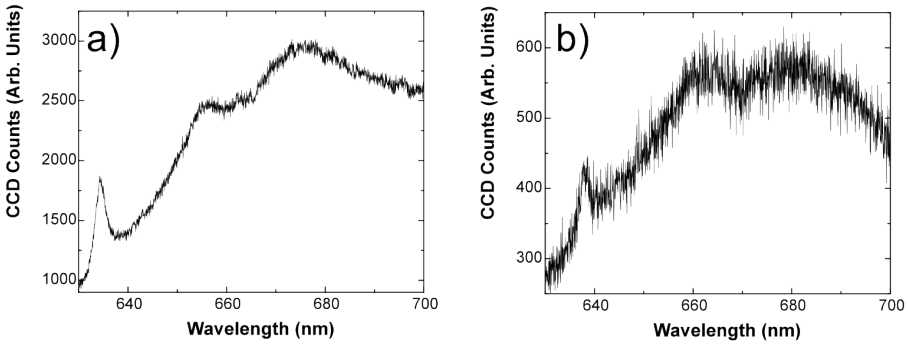


Figure 7.5: Room temperature photoluminescence spectrum from nitrogen vacancy centers in diamond samples containing nitrogen in a) ppm and b) ppb concentrations.

For both of these plots, the signal originates from multiple NV centers in the volume of the sample that the microscope objective collects from. Also, the microscope objective was focused just below the surface of the sample. As would be expected, the signal from the ppb samples was much weaker than the higher-density sample. This

confirmed that the number of NV centers in the excitation/collection volume was smaller in the ppb samples. There was one sample where no NV centers could be measured throughout the entire sample. There were five ppb samples studied in this work, and only one of the samples indicated that there were no NV centers present. All other ppb samples had regions where PL from NV centers could be found.

As can be seen from these figures, NV centers at room temperature display a strong phonon sideband in their fluorescence spectra. These two plots are representative of the PL spectra that would be obtained from the two classes of samples studied in this research. For ppm samples, the center wavelength for the ZPL and its intensity could fluctuate within a given sample. However, in these single crystal diamond substrates the variation was negligible. In the case of ppb samples, the variation in the ZPL center wavelength was also negligible. On the other hand, the intensity of the ZPL did change drastically within a ppb sample. When an APD was used to measure the PL signal, ppm samples showed a slight variation (a few percent) in the count rate, from region to region, while the laser power was maintained at a constant value. Typically, in ppb samples at room temperature, there were large regions where considerable APD counts (~10,000 counts per second) could be measure with a power on the order of a few milliwatts.

## 7.5. Optical Properties at 10 K

At temperatures near or below 10 K the ZPL becomes sharper and brighter than the phonon sideband, which is suppressed. This can be seen from Fig. 7.6, where Fig. 7.6a and Fig. 7.6b are PL spectra collected from samples that had a nitrogen

concentration in the ppm and ppb range, respectively. These were the same diamond substrates that were used in Fig. 7.5. However, these data were taken from different regions of the samples. At these temperatures the linewidths of the ZPL were approximately 0.20 nm and 0.03 nm for the ppm and ppb samples, respectively. The center wavelength of the ZPL for these two samples were 637.105 nm (ppm) and 637.022 (ppb). Figure 7.6c shows a close up of the ZPL in Fig. 7.6b.

The low temperature PL characteristics obtained from other samples in these two classes followed a similar trend to the one described in the previous section. Other than determining that there were NV centers within the sample region under investigation, PL measurements served the purpose of finding the location of the ZPL in the various samples. This dictated where the spectral location for the WGM resonances would need to be located after the microsphere was fabricated and cooled to liquid helium temperatures. The inhomogeneous linewidth of the ZPL gives a sense of what kind of deviation the WGM resonances could have from this value.

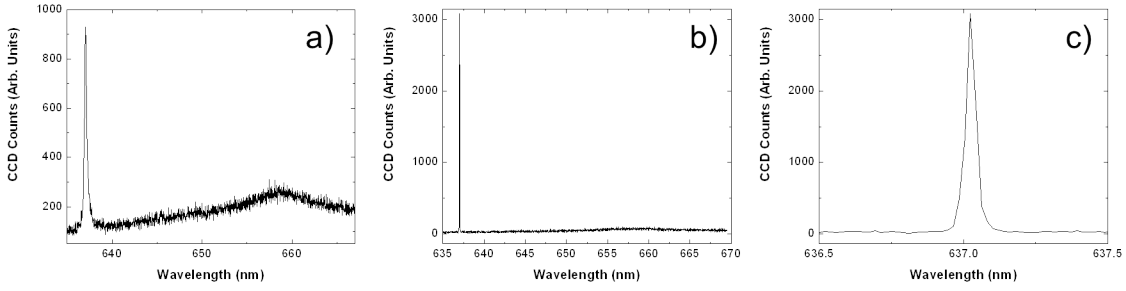


Figure 7.6: Photoluminescence spectra from NV centers in a) ppm and b) ppb concentration diamond substrates at 10 K. c) Spanned in view of the zero phonon line for the PPB sample.

Once a region in a sample was determined to contain NV centers, the resonant PLE approach could be used to study specific dipole transitions. It was possible to spectrally isolate single NV centers in both types of samples by resonantly exciting an optical transition that was far away from the center of the inhomogenously broadened ZPL. For the case of high-density samples it was necessary to work even further away from the center of the ZPL. This was due to the number of NV centers in the excitation and collection region of the microscope objective. When no RF field was applied to the sample, the transitions that were possible to excite corresponded to the two transitions that originate from the $m_s = 0$ state. These two transitions are the brightest of the six possible transitions and are labeled (1) and (4) in Fig. 6.4.

The PLE technique allowed for a direct measure of the homogenous linewidth of an NV center in either class of samples. Figure 7.7a and Fig. 7.7b shows the homogeneous linewidth of an optical transition for an NV center in both a ppm and ppb sample, respectively. It was experimentally determined that NV centers found in samples with ppm nitrogen concentrations typically had linewidths that were two to three times broader than those found in samples with ppb concentrations. NV centers found in the ppm samples were never observed to have linewidths narrower than 60 MHz. Typical values for the instantaneous linewidth were closer to 100 MHz. However, in these types of samples, NV centers were observed to have linewidths as broad as 140 MHz. This range of widths was consistent and fit a general trend regarding different samples within this class.

The linewidth of NV centers in samples with ppb nitrogen concentrations were typically sharper than 50 MHz. During the course of this research, the sharpest recorded

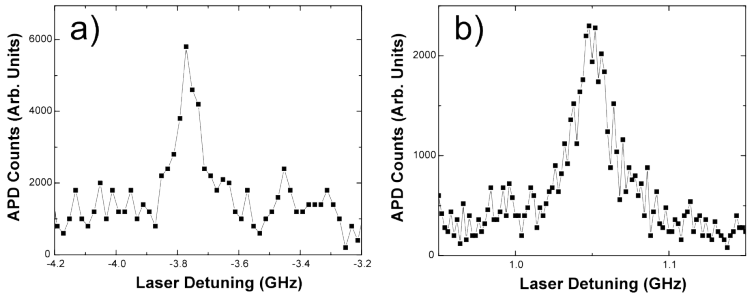


Figure 7.7: Linewidths of nitrogen vacancy centers in a) ppm and b) ppb sample at 10 K.

linewidths for NV centers were measured to be near 30 MHz. However, some transitions were found to be as broad as 60 MHz. Even when PL was measured from a specific region in a ppb sample, it would take time to find a signal from an optical transition in frequency space. Once a center was found, it could be scanned across repeatedly using the PLE technique to characterize the spectral stability of an NV center over time.

Figure 7.8 shows the spectral stability for the same NV center and same transition displayed in Fig. 7.7a above. Actually, Fig. 7.7a was just a single scan across this same transition but with a much slower scan rate. During these data acquisition cycles, the NV center was excited with the diode laser at a power of 50 nW and with a scan period of 40 seconds. This particular NV center was extremely stable over the course of 65 minutes and in a sense set a bar for stability. Most NV centers in ppb samples were bright and stable for less than 10 minutes. This was primarily a consequence of drift in the cryostat or from the NV center photo-ionizing. With the experimental set-up used during these studies, it was possible to re-optimize the coupling to a particular NV center during scans but over time it would eventually be lost.

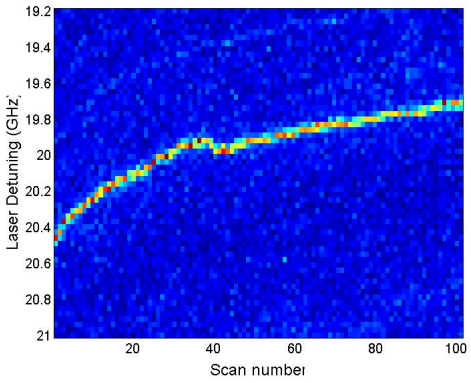


Figure 7.8: PLE stability plot from a NV center found in a ppb at 10 K.

Figure 7.9a and Fig. 7.9b are cross sectional plots from the beginning and end of the stability plot shown in Fig. 7.8. The linewidth for this transition fluctuated slightly during the scan and was on the order of 40 MHz. The center frequency for this particular transition drifted approximately 0.5 GHz over the entire measurement.

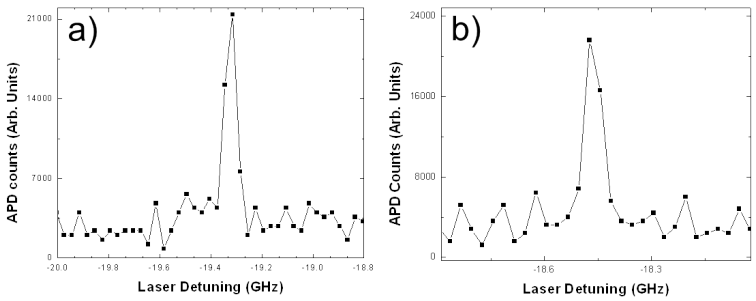


Figure 7.9: Two resonant excitation scans of the stability plot for the NV center studied in figure 6.7 where a) was the first plot and b) was the last scan.

Another sequence of PLE scans from a NV center in this same sample is shown in Fig. 7.10. This NV center had characteristics that were more typical of NV centers found

in ppb nitrogen concentration substrates. It should be noted that if the NV center was continuously excited on resonance, it would typically photo-ionize, or go into the dark metastable state within a few to tens of seconds. In terms of continuously exciting a transition, the longest time a NV center could be continuously excited without photo-ionizing was on the order of a minute. By scanning over the transition it was possible to study NV centers for longer periods of time without making the transition disappear.

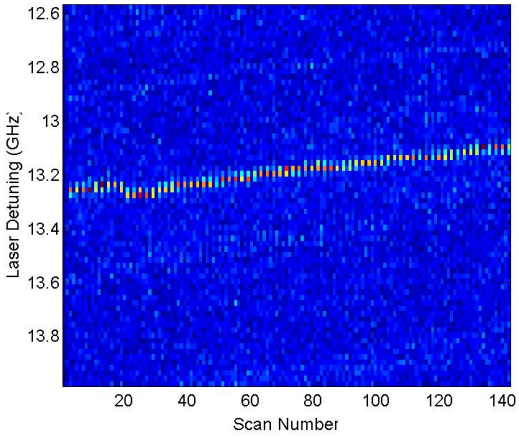


Figure 7.10: PLE stability trace for an optical transition for an NV center in a ppb sample at 10 K.

It was possible to study NV centers in samples that had a nitrogen concentration in the ppm range with the PLE technique. Figure 7.11 shows a sequence of PLE scans for the same NV center that was used in Figure 7.7b above. The NV center was excited with 50 nW of laser power with a scan rate of 0.1 Hz. As can be seen from this plot, the NV center was not spectrally stable and was only observed for 190 seconds.

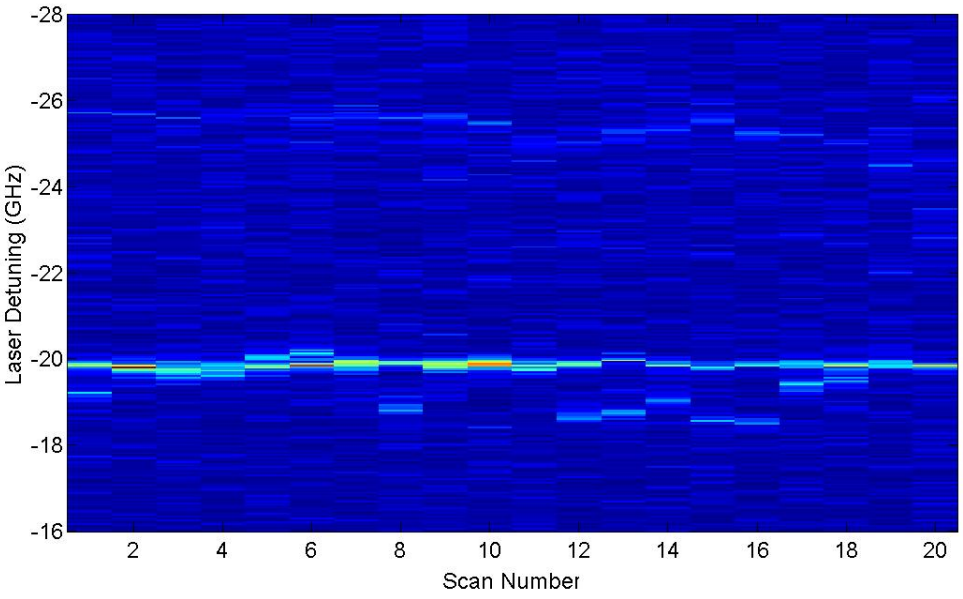


Figure 7.11: Photoluminescence stability plot for an NV center in a ppm sample at 10 K.

A spectral stability plot for another NV center, found in a different region of this same substrate is displayed in Fig. 7.12a. It was studied under the same experimental conditions as the previous NV center. The homogenous linewidth for this center was 90 MHz. The plots in Fig. 7.11 and Fig. 7.12 were typically for NV centers found in ppm samples. Within a given sample volume, and within a certain frequency space, NV centers could be located that were fairly stable and narrow. On the other hand, within a similar variable-space it was possible that no distinct NV center would be found or that the NV centers would be extremely unstable. Nitrogen vacancy centers in this class of diamond (ppm) typically showed large spectral fluctuations and went dark on the order of seconds to a few minutes.

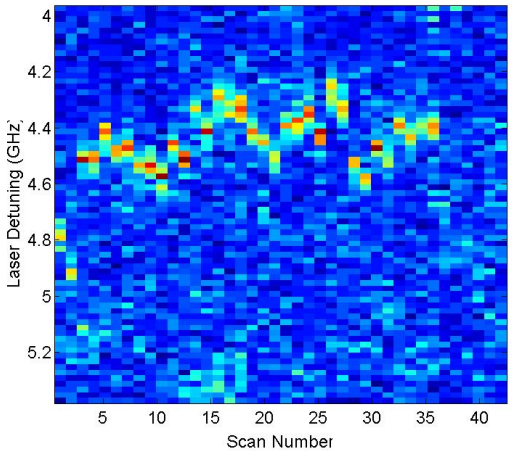


Figure 7.12: Another photoluminescence stability plot for an NV center in a ppm sample at 10 K.

For cavity-QED studies, it is extremely important that the transition frequency be spectrally stable, otherwise coupling a dipole transition to a cavity mode would not be possible. Therefore, NV centers with optical properties similar to those found in high purity diamond substrates should be used for cavity-QED studies. Also, the linewidths of these emitters are narrower than the other class of samples. Even when the coupling to a NV center was re-optimized, there was the case when the resonance frequency jumped for centers in ppb samples. This was thought to occur when an NV center lost an electron followed by recapturing another one from the lattice. It has been shown that a single NV center does fluctuate between the neutral and negatively charged versions [206]. In this study, the time scales where the NV center alternated its characteristics between the negatively charged version and the neutral, and then back were on the order of 100 ms and 10 ms, respectively.

If all NV centers exhibit this fluctuation between the two charged states, it was still possible to study them with the PLE method over long periods of time as has been

shown in this section. But if the local environment created charge traps near by, it may only be possible to study them for minutes or even less. Laser pulse sequences, alternating between 532 nm and 637 nm wavelengths, have been developed and implemented in other experiments in order to mitigate these issues. All of these factors indicate that is important to work with the cleanest samples, both in the sense of impurities and lattice damage.

## 7.6. Introduction to Irradiation Sections

The previous section makes it clear that ppm samples had a higher concentration of NV centers when compared to ppb samples. Unfortunately though, NV centers found in these samples were spectrally unstable. The high purity samples hosted spectrally stable emitters at a much lower density. However, a modest density of NV centers is required near the surface of a sample in order to fabricate diamond nanopillars that contain spectrally stable NV centers near the top of the pillar. One possible solution is to irradiate the surface of a ppb diamond sample with nitrogen ions (or molecules) at low energies and doses. In theory, if the contamination of and damage to the sample is minimized, stable NV centers could be induced near the sample surface.

This material modification technique could also be used to increase the interaction strength between the NV centers and the cavity mode [141, 186, 207]. For the lowest order radial mode of a silica microsphere resonator, the field intensity maximum is closest to the sphere surface. This maximum is just inside of the structure and the optical emitter interacts with an evanescent field that decays exponentially from the surface. In

order to have the strongest interaction strength between the cavity and the emitter, the emitter should be as close to the surface of the microsphere as possible. As was shown in the previous chapter, this decay length is roughly 100 nm for regular microspheres and approximately four times that for deformed resonators. In either case, the closer the NV center is to the surface of the microsphere the stronger the coupling rate is to the cavity. Investigations into the feasibility of this material modification approach for cavity-QED studies were done and in the following section, an approach to induce NV centers near the surface of the sample will be discussed. The last two sections of this chapter will discuss the PL and PLE studies of NV centers in regions of SCD substrates that were irradiated with high-energy nitrogen ions.

## 7.7. NV Centers Created via Ion Implantation

Low energy nitrogen (N+) ions were implanted in SCD substrates to induce NV centers near the surface. The samples were irradiated at Core Systems in Sunnyvale, California. The samples were then annealed in a tube furnace housed in Professor David Johnson's Laboratory in the Chemistry Department at the University of Oregon. The samples were irradiated with nitrogen ions having an energy of 14 keV or 100 keV. These energies were chosen to keep the implanted ions within the top 200 nm of the sample. The dose of the ion implantation was kept near the minimum available dose from the vender, so the density of defects and damage created by this process were kept relatively low. This range of doses corresponded to $10^{-9}$ to $10^{-7}$ ions per square centimeter. The samples were annealed at a temperature of 825° C. At temperatures

above 600º C and below 1150º C only the vacancies become mobile and migrate about the crystal lattice. This was done to help the vacancies pair up with either an implanted or native nitrogen atom to form an NV center.

Before irradiating the diamond samples with nitrogen ions, the process was modeled using a free software package called Stopping Range of Ions in Matter (www.srim.org) by Dr. James F. Zeigler. This software can model the implantation of ions into amorphous materials and was used to calculate the average depth the ions would be located and the amount of damage that would be caused per ion. Figure 7.13a shows distribution of 14 keV nitrogen ions implanted into the sample, while Fig. 7.13b show the number of vacancies produced per ion at this energy.

When 14 keV nitrogen ions were implanted into amorphous carbon, the projected implantation range was 30 nm below the surface. It was estimated that each ion produced approximately 140 vacancies along its trajectory. Figure 7.13c and Fig. 7.13d show similar plots for 100 keV nitrogen ions. In this case, an ion was projected to be implanted 180 nm below the sample surface, with an estimated 410 vacancies created along a given path length. In order to make SCD diamond look like amorphous carbon to the incoming ions, the samples were tilted slightly and rotated during the irradiation. If this was not done the ions could be channeled through the lattice and the vertical distribution would not resemble those in Fig. 7.13.

This concept is called ion channeling and typically ions would be able to propagate much deeper into the substrate. The samples were tilted at 7 degrees from the

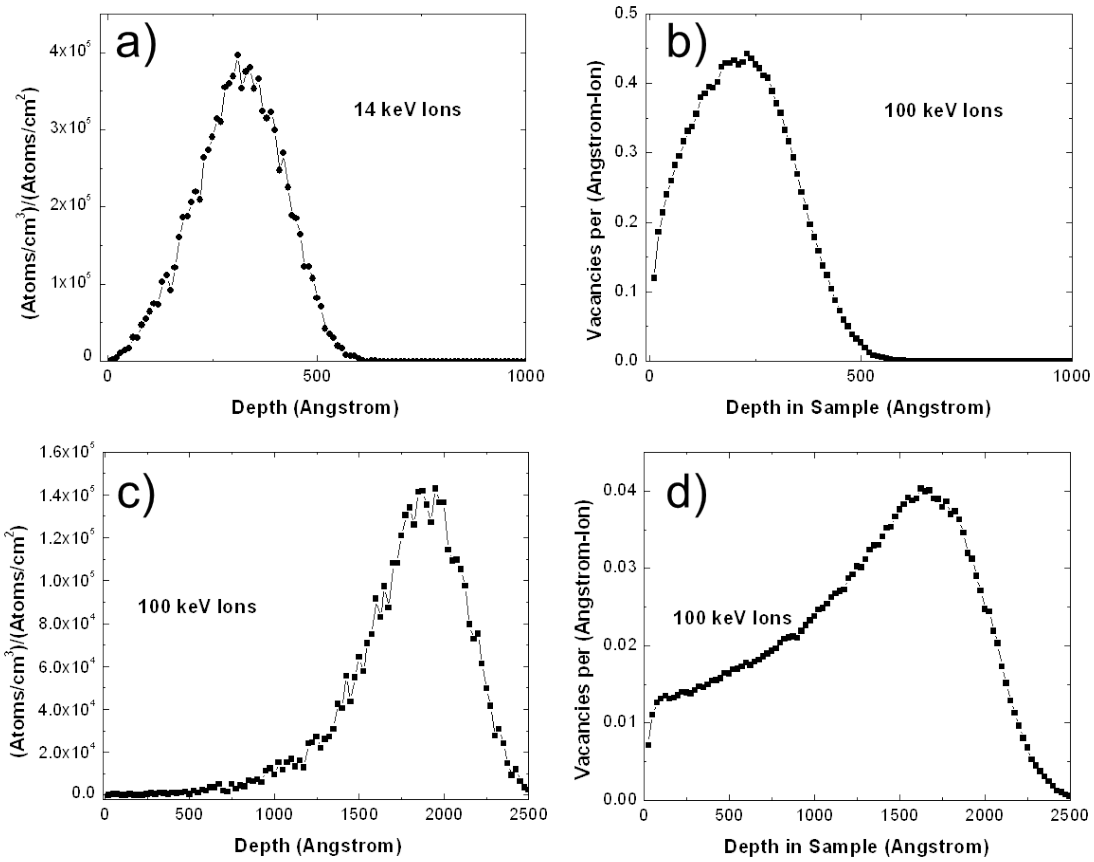


Figure 7.13: A simulated plot showing the a) vertical distribution of nitrogen ions and b) vacancies/ion when amorphous carbon is irradiated with 14 keV nitrogen atoms. A similar set of plots showing the c) vertical distribution of nitrogen ions and d) vacancies per ion when amorphous carbon is irradiated with 100 keV nitrogen atoms.

implantation direction and rotated at 3600 RPM while being irradiated in order to avoid the problem of ion channeling. The sample temperature was maintained at 20° C while being irradiated. A portion of the sample was masked with a piece of copper tape in order to maintain a reference for later measurements. With the number of vacancies out numbering the number of implanted nitrogen atoms, and considering the fact that not every ion sits at a lattice site, it was obvious that each implanted ion would not generate

an NV center. After the irradiation process, the samples were annealed at 825º C for 85 minutes.

## 7.8. Photoluminescence from Single Crystal Diamond Irradiated with Nitrogen Ions

Figure 7.14a shows the PL spectrum from a region of a ppm substrate that was not irradiated with nitrogen ions but was annealed at 825 C for 1.25 hours. Figure 7.14b shows PL from the same substrate, using the same power and integration time, from a region that was irradiated with 100 keV nitrogen ions with a dose of $1 \times 10^{-8}$ ions per square centimeter. These spectra were taken 10 microns away from one another. The sample was at 10 K for these two measurements. When irradiating ppm class samples with these low doses no appreciable change in the ZPL linewidth or intensity was observed. This was observed in all ppm samples that were irradiated with 100 keV ions when doses less than $5 \times 10^{-8}$ per square centimeter were used. In another ppm sample that was irradiated with 100 keV nitrogen ions and at a dose of $1 \times 10^{-7}$ ions per square centimeter a noticeable change in the ZPL intensity of the neutral and negatively charged states of an NV center was observed.

Figure 7.15a shows the PL obtained at 10 K on a portion of a sample that was not irradiated but annealed. When a PL spectrum was taken from an irradiated section of this sample, ten microns away from where Fig. 7.15a was taken, a decrease in the ZPL intensity was observed. These data are shown in Fig. 7.15b and all of the other conditions

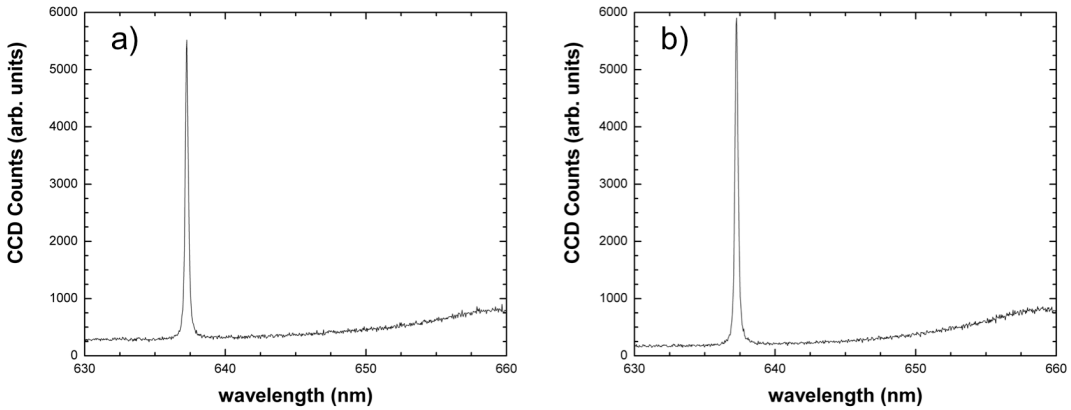


Figure 7.14: Photoluminescence spectra at 10 K from regions of a ppm nitrogen content sample that a) was not and b) was irradiated with 100 keV ions at a dose of 1 x $10^{-8}$ per square centimeter.

were kept the same from Fig. 7.15a. However, what is more noticeable was an increase in the ZPL intensity for the neutrally charged NV center (at 575 nm) and Raman line (at 572 nm). The phonon sideband also appears to have increase in signal.

For both of these spectra, the samples were excited with 10 mW and an integration time of one second was used. Spectra with similar characteristics were observed around these two locations. Data taken from another ppm diamond substrate showed a similar trend. It appeared that the number of negatively charged NV centers actually decreased when the irradiation dose was higher than 5 x $10^{-8}$ ions per square centimeter for 100 keV nitrogen ions. Also, under these same conditions, the undesirable

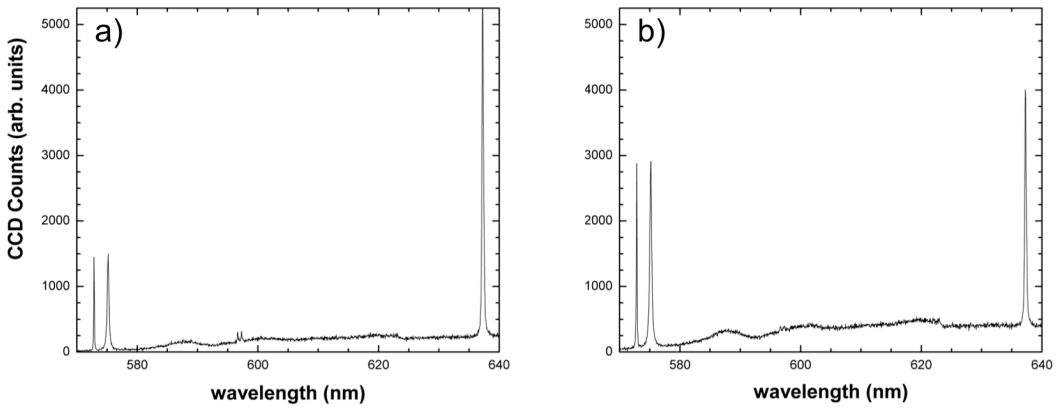


Figure 7.15: Photoluminescence spectra at 10 K from regions of a ppm nitrogen content sample that a) was and b) was not irradiated with 100 keV ions at a dose of 1 x $10^{-7}$ per square centimeter.

effect of creating more neutral NV centers was consistently observed.

Samples with nitrogen content in the ppb regime were also irradiated with nitrogen ions to induce NV centers. The doses used to implant ions were kept at, or below $1x10^{-8}$ ions per square centimeter. Figure 7.16a shows a PL spectrum from a region of a ppb sample that was irradiated with a dose of $1x10^{-8}$ ions per centimeter squared. For these data, the energy of the implanted nitrogen ions was 100 keV and the samples were annealed at 825° C for 1.5 hours. The excitation power was 100 mW with an integration time of one second. Also, these data were acquired with the samples at 10 K. Figure 7.16b is a PL spectrum of the same diamond sample that was in a non-irradiated section of the sample, 10 microns away from where the data in Fig. 7.16a was taken. However, in this case the integration time was 10 seconds.

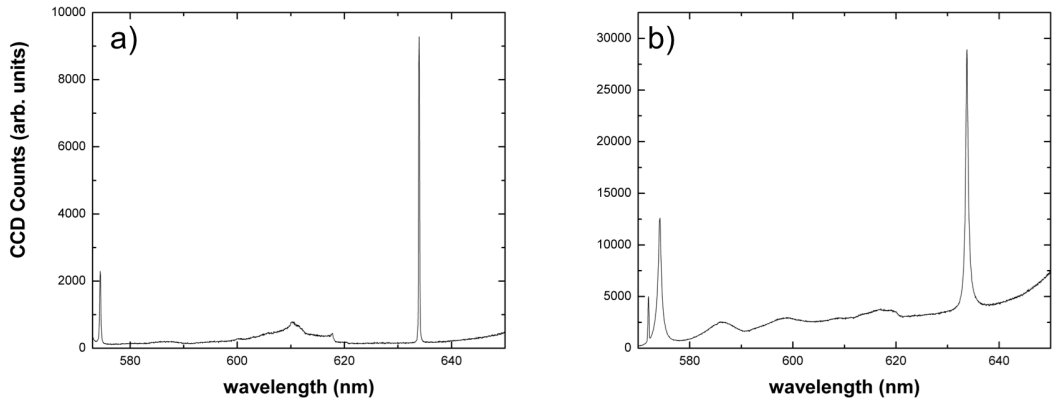


Figure 7.16: Photoluminescence spectra at 10 K from regions of a ppb nitrogen content sample that a) was and b) was not irradiated with 100 keV ions at a dose of 1 x $10^{-8}$ per square centimeter. The integration time for the spectrum in the second figure was 10 times longer than that of the first figure.

Again, the most noticeable difference was the change in $NV^-$:$NV^0$ ratio for the ZPL intensity. Before irradiation, the ZPL ratio was roughly 5:1. In regions where the irradiation had occurred the ratio was less than 3:1. A common feature for ppb samples that were irradiated under these conditions was that the ensemble linewidth of the ZPL for the negatively charged NV center increased in regions where the irradiation had occurred. Second, there was an increase in the phonon sidebands for both charged states. Another high purity substrate was irradiated with 14 keV nitrogen ions at a dose of $5x10^{-9}$ ions per square centimeter. Spectra from this sample are shown in Fig. 7.17. The PL was collected from the sample when it was at 10 K. For both plots, a laser power of 25 mW was used with an integration time of 10 seconds. Again, there was a greater increase in the number of neutral NV centers than the negatively charged version, with nearly a seven-fold increase in the intensity.

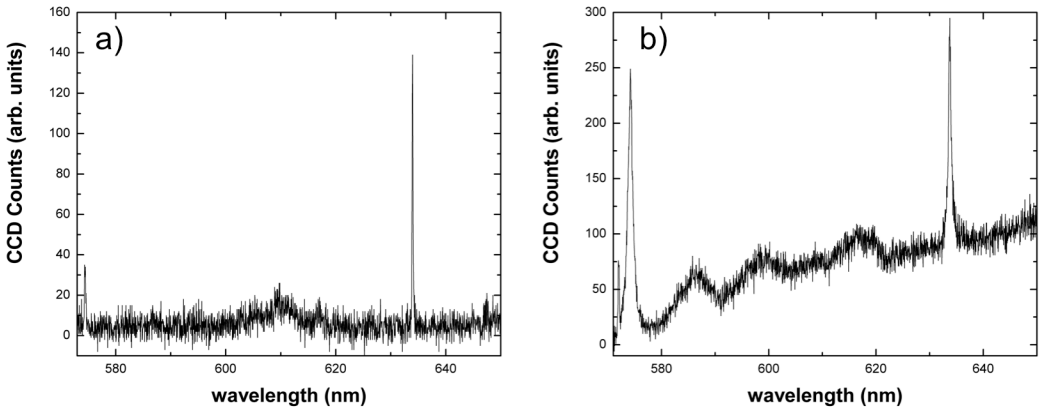


Figure 7.17: Photoluminescence spectra at 10 K from regions of a ppb nitrogen content sample that a) was and b) was not irradiated with 100 keV ions at a dose of 5 x $10^{-9}$ per square centimeter.

The ZPL for the negatively charged NV center nearly doubled after the irradiation and annealing process. The more obvious difference was the in the irradiated sections of the sample the ZPL linewidth for both of the NV center charged states had increased. In the sections of the sample that were not irradiated, the linewidth for neutral and negatively charged version of the NV center was approximately 0.3 nm and 0.2 nm, respectively. In the irradiated sections of the sample, the ZPL linewidths were nearly 1 nm and 0.6 nm for the neutral and negatively charged centers, respectively. There was also an increase in the phonon sideband for both of the charged states.

## 7.9. Photoluminescence Excitation of Irradiation Induced Nitrogen Vacancy Centers

The sample used for the data presented in Fig. 7.17 was also studied using the photoluminescence excitation technique. Figure 7.18 shows a PLE trace of an NV center

that was in the implantation region of this sample. The laser wavelength was near 637 nm and had an excitation power that was 25 nW. The time for each scan was 40 seconds and these data were taken at 10 K. As can be seen from this plot the NV center exhibited large spectral fluctuations. Also, at some points during the measurement there were small jumps in the resonant frequency of the emitter. However, this particular NV center stayed bright for 1,400 seconds. Only a few NV centers found in regions of the sample that were irradiated with nitrogen ions could be studied for this extended period of time. It appears as though NV centers that were created via the irradiation process were only slightly more prone to photo-darkening when compared to native NV centers in ppm samples.

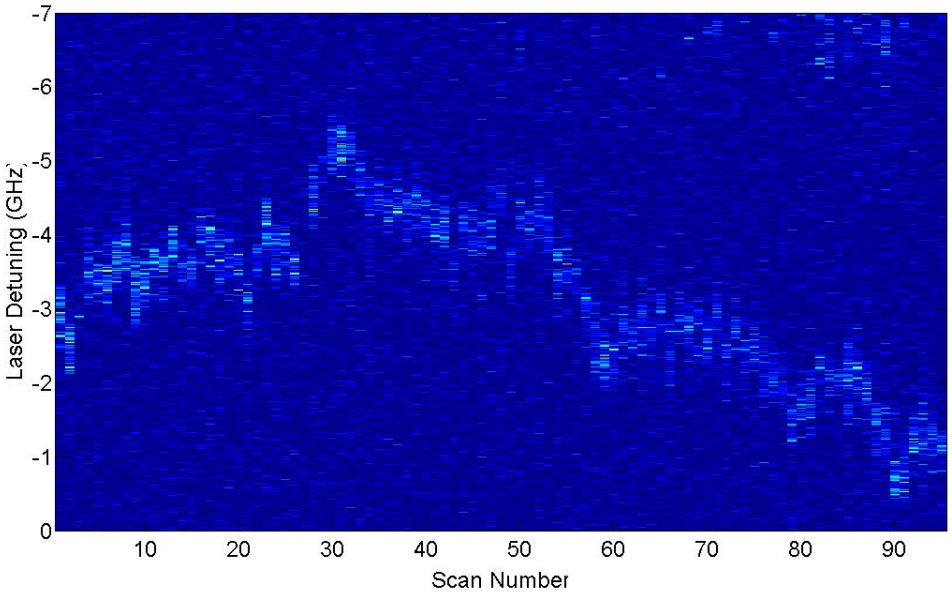


Figure 7.18: A photoluminescence excitation stability plot of an NV center in a region of a ppb diamond substrate that was irradiated with 100 keV nitrogen ions. The laser power was 25 nW and each scan lasted 40 seconds.

It should also be noted that the spectral fluctuations of the irradiation-induced centers were no greater than NV centers that were typically found in ppm SCD substrates. It was obvious that in regions of the sample that were irradiated, centers had less spectral stability than NV centers that were found in un-irradiated regions of the sample. This was consistent for either 100 keV or 14 keV irradiation energies, regardless of the dose. Another feature that irradiation induced NV centers had, and which made them a poor candidate for cavity QED studies was their broad linewidths.

Figure 7.19 shows a single scan across an NV center created via this irradiation process when the lowest ion dose ($1x10^{-9}$ ions per square centimeter) was used. The linewidth of the emitter was greater than 200 MHz. This linewidth was more than double the typical linewidth of NV centers found in ppm samples and as much as six times larger for NV centers typically found in ppb samples. For the energies and doses used the features for the optical linewidth shown in Fig. 7.19 below was indicative of all NV centers that were in regions were nitrogen ions were implanted.

During these studies, it was easiest to excite native NV centers in ppb samples. NV centers in ppm samples were difficult to spatially and spectrally isolate. There were typically too many resonances to distinguish a signal from an individual center. NV centers in irradiate regions of the sample were slightly easier to study than the previously mentioned case but typically went dark and were spectrally unstable. These issues render NV centers induced via irradiation (under these experimental conditions) unfit for cavity-QED studies.

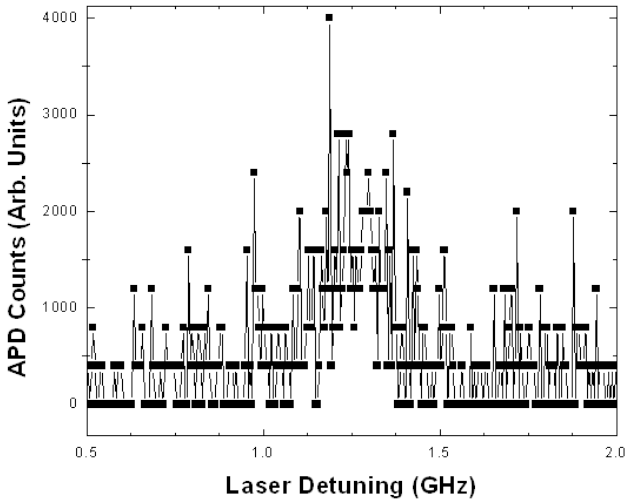


Figure 7.19: A single scan across an NV center in a region of a ppb sample which had been irradiate with 100 keV nitrogen ions with at a dose of $1x10^{-9}$ per square centimeter. These data were taken at 10 K.

# CHAPTER VIII

# DIAMOND NANOPILLARS

This chapter addresses the methods used to fabricate diamond nanopillars from single crystal diamond (SCD) substrates used in the composite cavity quantum electrodynamics (cavity-QED) system for this dissertation. Diamond fabrication techniques at the micro- and nano-scale have matured in the past decade [208, 209, 210, 211, 212]. The samples used to fabricate the diamond nanopillars were commercially purchased SCD substrates that were grown using a chemical vapor deposition (CVD) technique and were purchased from Element 6 (www.e6cvd.com). For this work the typical substrate size was 3.0 x 3.0 x 0.5mm. Samples with a nitrogen concentration less than 1 ppm had a surface finish with a roughness average (Ra) that was less than 30 nm. For the high purity SCD with a nitrogen concentration less than 5 ppb, the surface roughness had a Ra that was less than 5 nm.

Section 8.1 will discuss the first approach that was taken to fabricate diamond nanopillars from CVD grown diamond. This method utilized electron beam lithography (EBL) with a positive electron beam (e-beam) resist. After the pattern was developed, an aluminum coating was evaporated onto the sample surface to fabricate a mask. The mask served to protect the diamond beneath it while the exposed diamond was etched with a reactive ion etcher (RIE). Section 8.2 lays out another approach in fabricating diamond nanopillars from SCD. This second method used a negative e-beam resist as the mask

when the exposed diamond was etched with an inductively coupled plasma reactive ion etcher (ICP-RIE).

A technique for covering the bulk diamond substrate with gold, while exposing the diamond pillars through this metal layer, will then be described in section 8.3. This was done in an attempt to eliminate the excitation and collection from NV centers that were not in the diamond nanopillars. The two sections that follow will present the PL and PLE data taken from nanopillars fabricated from SCD substrates with either ppm or ppb nitrogen concentrations. The final section of this chapter presents PL and PLE data taken from diamond nanopillars that were etched from irradiate regions of ppb diamond substrates.

## 8.1. Metal Mask Diamond Nanopillar Fabrication

Arrays of diamond nanopillars with various diameters were fabricated on the surface of diamond substrates in such a way that a fused silica microsphere could be brought in contact with a single pillar at a time. In order to produce nanometer-sized pillars, standard EBL and lift-off techniques were employed to pattern an aluminum mask on the surface of the diamond. The mask consisted of 200 nm thick aluminum discs with varying diameters. The diameters ranged in size from a few hundred nanometers up to 2 microns. The chemical inertness and hardness of diamond requires an RIE to etch the exposed diamond surface with an argon and oxygen gas mixture at room temperature. With this processing technique, diamond pillars were fabricated which were 1.2 microns tall. The resulting nanopillars had diameters as small as 200 nm and as large as 1 micron.

A summary of the steps required in fabricating diamond nanopillars from SCD is depicted in a flow chart style in Fig. 8.1.

The first step in the process flow was to mount the small piece of diamond onto a larger silicon chip; the sizes of the silicon chips were approximately10x10x0.05mm. Doing this made it easier to handle the small diamond substrate during the various fabrication steps. Also, mounting the diamond substrate onto the silicon chip helped dissipate charge from the diamond when imaging or writing patterns on its surface with the scanning electron microscope (SEM). To mount the diamond substrate, a thick layer (~0.25mm) of polymethyl methacrylate (PMMA, 495 PMMA A Resist, 5% in Anisole, MicroChem Corp) was spun onto a clean silicon chip.

Once the diamond was mounted on the silicon chip with the PMMA, it was baked in a convection oven at 170˚ C for 5 minutes. This baking was done in order to remove the solvents from the PMMA to harden it. Following this step, a 300 nm layer of PMMA was spin coated on the diamond surface. To get this thickness of PMMA on the surface of the diamond, the sample was accelerated from 0 RPM to 3,500 RPM at 2,000 RPM/second. Once the sample reached 3,500 RPM it was held at that speed for 60 seconds. The sample was decelerated to 0 RPM at 2,000 RPM/second. After this spin coating process the sample was baked in a convection oven at 170˚ C for 30 minutes.

Once the sample was coated with PMMA a thin layer of gold approximately 10 nm thick was evaporated onto the surface of the diamond and the silicon chip. This layer of gold was put down to further aid in the dissipation of the electrical charge that could build-up on the diamond chip. The silicon chip with the diamond substrate was then

mounted into a Zeiss SEM adapted with a nanometer pattern generation system (NGPS) used for EBL. To produce an array of circles with diameters varying in size from 300 nm to 2 microns, the PMMA was exposed to electrons at a dose of 1,600 C/cm$^2$ and an accelerator voltage of 30 keV. A 10 micron diameter aperture was used on the SEM. It should be noted that the PMMA was exposed through the gold conductive layer. However, before developing the PMMA, the gold conductive layer was removed with a one-to-one-hundred-ratio solution of X20 Gold Etch (Fuji Film) to deionized (DI) water. The sample was the rinsed with DI water and then dried with a nitrogen gas gun.

Following this step, the PMMA was developed in a one-to-three ratio solution of methyl isobutyl ketone (MIBK) to Isopropanol (IPA) for 60 seconds. The developer solution was at a temperature of 20˚ C. The development of the PMMA was stopped in IPA and then blow-dried. This procedure produced the positive image of the mask that was to be created out of aluminum. A lift-off technique was used to produce an Aluminum mask for the etching process. The first step of the lift-off technique was to deposit 200 nm of aluminum onto the surface of the diamond in an evaporator (Edwards) at a rate of 0.5 nm per second. Afterwards, the diamond substrate was placed in acetone to dissolve the PMMA and lift-off the aluminum that was not directly evaporated onto the diamond surface. Aluminum has a strong adhesion to diamond, and very little of the Aluminum that was in contact100with the diamond surface came off during the liftoff process. Figure 8.2 shows an SEM image of a 200 nm aluminum disk produced with the method described above.

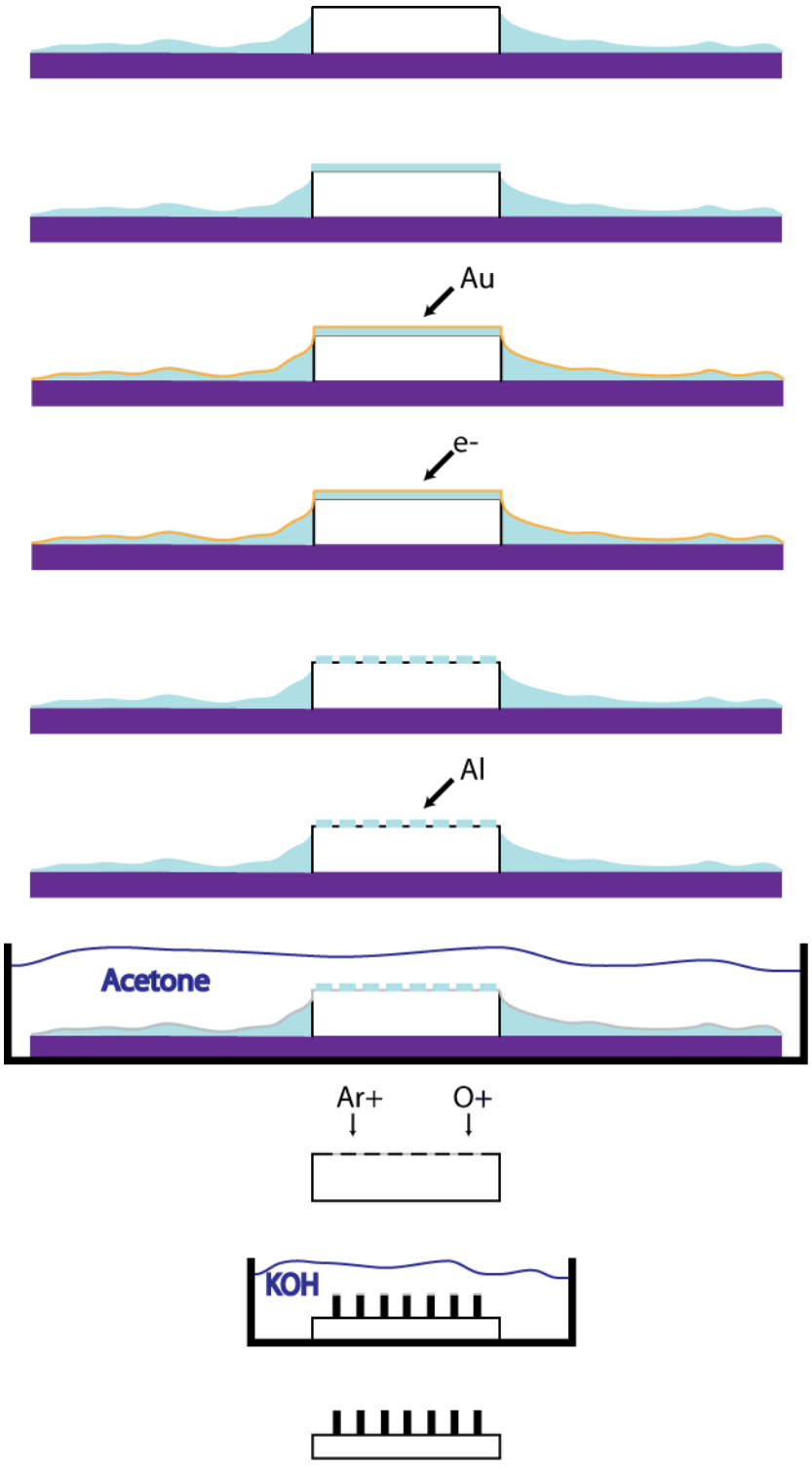


Figure 8.1: A flow chart showing the mask fabrication and diamond etching process.

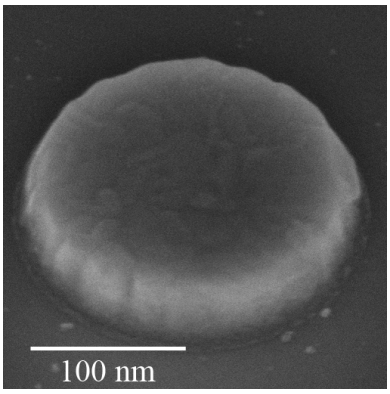


Figure 8.2: A scanning electron microscope image of an Aluminum mask that was fabricated with electron beam lithography and a lift-off technique. The mask diameter is approximately 1 micron.

To etch the exposed diamond and produce diamond nanopillars an RIE (Plasmatherm System VII) was used at Oregon State University (OSU) in Professor John Wager's lab. This system was a very basic RIE and Fig. 8.3 is a drawing of the chamber where the etching occurs. The concept of an RIE is fairly straightforward. An evacuated chamber is filled with the appropriate gas(es) for etching the sample. This is done at a specific flow rate until the chamber reaches the desired pressure. Once the gas rates and pressure reach a steady state, a high power radio frequency electromagnetic field is applied to the wafer plate. Nearly instantaneously, plasma is created in the chamber. During this process, a large potential difference between the ground plate and the wafer plate develops.

This large potential difference between the ground plate and the wafer plate causes the ions to accelerate towards the wafer plate that then chemically reacts with the sample. Also, the ions can cause the physical removal, or sputtering, of the sample

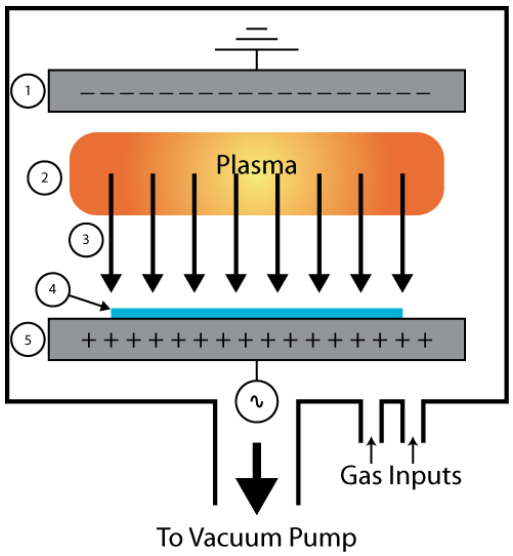


Figure 8.3: A diagram depicting reaction ion etching components. Gases are pumped in and pumped out via gas inputs and a pumping port, respectively. The top plate (1) is grounded while the bottom plate (5) is driven at a RF frequency. This produces a plasma (2) which is accelerated (3) by the bottom plate to the sample (4) which is then etched by the plasma.

material. In the case of this fabrication technique both methods of etching were used. When the diamond samples were etched with the Plasmatherm VII at OSU an oxygen and argon gas mixture was used. The oxygen was used as the reactive etchant while argon was used as a physical etchant. The gas mixture had a flow rate of 5 standard cubic centimeters per minute (sccm) for both the Ar and $O_2$ gas. This was done while maintaining a chamber pressure of 5 milliTorr. A radio frequency signal at a power of 400 W was applied to the wafer plate, which resulted in an 830 V DC potential between the wafer plate and the ground plate.

With these parameters, the resulting etch rate was approximately 20 nm per minute for the diamond substrate and 2 nm per minute for the aluminum mask. The diamond was etched for 45 minutes, which resulted in 1.2 micron tall pillars with

diameters ranging from 1 micron down to 200 nm. The mask was subsequently removed using a Potassium Hydroxide solution. A 10% buffered oxide solution can also be used to remove the aluminum mask without affecting the diamond nanopillars. A set of SEM images of the resulting pillars is shown in Fig. 8.4 after the aluminum was removed.

As can be seen in these SEM images, the pillars were tapered and had significant sidewall roughness. Also, the shapes of the diamond pillars were not as circular as the mask pattern was. This implied that the mask did not sputter at the edges uniformly and the shape of the eroding mask was transferred to the sidewalls of the nanopillar. It should be noted that the 1 micron and 200 nm diameter pillars were fabricated from 2 micron and 400 nm diameter aluminum masks, respectively. Smaller aluminum mask features did not survive this etching process. As can be seen from the SEM images, the top of the pillars were unaffected by the etching process indicating that the Aluminum mask was effective near its center.

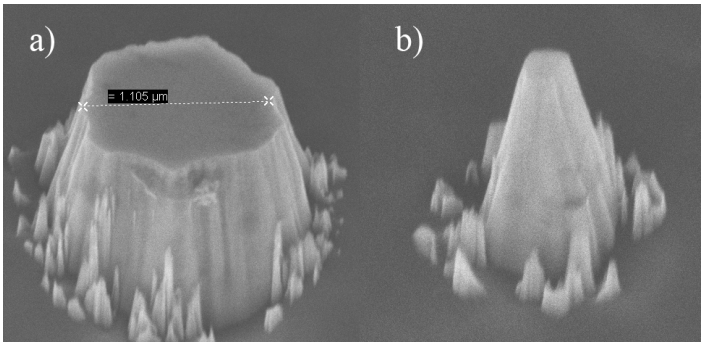


Figure 8.4: Two scanning electron microscope images showing a) 1 micron diameter diamond pillar and b) a 200 nm diameter pillar fabricated from single crystal diamond as is described in this section.

## 8.2. Hydrogen Silsesquioxane Mask Used in Fabricating Diamond Nanopillars

This section focuses on the fabrication of diamond nanopillars on the surface of SCD substrates using a negative tone e-beam resist based on Hydrogen silsesquioxane (HSQ). More specifically, the negative tone resist was FOX®-17 Flowable Oxide from DowCorning. Similar to the work in the previous section, the patterning of the mask on the surface of the diamond substrate was accomplished with EBL. However, the exposed substrate was etched with an ICP-RIE.

A flow chart of the process is displayed in Fig. 8.5. Another major difference from the previous section was the method that was used to fabricate the mask on the diamond surface. With this procedure fewer steps were require after the e-beam resist was developed before the sample was ready to be etched in the ICP-RIE. In comparison to the previous section, after the PMMA was developed the actual mask material had to be evaporated onto the PMMA. Then a lift-off technique was used to produce the desired mask pattern.

The initial steps taken to produce diamond nanopillars out of SCD with HSQ were similar to the previous section. However, those steps will be repeated here for clarity. The first step to produce diamond nanopillars from the CVD diamond was to mount the diamond onto a larger silicon chip that was approximately 10x10x0.05mm in size. To mount the diamond substrate, a thick layer (~0.25mm) of PMMA was spun onto a clean silicon chip. The diamond substrate was then placed onto the PMMA and pressed down with a pair of clean tweezers. This was done to insure the sample was level and in

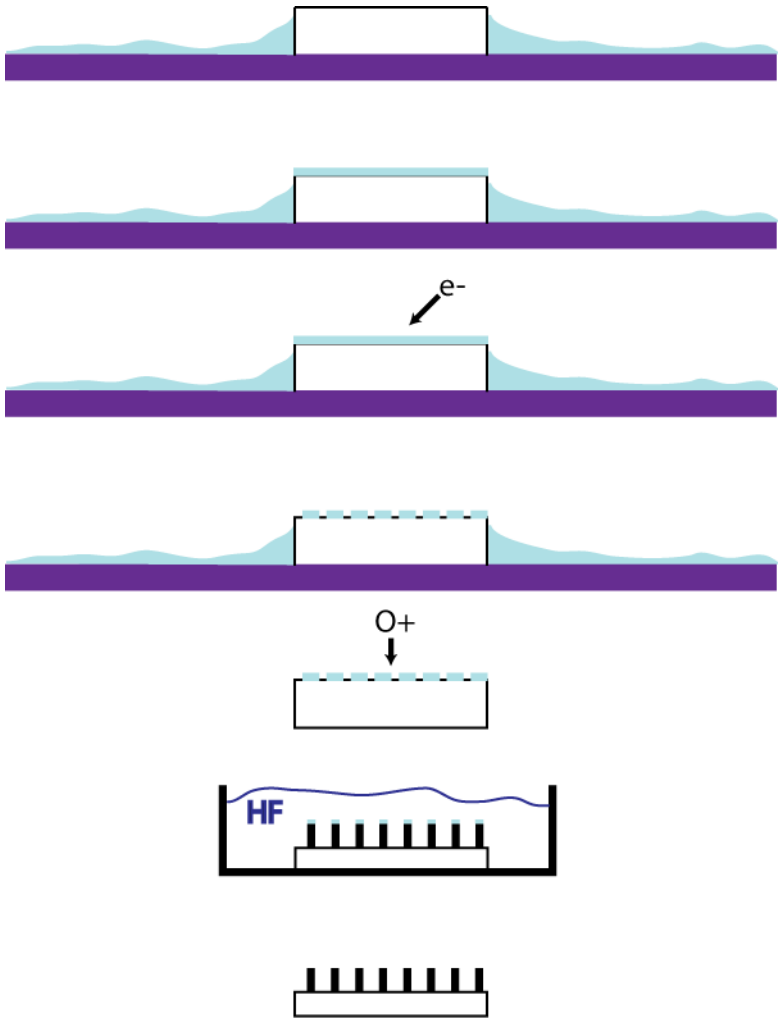


Figure 8.5: A flow chart showing the mask fabrication and diamond etching process.

good contact with silicon chip. Care was taken to avoid having any of the PMMA flow onto the diamond surface.

Once the diamond had been placed on the silicon chip, it was baked in a convection oven at 170˚ C from 5 minutes. Afterwards, a hexamethyldisilazane (HMDS) priming oven was used to coat the sample in order to help the HSQ resist adhere to the diamond surface. Then the HSW e-beam resist was spin coated onto the diamond surface. Before spin coating the diamond substrate with the HSQ, the HSQ was removed

from the refrigerator (~5° C) for 20 minutes. To achieve the desired thickness of HSQ, it was spin coated onto the diamond substrate under very specific conditions. The sample was accelerated to 3,000 RPM at a ramp rate of 2,040 RPM/second and then was held at that value for 45 seconds. After 45 seconds the sample was ramped down to 0 RPM at a rate of 2040 RPM/second. This resulted in a 350 nm thick resist layer.

Immediately after spin coating, the sample was pre-baked at 400° C for 60 seconds on a hot plate. After coating the diamond substrate with HSQ, a layer of ESPACER-300 (Showa Denko) was spun onto the sample to help dissipate charge from the surface when imaging or writing a pattern with the SEM. ESPACER is a water-soluble organic charge dissipation compound that can be used when nonconductive sample are processed with either EBL or simple SEM imaging. The ESPACER was spun on the sample under the same conditions as the HSQ with the only exception being that there was no pre-baking of this layer before writing the pattern with the SEM.

The pattern consisted of an array of circles varying in diameter and was written with a Raith-150 SEM. The pattern was written with an electron dose of 3,200 C/cm$^2$ and an accelerator voltage of 30 keV. An aperture size of 10 microns was used when imaging the diamond during the alignment and writing process. Once the pattern was written with the SEM, the ESAPCER was removed with DI water and then dried with a nitrogen gun. HSQ is typically developed in MF-CD-26 (MICROPOSIT™ MF™ -CD-26 Developer, Rohm and Haas Electronic Materials LLC) at 50˚ C for 60 seconds while being agitated. Submerging it in water while agitating it for 60 seconds can then stop the development of the pattern. However, there were technical issues with the use of HSQ

on CVD grown SCD that required a modified development process of the exposed e-beam resist.

The first issue was related to the weak adhesion of HSQ to the diamond substrate. Similar to glass substrates, the surface chemistry of diamond can be such that some metals and resist do not adhere well to their surface. To get around this issue, it was determined that the surface of the diamond needed to be hydrophobic before priming the diamond surface with HMDS. Therefore, before mounting diamond substrates onto the silicon chip they were cleaned in a 10% buffered oxide solution for five minutes. The second issue of developing HSQ patterns with MF-CD-26 for diamond applications was the fact that features smaller than 200 nm in width that had a width-to-height aspect ratio greater than 1:1 would collapse or lift-off.

The goal of this fabrication process was to create diamond nanopillars with diameters as small as 140nm. With this requirement the thickness of the HSQ mask needed to be 300 nm to survive the ICP-RIE etching process. The pattern collapse issue was resolved by reducing the surface tension of the developer with IPA. The exposed HSQ was developed in MF-CD-26 solution where 30% by volume of the developer was replaced with IPA. The DI rinse was also modified this way to reduce the surface tension minimizing the amount of the pattern that collapsed.

Using the above fabrication technique, arrays of circles were patterned from HSQ on the surface of the SCD substrates. They were 350nm thick with diameters ranging in size from 100 nm to 5 microns. Figure 8.6 is an SEM image of a 140 nm diameter circle patterned with HSQ. The pattern size was written to be 150 nm but the diameter reduced

in size by a small amount after the samples were developed and post-baked on a hot plate for 30 minutes at 400° C, which was done to harden the mask before the etch.

Once the HSQ mask pattern was written, developed and hard baked, the diamond sample was etched in the ICP-RIE. The main difference of an ICP-RIE and a conventional RIE is that there is a separate RF source that couples to the low-pressure gas in the chamber. This second RF source increases the plasma density over the sample. An increase in the density of the reactive species can be beneficial in many ways but it depends on the material being etched and the recipe implemented to etch it. In the case of SCD, the increased density of the reactive species had many benefits. First, the etch

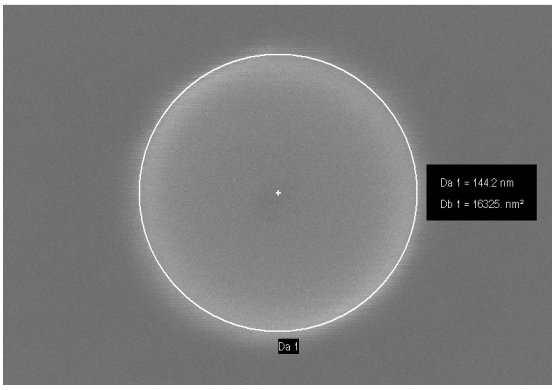


Figure 8.6: A scanning electron microscope image of an HSQ mask after exposure and developments. The diameter is approximately 140 nm.

time was greatly reduced compared to the previous section; it only took 10 minutes to etch 2 microns of diamond compared to 45 minutes to etch 1 micron when a conventional RIE was used. Second, there was no need to add argon during the etching process when using an ICP-RIE. This resulted in a decrease of the mask erosion rate; the mask choices,

aluminum or HSQ, are both relatively inert to $O_2$. Reducing the mask etch rate allowed for a thinner mask making it easier to devise a fabrication procedure to produce an HSQ mask pattern on SCD.

The parameters used to etch the diamond substrate were experimentally determined. In our process flow, the sample was still mounted on the small silicon chip which was itself mounted on a 4 inch silicon dioxide wafer with Kapton® tape (DuPont). This larger wafer was loaded into an Oxford Plasmalab 100 (Oxford Instruments) and was maintained at 20° C during the etch process. The oxygen flow rate was set to 30 sccm and the chamber pressure was held at 10 milliTorr. Once the chamber pressure and gas flow rate reached equilibrium and was held for 60 seconds, the RIE RF power was set to 100 W, resulting in a DC voltage of 253 V. The ICP RF power was set to 700W.

Under these conditions, the SCD was etched at 200 nm per minute while the HSQ mask etched at approximately 10 nm per minute. The 1:20 etch ratio of diamond to HSQ was an improvement over the 1:10 etch ratio in the previous section. More importantly though, the resulting diamond nanopillar sidewall surface roughness was decreased and its overall taper was reduced using the ICP-RIE. This can be seen in Fig. 8.7, which displays two SEM images of a diamond nanopillar with a 140nm diameter at the top. Figure 8.7a shows the entire nanopillar with the HSQ mask on top. As can be seen from this image, only a slight taper appears at the top nanopillar. However, there was a slight bulge in the middle. The nanopillar had a 100 nm diameter at the top and a 140 nm diameter at the bottom of the taper near the tip. The diameter at the bulge and the base of the nanopillar was 165 nm and 190 nm, respectively. This characteristic shape was found on all of the nanopillars with a diameter less than 500 nm.

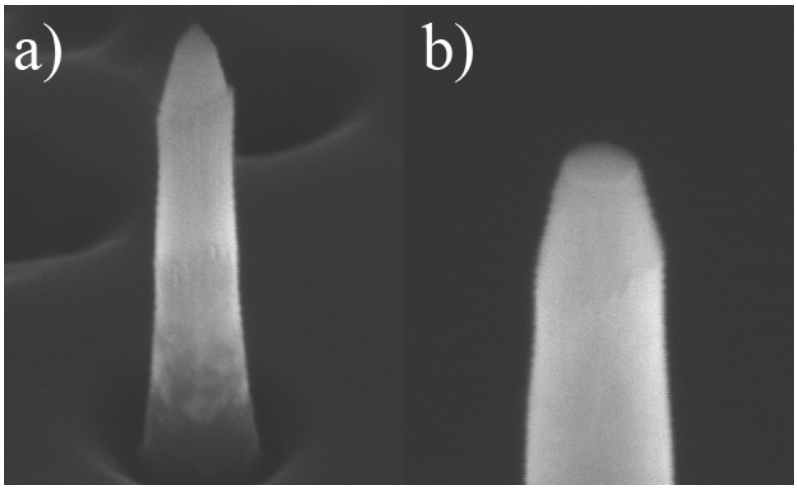


Figure 8.7: a) An SEM micrograph of a 140 nm nanopillar fabricated using an HSQ mask with the mask still on the pillar. b) An SEM micrograph of a 140 nm pillar with the mask removed.

## 8.3. Using Gold as a Mask for the Bulk

Before the diamond nanopillars were optically characterized, gold was used to cover the bulk diamond substrate. This was done to insure that any optical signal that was detected originated from the nanopillars. A fabrication technique was developed that exposed diamond nanopillars from the 100 nm thick layer of gold that was evaporated onto the SCD. A process flow chart is shown in Fig. 8.8. The first step was to mount the small diamond substrate onto a larger silicon chip. Next, a 100 nm thick layer of gold was evaporated (Key Evaporator) onto the entire diamond surface at a rate of 0.2 nanometers per second. To avoid any shadowing affects by the pillar the sample was tilted at 25 degrees and rotated at 60 RPM.

After the entire diamond surface was covered in a 100 nm gold layer, a 1,100 nm thick layer of PMMA was spun onto the surface. To accomplish this, two consecutive layers of PMMA (5% in Anisol) were spun on. For the first spin coating process, the sample was accelerated at 2000 RPM/second to 3000 RPM and then held at that value for 60 seconds. After the 60 seconds it was ramped down to 0 RPM at the same rate. After the first coating run, the sample was placed into a convection oven and baked at 100° C for five minutes. A second layer was then spun on with the same parameters as the first layer. However, after this coating process, the substrate was placed in a convection oven for 30 minutes.

The next step was to expose a significant amount of the gold-coated diamond nanopillars without exposing any of the bulk. A RIE CS-1701 (March®) plasma cleaner was used to strip the PMMA. This was done using an oxygen plasma with a flow rate of 90 SCCM and an RF power of 50 W. The overall etch time was 6 minutes. Under these conditions approximately 650 nm of the PMMA was remove from the diamond surface. Once the pillars were exposed through the PMMA the gold was etched. The gold was etched using a 1:100 solution of X20:DI water. The overall etch rate of the gold was approximately 10 nm/minute.

This etch rate was used to make the fabrication process more systematic. The sample would be etched in 30 second intervals and then inspected in an optical microscope operated in a dark field imaging mode. As the gold was etched off of the pillars, dark spots would appear and this would be an indication that the pillars had been exposed. The gold was etched from the sample until all of the pillars had been exposed. An SEM image of an exposed diamond nanopillar is shown in Fig. 8.9. The SEM image

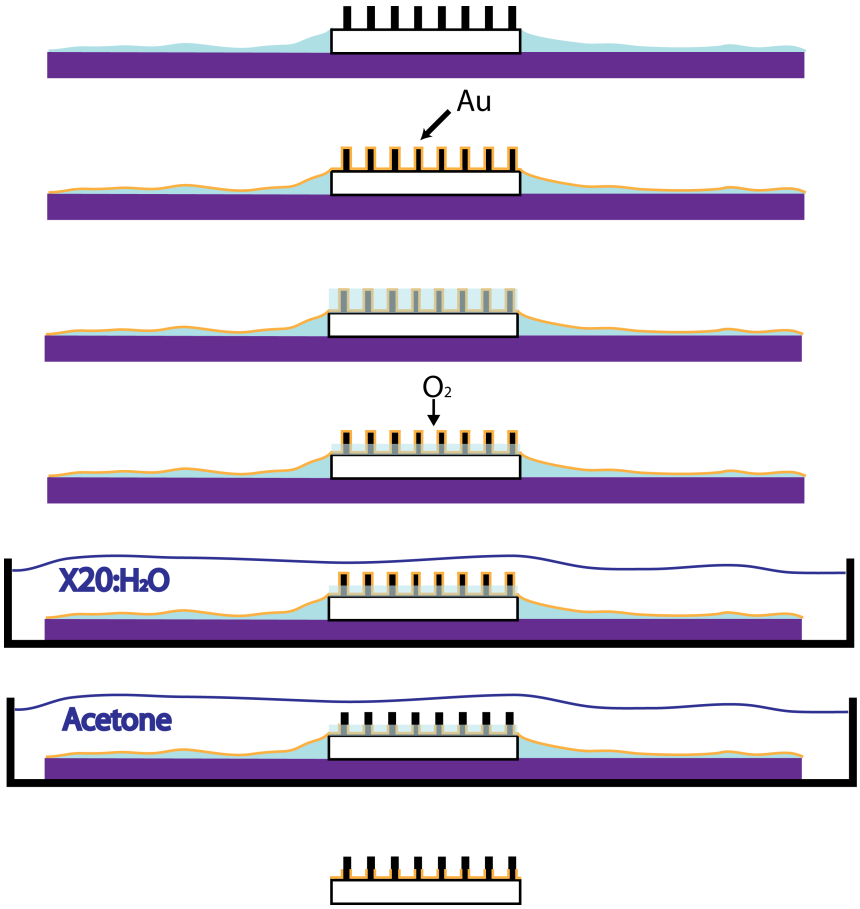


Figure 8.8: A flow chart showing the gold coating process.

is of a 240 nm diameter diamond nanopillar that was exposed through 100 nm layer of gold.

## 8.4. Photoluminescence Characterization of Diamond Nanopillars

In this section, PL data from diamond nanopillars will be presented for both mask fabrication techniques used in this work. However, there is actually no significant difference in the PL or PLE characteristics from either method. What plays a bigger role

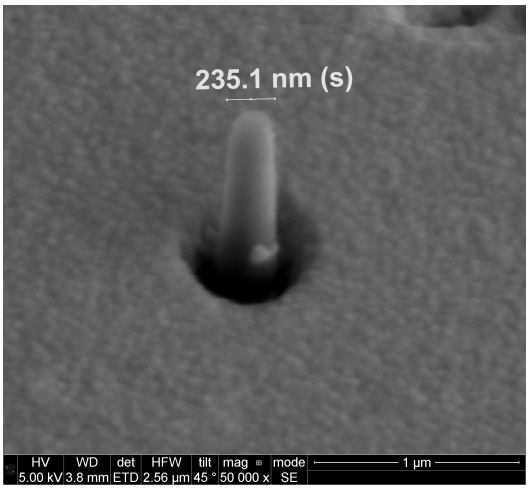


Figure 8.9: An SEM micrograph of a 240 nm pillar exposed through 100 nm of gold.

is the sample from which the nanopillars were fabricated. As was mentioned before, for both the ppm and ppb nitrogen concentration samples the PL at 300K and 10K can vary drastically. For pillars fabricated from the high purity ppb diamond, with a diameter that less than 500nm, it was not possible to detect any negatively charged NV centers. This could be due to the combination of a small volume for these pillar sizes with the low concentration of NV centers sample. For ppm samples it was possible to find NV centers in diamond nanopillars with diameters as small as 140nm.

For pillars that were 500 nm in diameter, and were fabricated from SCD with a ppm nitrogen concentration, it was possible to find a PL signal that stood out of the noise at room temperature. Figure 8.9a shows the room temperature PL obtained from a 500 nm diameter diamond pillar fabricated from a ppm substrate using the metal mask technique. These data were taken with 25 mW of power and the integration time was 1 second. The ZPL can be seen along with the phonon sideband. Figure 6.9b shows the PL

obtained from a 500 nm diameter pillar fabricated from a different ppm sample with the use of a HSQ mask material.

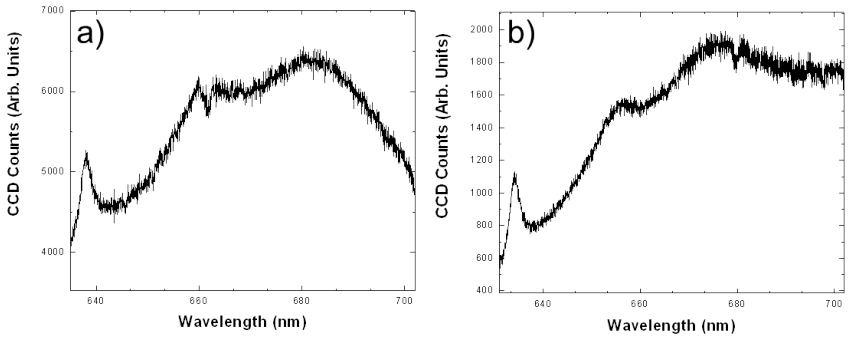


Figure 8.10: Room temperature photoluminescence from a 500 nm pillar fabricated from a diamond sample with a ppm nitrogen concentration using a) the metal mask and b) the HSQ mask technique.

The data for Fig. 8.9b was obtained at room temperature, with a laser excitation power of 50 mW and a 1 second integration time. When comparing these two room temperature plots, there appears to be no significant difference when the pillars are fabricated using an aluminum mask or an HSQ mask. In order to detect PL from nanopillars with diameters less than 500 nm, the samples needed to be cooled to liquid helium temperatures. Figure 8.10 is a series of plots showing the PL obtained at 10K from three different diamond pillars with a diameter of 200 nm. All the pillars were fabricated from the same SCD substrate and were in the same region of the sample. The excitation power for each was 100 mW and the collection time was 30 seconds for the first two plots and 60 seconds for the third.

These three PL spectra display different phenomena observed from 200 nm diameter nanopillars fabricated from SCD with a ppm nitrogen content. One common

theme, however, was that all of the nanopillars from this sample had NV centers whose zero-phonon line had shifted from 637 nm. Sometimes the shift was relatively small as in Fig. 8.10a. However, as is displayed in Fig. 8.10b there were pillars where no signal could be detected from an NV center. In some cases sharp peaks were detected, but could not be identified as originating from NV centers. Figure 8.10c was an intermediate case, where a number of NV centers in a 200 nm pillar had their ZPL emission at or near 637 nm while other NV centers had the ZPL emission shifted by a few nanometers.

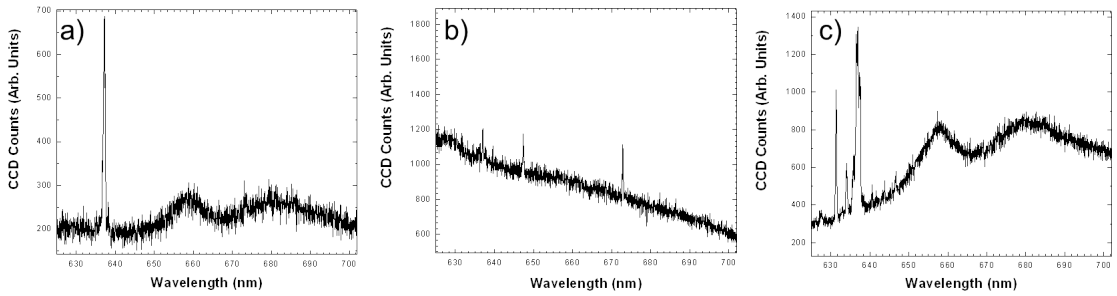


Figure 8.11: Photoluminescence data taken at 10 K from various 200 nm pillars fabricated from a diamond sample with ppm nitrogen content. The metal mask technique was used for these nanopillars.

As the first plot displays, some of the nanopillars had a typical PL spectra from NV centers found in the bulk substrate. This was not very common in sub-500 nm diameter nanopillars studied in samples fabricated from SCD. More commonly one would find that nanopillars had no observable PL. When a nanopillar was found to have strong NV center emission its distribution was similar to that of figure 6.10c. When studying the NV center emission from nanopillars that were fabricated from SCD using an HSQ a mask, the results were similar to that when the mask was aluminum.

Photoluminescence spectra from three different diamond nanopillars are shown in Fig. 8.11. Figure 8.11a was from a 300 nm diameter pillar, which was excited with 50 mW and had an integration time of 60 seconds.

From Fig 8.11a there appeared to be strain-induced shifts in the ZPL emission for some of the NV centers in this particular nanopillar. Figure 8.11b shows the PL spectrum from a 160 nm pillar that was excited with 100 mW and the integration time was 30 seconds. Figure 8.10c shows the PL emission from a 140 nm diamond nanopillar when it was excited with 100 mW of laser power. The data taken for Fig. 8.11 came from nanopillars that were fabricated from two different SCD diamond substrates. However, the data showed the same general characteristic features. The common theme was that when a signal was found it was typically weak and many NV centers seemed to have been moderately strain shifted. It was possible to find nanopillars that were this small where ZPL for some NV centers was shifted by as much as 10 nm. Similar to the case of diamond nanopillars created with an aluminum mask, many pillars with these small of diameters did not show any NV center emission.

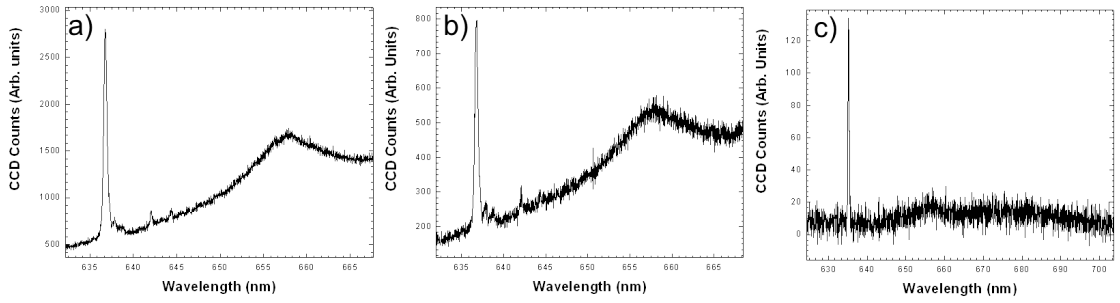


Figure 8.12: Photoluminescence data taken at 10 K from pillars with a) a 300 nm, b) 160 nm and c) 140 nm diameter. These structures were fabricated from a diamond

sample with ppm nitrogen content using the HSQ mask technique.

In the case of samples with ppb nitrogen content, the 500 nm diameter pillars were the smallest feature size that showed signs of PL emission originating from NV centers. Many nanopillars were tested with various diameters and locations as well as on three different samples. Photoluminescence spectra from NV centers in a 500 nm diamond pillar at 10 K showed similar characteristics were no different that the ones taken directly from the bulk samples.

## 8.5. PLE Characterization of NV Centers in Diamond Nanopillars

Finding diamond nanopillars that contained NV centers, which were bright and stable enough to study using the PLE technique, was difficult. It was possible to study a few nanopillars with this technique when they were fabricated from SCD that had a ppm nitrogen concentration. No diamond nanopillars fabricated with ppb nitrogen concentrations showed a PLE signal. Figure 8.13a shows a sequence of PLE scans for a 200 nm diamond nanopillar that was cooled to 10K. Figure 8.13b shows a single trace across the ZPL for this particular NV center. The laser power was 25 nW and the time for each scan was 40 seconds.

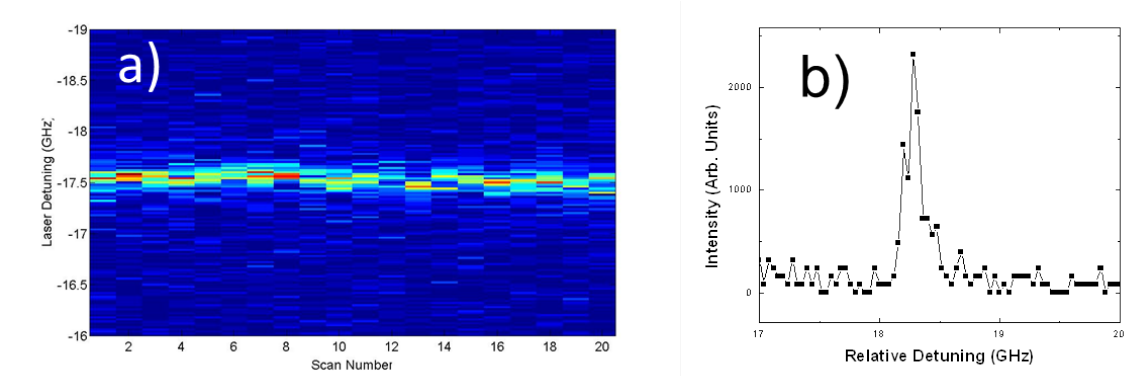


Figure 8.13: a) Stacked PLE scans showing the stability of a NV center found in a ppm 200 nm pillar at 10K. b) A single scan across an NV center showing a linewidth of 120 MHz. These data were taken at 10 K.

In this case the diamond nanopillar was fabricated utilizing the metal mask technique. It was the brightest and most long-lived native NV center found in a diamond nanopillar that was studied in this work; it was an exceptional case. No other PLE sequence of scans lasted this long when studying diamond nanopillars with native NV centers. Also, compared to NV centers typically found in SCD with higher nitrogen concentrations, this particular NV center showed superior stability. It exhibited a linewidth of approximately 80 MHz, which was the typical linewidth for NV centers found in ppm SCD substrates.

A more typical PLE sequence of scans for a NV center in a 200nm diamond nanopillar fabricated from a ppm substrate is shown in Fig. 8.14a. For this sequence of scans the power was 20 nW and the scan period was 10 seconds. The NV center studied in this nanopillar was only studied for 4 scans before it went dark. Also, the NV center was not bright, as can be seen from Fig. 8.14b. It exhibited a linewidth on the order of 60 MHz.

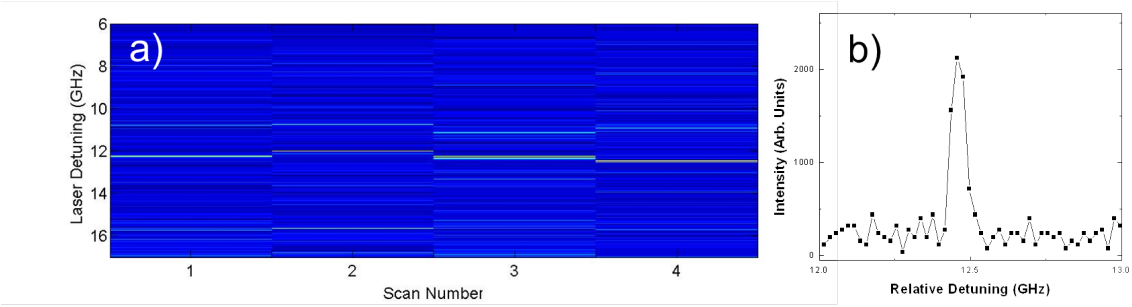


Figure 8.14: a) Stacked PLE scans at 10K showing the stability of a NV center found in a 200 nm pillar fabricated from a ppm sample. b) A single scan across this NV center showing a linewidth of 60 MHz.

Another PLE scan sequence for an NV center in a diamond nanopillar is displayed in Fig. 8.15a. It was found in a 200 nm diameter pillar that was also fabricated from the same diamond substrate as the previous two nanopillars. It was excited with a diode laser with an excitation power of 20 nW. The scan rate for this trace was 0.1 Hz. Relative to the two previous NV centers, this was an intermediate case in terms of its stability and the time it stayed bright. However, the spectral fluctuations that this NV center exhibited were much worse than the first example. The linewidth of this particular NV center was also on the order of 60 MHz.

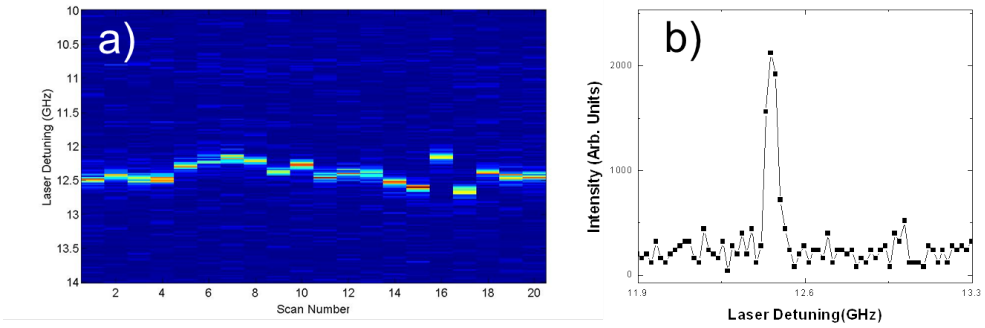


Figure 8.15: a) Stacked PLE scans showing the stability of a NV center found in a 200 nm pillar at 10K. This pillar was on the same substrate as the plots in figure 8.13 and 8.14. b) A single scan across an NV center showing a linewidth of 60 MHz.

Photoluminescence excitation data were not obtained from any diamond nanopillars fabricated from SCD substrates that had a nitrogen concentration that was less than 100 ppb. This could be due to the fact that the density of NV centers was so low in these higher purity diamond substrates. A brief back of the envelope calculation might shed light on the situation. First, for this assumption the typical nitrogen concentration of these high purity samples will be set to 5 ppb. For diamond the number density of carbon atoms is approximately $17.6 \times 10^{22}$ atoms per cubic centimeter, implying the concentration of nitrogen atoms in these samples was approximately $9 \times 10^{14}$ atoms per cubic centimeter. If it is assumed that 0.1% of the nitrogen atoms are in the negatively charged NV state, then the concentration of negatively charged NV centers could be as high as $88 \times 10^{10}$ atoms per cubic centimeter. For a 1 micron tall, 100 nm diameter nanopillar, the number of NV centers per pillar would be roughly 0.03. Assuming that this calculation is valid, if 100 pillars are thoroughly searched one might find three NV centers.

## 8.6. Optical Characterization of Nitrogen Irradiated Diamond Nanopillars

Photoluminescence and photoluminescence excitation experiments were conducted on diamond nanopillars that were fabricated from regions of ppb samples that were irradiated with nitrogen ions. For the data presented in this section, SCD substrate with a nitrogen concentration of approximately 5 ppb were irradiated with 100 keV nitrogen ions. The SCD substrate was irradiated with a dose of $1 \times 10^{-9}$ ions per square centimeter and then annealed at 825° C for 1.5 hours. It was the same sample that was used for the data shown in the Fig. 8.14, 8.16 and 8.17. A photoluminescence spectrum

from a negatively charged NV centers in a 200 nm diamond nanopillar is shown in Fig. 8.17. For this spectrum the sample was cooled to 10 K and the diamond nanopillar was excited with 100 mW of power. An integration time of 30 seconds was used.

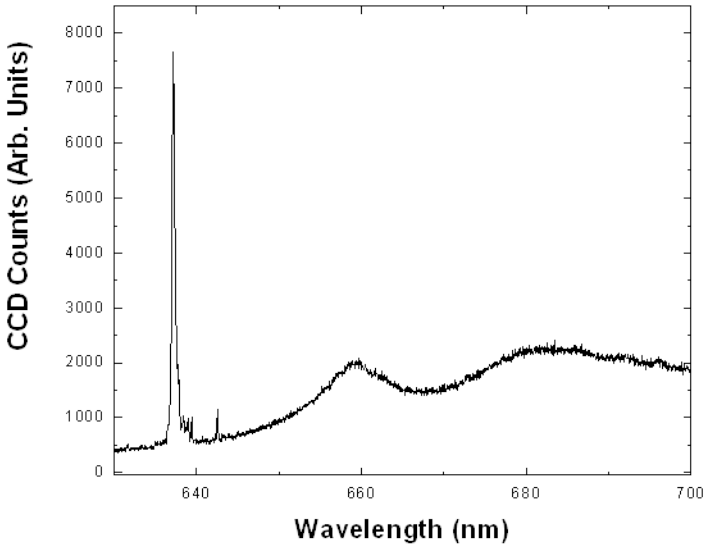


Figure 8.16: Photoluminescence data obtained at 10 K from a 200 nm diamond pillar fabricated from a sample containing 5 ppb nitrogen content which was irradiated with 100 keV nitrogen ions with a fluence of $5x10^{-9}$ ions per square centimeter.

This same nanopillar was then studied using the PLE technique. It was excited with 20 nW of laser power and with a scan speed of 40 seconds. Figure 8.18a shows the data for this sequence of PLE scans. The NV center was only bright for a handful of scans until it went dark. A can be seen from the scan, a large number of counts was detected before the NV center went dark. A single cross-sectional scan across the NV center is shown in Fig. 8.18b. It exhibited a linewidth of approximately 700 MHz. This value for the linewidth was much broader than that of an irradiation induced NV center in the bulk SCD substrate. In that case it was on the order of 200 MHz.

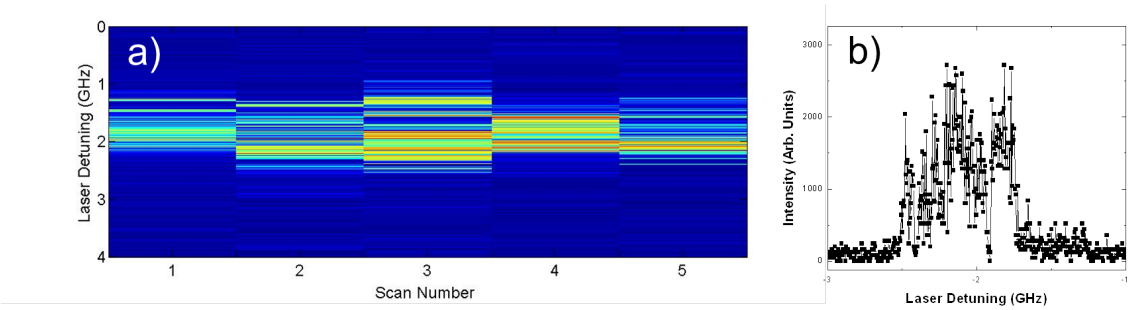


Figure 8.17: a) Stacked PLE scans showing the stability of a irradiation created NV center found in a 200 nm pillar at 10K. b) A single scan across an NV center showing a linewidth of 700 MHz.

This same diamond nanopillar was studied after it was pulsed with a 532 nm laser. The laser pulse lasted for 5 seconds and had a peak power of 100 mW. The frequency of the resonant laser was offset from the previous scan when the next NV center was found in this nanopillar. However, the excitation power of the laser was kept the same. A stacked sequence of PLE scans is shown in Fig. 8.19a, where each scan had a period of 10 seconds. The spectral stability of this NV center was worse than that of the previous NV center, but it could be studied for a much longer time. This could be due to either the re-pumping process or the fact that the total time that the NV center was excited was decreased. This particular NV center exhibited large spectral jumps as well as being spectral unstable. Figure 8.19b shows a single scan spectrum across the NV center. The linewidth was approximately 400 MHz, which is also larger than that found for NV centers studied in regions of ppb diamond substrates that were irradiated and annealed under these same conditions.

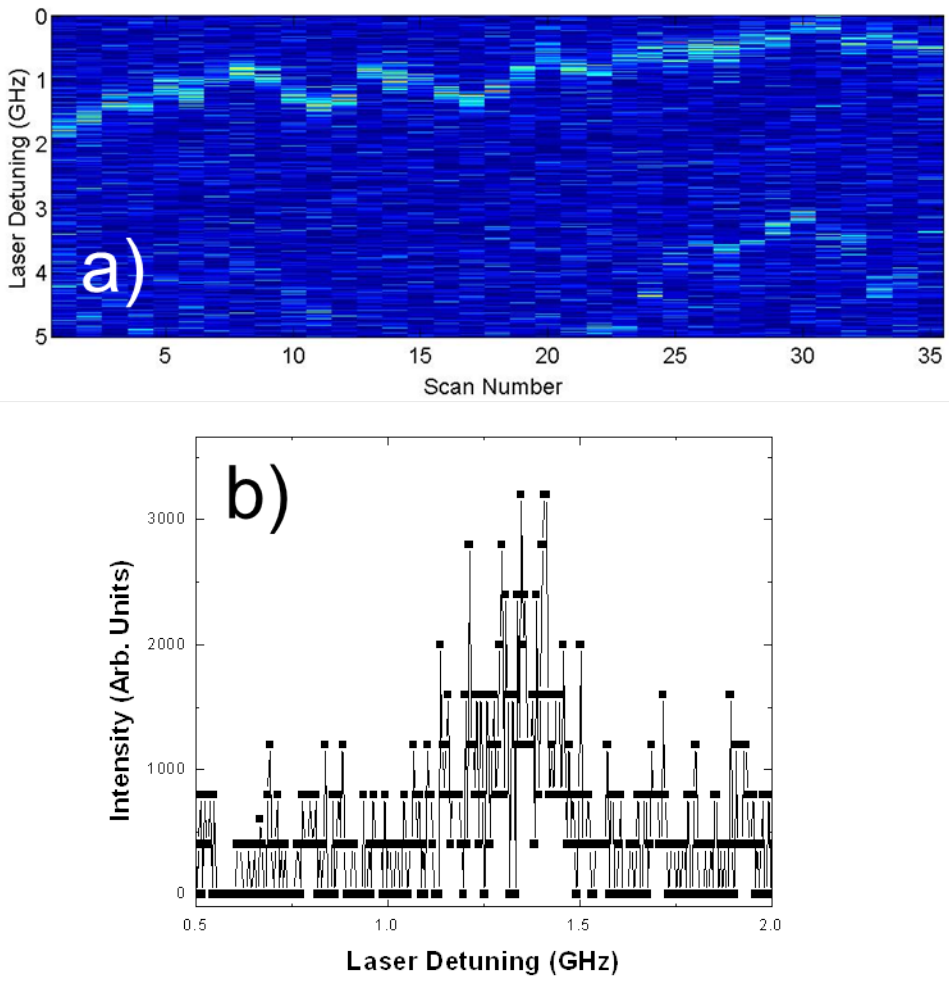


Figure 8.18: a) Stacked PLE scans showing the stability of a NV center found in a 200 nm pillar at 10K. b) A single scan across an NV center showing a linewidth of 400 MHz.

# CHAPTER IX

# A COMPOSITE DIAMOND NANOPILLAR-SILICA MICROSPHERE SYSTEM

This chapter brings together the core components laid out in this dissertation during the development of a cavity quantum electrodynamic (cavity-QED) system, which can ultimately couple a nitrogen vacancy (NV) center in diamond nanopillar to the whispering gallery mode (WGM) supported by a fused silica microsphere. Section 9.1 discusses the room temperature apparatus that was used to position a diamond nanopillar near the surface of a microsphere with nanometer precision. This is the first reported work demonstrating a composite system that filtered the photoluminescence (PL) from NV centers in bulk diamond through a high quality (Q) factor resonator. The section that follows focuses on the low temperature set-up that was used to accomplished this task same task at liquid helium temperatures. Section 9.3 displays the effects that a diamond nanopillar had on the Q of a fundamental WGM. For the room temperature arrangement, a tapered fiber was used to couple the cavity-filtered PL from the NV centers in the diamond nanopillar; these experimental results are detailed in section 9.4. The experimental results of filtering the PL through a deformed microsphere at 10 K will be presented in section 9.5. During the low temperatures PL experiments the WGMs of the cavity were tuned across the zero phonon line (ZPL) for the ensemble of NV centers in the nanopillar.

## 9.1. A Composite Diamond Nanopillar-Silica Microsphere System at Room Temperature

Initially, experiments with the composite diamond nanopillar-fused silica system were conducted at 300 K (room temperature) in order to test the performance of the system. Over the course of these initial studies a procedure was developed to align the diamond nanopillar to the fundamental WGM ($l = m$) of a microsphere. The diamond nanopillars had diameters ranging from 200 nm to 1 micron and were fabricated using the metal mask technique described in the previous chapter. For these experiments, the pillars were fabricated from diamond substrates containing ppm nitrogen concentrations. Furthermore, the pillars were exposed through a gold mask layer in an attempt to limit the PL emitted from NV centers located in the substrate. The details of this gold mask technique were described in the previous chapter as well. Conventional three-dimensional translation stages outfitted with piezo-electric actuators were used for coarse alignment of the diamond nanopillars relative to the sphere surface. These stages allowed for long range positioning, spanning many millimeters, such that various pillars could be tested in the system.

Once a pillar had been brought near the microsphere surface, the piezo-electric actuators enabled the position of the diamond nanopillar to be scanned across a WGM with nanometer precision. At room temperature, the piezo actuators (Thorlabs AE0203D08F) had a displacement of 9 microns when a 150 V DC bias was applied across the ceramic. At room temperature the microsphere was optically coupled to with a tapered fiber that had a 1 micron diameter. The WGMs were excited with a tunable diode laser with an output wavelength near 637 nm. In this experimental set-up, the

tapered fiber was held in place while the microsphere position was adjusted with a three dimensional stage. The tapered fiber was under tension in order to prevent it from inadvertently coming into contact with the microsphere. However, once the microsphere was positioned near the thinnest region of the fiber it was placed in contact with the coupler to simplify the experiment. A schematic of the alignment and excitation set-up is shown in Fig. 9.1.

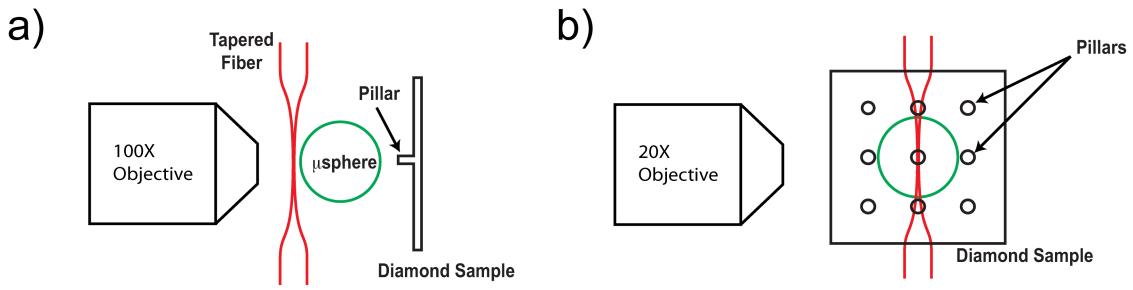


Figure 9.1: A basic schematic of the room temperature set-up used to study the composite system. a) The relative positions perpendicular to the diamond surface were aligned with the aid of a 100X microscope objective. b) The gaps between the diamond and the sphere and the sphere and fiber were monitored with a 20X objective.

Once this initial alignment had been accomplished the rest of the experimental set-up was centered on this location. The gaps between the fiber and the sphere, and the sphere and the diamond, were monitored with the aid of 20X microscope objective (Mitutoyo M Plan APO 20X). This image was focus on to CCD camera with 100 mm focal length plano-convex lens. A second imaging arm was used to monitor the sample surface and to position the nanopillar near the equator of the microsphere. This second imaging arm utilized a 100X microscope objective (Mitutoyo M Plan APO 100X) to

magnify the image and a 100 mm focal length plano-convex lens to focus the image onto another CCD. This imaging arm was perpendicular to the diamond surface.

With the arrangement described above two experiments could be conducted while changing relatively little in the overall set-up. For PL measurements, the sample was excited with a 532 nm laser perpendicular to the sample surface. The laser source was focused onto a diamond nanopillar with the 100X objective through the microsphere as is shown in Fig. 9.2. In this arrangement, the PL emission from NV centers in the diamond pillar, which was filtered through the microsphere, could be directed to a spectrometer by the tapered fiber. Before entering the spectrometer the non-resonant laser source was removed with the appropriate stop-band filter.

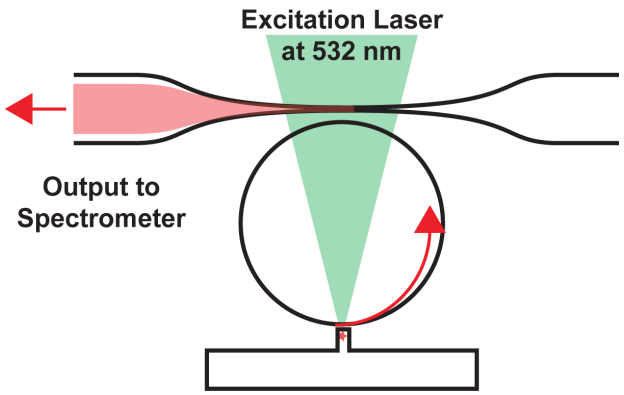


Figure 9.2: Room temperature photoluminescence from nitrogen vacancy centers in a diamond nanopillar could be filtered through a silica microsphere and directed to a spectrometer with a tapered fiber.

By switching the excitation source to the tunable diode laser, WGMs could be excited in the microsphere through the tapered fiber. With this arrangement the Q of the composited system could be measured as a function of the nanopillar position relative to

the sphere surface. The transmission spectrum from the fiber was monitored with lock-in detection as the frequency of the tunable laser was scanned over a fundamental ($l = m$) cavity resonance. With the tapered fiber in contact with the microsphere the system operated in the over-coupled regime. If sphere was not in contact with the tapered fiber their relative position would fluctuate as the nanopillar was scanned across the cavity mode volume. Figure 9.3 illustrates the basic idea behind transmission experiments.

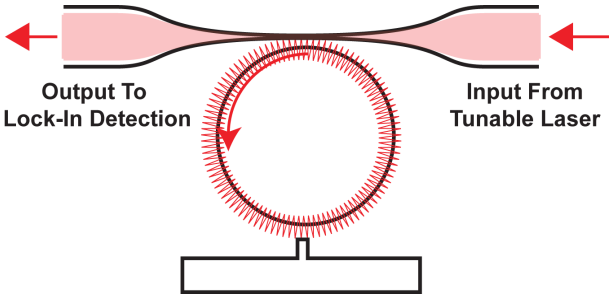


Figure 9.3: The effects from the presence of a diamond nanopillar were studied by monitoring the output of the tapered fiber. The output of tunable diode laser was monitored as the laser was scanned across a fundamental ($l = m$) cavity resonance.

## 9.2. A Low Temperature Composite Diamond Nanopillar-Silica Microsphere System

Low temperature cavity-QED experiments were conducted in an attempt to coherently couple an NV center in a diamond nanopillar to a WGM supported by a fused silica microsphere. Cavity modes were excited and collected from the microsphere with with the free-space coupling technique described in chapter four. With this technique all of the coupling adjustments relative to the sphere could be accomplished outside of the cryostat. In general there were two types of low temperature experiments. Figure 9.4 is a

cartoon for basic PL experiments. During PL measurements, a non-resonant excitation laser (532 nm) was focused onto the surface of the diamond with an excitation arm. This laser was used to directly excite the NV centers in the nanopillar. During these measurements the coupling arm was simply used to collect the cavity filtered PL. The signal from the microsphere was cleaned up with a band-stop filter to remove the non-resonant laser. After passing through the stop-band filter the emission from the cavity was passed through a spatial filter to clean up any scattered light from the sphere or

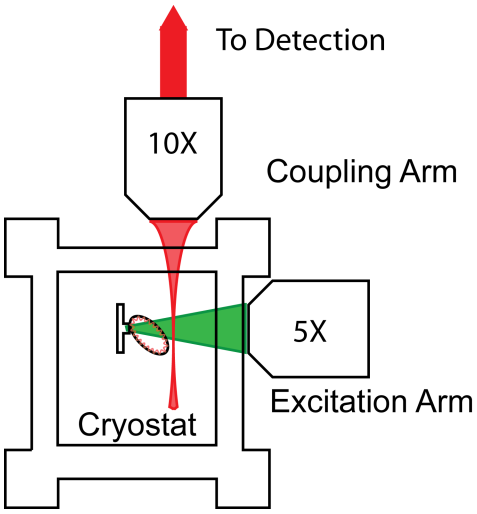


Figure 9.4: The low temperature photoluminescence arrangement.

sample surface. Finally, the cavity emission was coupled to a multimode fiber. The fiber output could then be detected with either a spectrometer or an avalanche photodiode.

The experimental set-ups for the resonant and non-resonant experiments were similar to one another. They both used a coupling and excitation arm as is displayed in the figure above. One major difference between the two experiments was that during the

resonant experiments the cavity was being excited directly with the coupling arm at a frequency $\omega_{cav}$. Also, the excitation arm was used to focus both a resonant and non-resonant laser onto the sample surface through the microsphere. When a non-resonant source was applied to the nanopillar a stop-band filter was used to reject this laser from the coupling arm as before. The scattering from the sphere and diamond surface (from any of the lasers) was removed from the actual cavity emission with a spatial filter. As in the filtered PL set-up, this cavity emission was coupled to a multimode fiber. For resonant excitation experiments the output of the fiber was detected with either a silicon diode (Newfocus 1621) or photomultiplier tube (Hamamatsu R928) whose signals were sent to a lock-in amplifier.

The general concept for the resonant experiments is depicted in Fig. 9.5. In this picture the cavity was being excited with a laser at frequency $\omega_{cav}$ which could be slightly detuned $\Delta_c$ from an optical transition for a NV center within the cavity mode volume. The second laser was focused directly on the diamond nanopillar through the microsphere with detuning $\Delta_{NV}$ from another transition for this same NV center. It should be noted that during these experiments, the actual position of the NV center's resonance frequencies were unknown but the relative detuning between the two lasers could be controlled.

If these two transitions had a common excited state the system is said to be in a lambda configuration. This type of energy level configuration can be useful for many quantum information applications; electromagnetically induced transparency is just one of the many phenomena that can be observed in a lambda system and was describe in

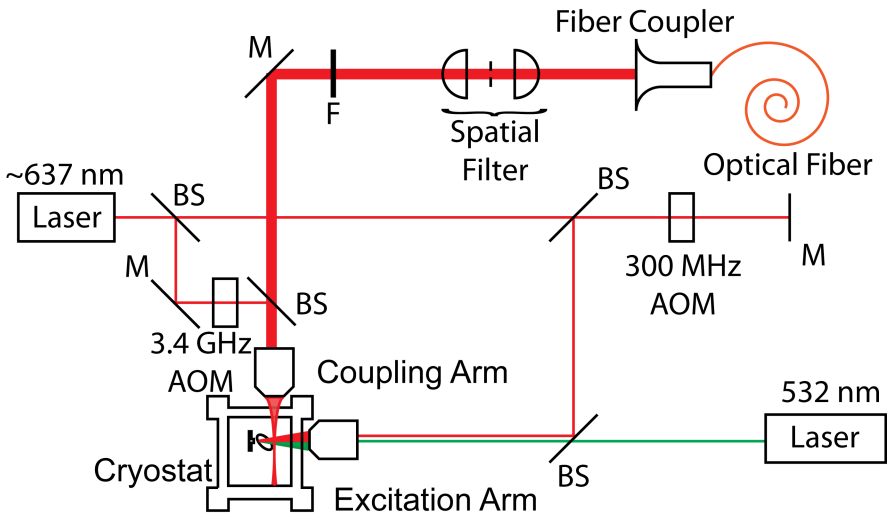


Figure 9.5: One of the many arrangements that was used to resonantly couple a lambda configuration of the nitrogen vacancy to the whispering gallery modes of a deformed double stemmed microsphere. The light collected from the cavity resonance was cleaned up with the appropriate stop band filter (F) and a spatial filter. The light coupled to the fiber could be sent to numerous detection schemes. BS Beam Spliter, M Mirror, AOM Acousto-Optical Modulator.

section 2.2 [213, 214, 215, 216, 217]. In the experiments conducted in this research, the cavity laser was held fixed and the excitation source was scanned $\Delta\omega_{NV}$ and when the system was in Raman resonance with the common excited state the population from one level could then be coherently transferred.

For lock-in detection a double chopped method was used to look for signals that are dependent on both lasers fields. The excitation arm could be thought of as a control laser (section 2.2) while the coupling arm was the probe laser. To prevent spectral instabilities induced by these two resonant lasers, and to keep the NV center from going dark, the powers were kept relatively weak (< 10 μW). In the arrangement shown in Fig. 9.5 the probe laser was detuned from the pump laser by about 2.87 GHz. The first step to

accomplish this was to split the laser source into two beams. One beam was then passed through a 3.4 GHz acousto-optical modulator (Brimrose) while the other was double passed through a 300 MHz acousto-optical modulator (Interaction). With the double pass arrangement that control laser could be scanned by 20 MHz while the lock-in spectrum was being recorded. Non-resonant laser pulses were applied before the resonant data were to be acquired in order to initialize the spin state of the system.

When the silicon diode was utilized the two lasers were modulated with a chopper wheel with a sum frequency near 700 Hz. When the photomultiplier tube was used, the two resonant lasers were modulated at two separate frequencies, ~ 0.7 MHz and ~ 0.45 MHz, and detection required an RF lock-in amplifier to look for signals at the sum frequency of ~ 1.15 MHz. This frequency corresponded to a region where the dye ring-laser had minimal noise. In either case only the photons that originated from the cavity mode were to be detected. As was mentioned in chapter four a spatial filter can be used to remove scattered light from the microsphere. However, when the free space coupling technique was used and a diamond substrate was brought near the sphere surface, the diamond clipped the input laser beam; the diamond surface also reflected the lasers towards the detector. The spatial filter can be used to remove this additional reflected and scattered light. In order to minimize the clipping of the beam the sample was tilted by approximately 5º from the principle axis. This is shown in Fig. 9.6 below.

To operate the composite system at cryogenic temperatures, a positioning system was engineered so that a diamond nanopillar could be scanned near the mode volume of a WGM at 10 K. When loading the composite system into the sample space, and while

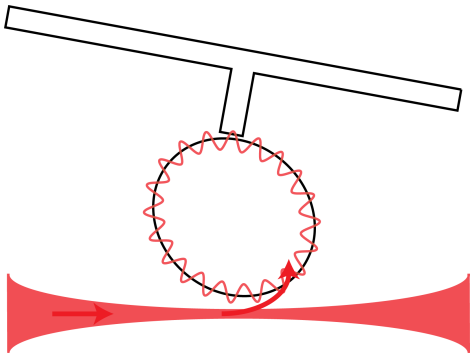

Figure 9.6: The diamond substrate was tilted in order to minimize the clipping of the coupling arm.

cooling down the bath it sits in, the diamond substrate and microsphere were kept millimeters apart. This was done in an attempt to reduce the probability that the Q of the sphere would be irreversible spoiled by coming in contact with the diamond surface. This separation was also necessary to prevent the DDSS from snapping as a result of coming in contact with the sample. Even if the samples and sphere were positioned near one another at room temperature their positions would shift on the order of tens to hundreds of microns due to thermal contraction.

The solution was to integrate commercially available nanopositioners into a compact unit that fit in the sample space that could operate over long distances with nanometer precision in a cryogenic environment. With three of these stages, the nanopillar could be positioned near the surface of a microsphere after the system had been cooled down to 10 K. These stages had a coarse and fine positioning mode of operation. The long travel coarse travel mode of the stages enabled many pillars to be positioned within the cavity mode volume. The high-resolution positioning mode was used to optimize the coupling between the WGM and the nanopillar. This compact unit is shown in Fig. 9.7.

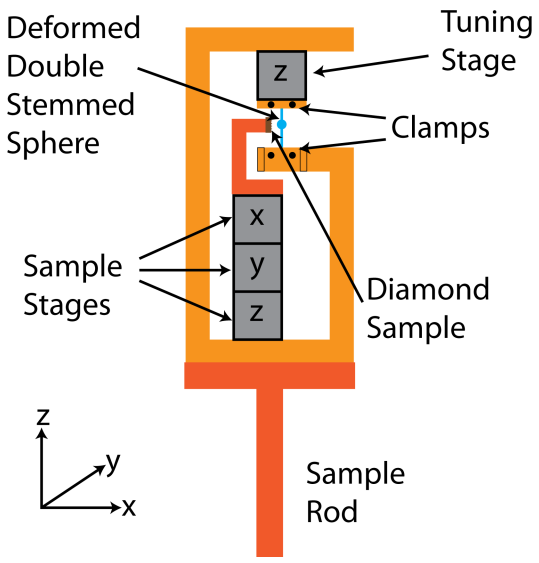


Figure 9.7: A schematic of the composite system. The diamond nanopillar could be positioned with nanometer precision with three nanopositioners at liquid helium temperatures. One end of the sphere was clamped in place while the other end could be stretched with a single nanopositioner.

As can be seen from this figure a fourth nanopositioner was integrated into this system and was used to tune the DDSS. As was mentioned in chapter five, the resonance frequency of a fundamental WMG supported in a DDSS could be shifted over a significant fraction of the microsphere free spectral range, with sub-linewidth resolution, at liquid helium temperatures. This method was used to align the WGM resonance frequency in the DDSS within the zero phonon line for the NV centers found in the nanopillars.

As was mentioned in section 5.3, the resonance of WGMs will shift when the DDSS is cooled from 300 K to 10 K due to thermal contraction and changes in the index of refraction for fused silica. It was experimentally determined that the resonance wavelength of the WGMs supported in the DDSS would blue-shift by about 0.6 nm

during this cool down procedure. With this in mind, the target resonance wavelength for the WGMs was near 637.650 nm at room temperature. For the data in section 9.5, diamond nanopillars fabricated from ppm samples were used in order to have an appreciable number of NV centers near the tip of the diamond nanopillars. The center wavelength for the ensemble ZPL for the NV centers in this class of pillars was typically near 637.1 nm.

On a final note, another consideration was made in order to maintain high-Q WGMs when operating microspheres at 10 K. Due the low thermal conductivity of fused silica, a helium bath cryostat was used to cool the composite system. This class of cryostats uses conduction to cool the samples directly. However, if the sample space has traces of gases other than helium, these other elements will condense onto the microsphere. Any condensation on the surface of the microsphere will result in a degradation of the Q-factor. This issue was resolved by pumping-and-purging the sample space with high purity (99.9999% He) helium gas before the system was to be pre-cooled with liquid nitrogen. While the system was being cooled the sample and reservoir spaces were kept at a positive pressure with this specialty gas.

## 9.3. Quality Factor Spoiling Induced by a Diamond Nanopillar

This section discusses the scattering induced Q-spoiling of WGMs as a result of a nanopillar being positioned within the cavity mode volume. As was mentioned in section 9.1, these data were acquired by measuring the linewidth of a fundamental ($l = m$) WGM resonance as the relative position of the nanopillar was scanned across the region of the

microsphere where the cavity mode was located. Nanopillars with various diameters were used to determine the relationship between the size of the nanopillar and the resulting Q-spoiling. Figure 9.8 shows how the fundamental WGM resonance in a 50 micron diameter microsphere was affected by the bulk diamond substrate. The two plots have been displaced vertically for clarity. The plot in black shows the transmission spectrum for this WGM before the diamond was placed in contact with the sphere surface. After the substrate was brought into contact with the sphere the mode could no longer be observed. This is displayed by the red plot in Fig. 9.8.

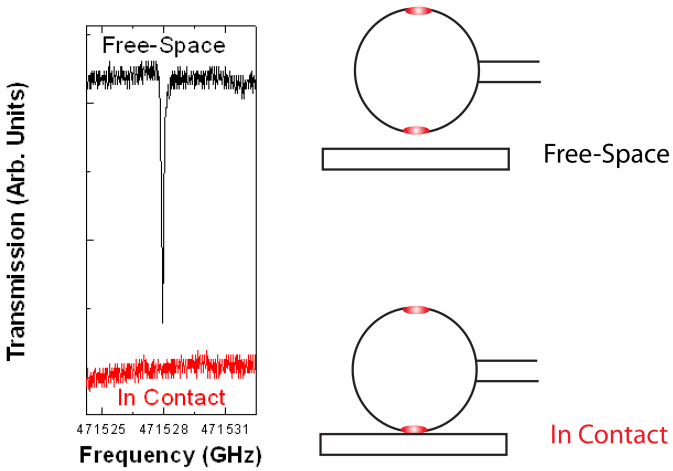


Figure 9.8: The transmission spectrum of a whispering gallery mode for a silica microsphere in the over-coupled regime (black) and when the system is in contact (red) with the bulk diamond substrate for the same resonance.

The scattering induced Q-spoiling due to the presence of the diamond nanopillar was also studied for this WGM. The initial quality factor $Q_0$ of the WGM was limited to $7x10^6$ because the tapered fiber was in contact with the sphere surface, as the system was

being operated in the over-coupled regime. In this geometry the set-up was more stable when scanning the position of the diamond nanopillar relative to the sphere surface. In the data presented in Fig. 9.9 two pillar diameters were used to study the effects of their presence on the cavity Q.

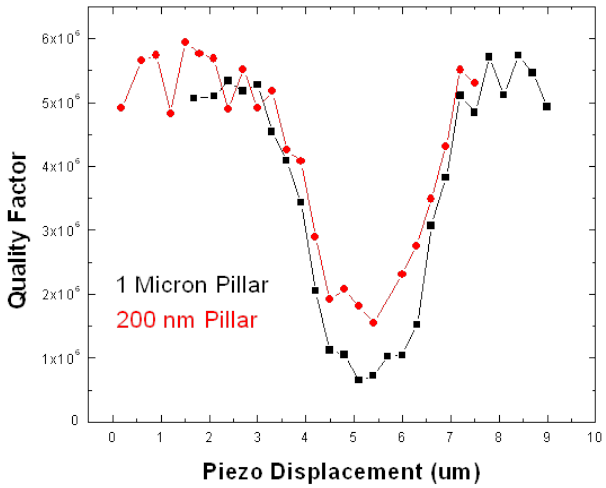


Figure 9.9: Cavity quality factor as a function of position when a 1 micron (black squares) and 200 nm (red circles) diameter pillar was scanned along the azimuthal direction of a 50 micron diameter microsphere.

As can be seen from this figure, when the 1 micron diameter pillar (black squares) was not in the vicinity of the mode volume no effect on the cavity linewidth was observed. There was a clear dip and revival of the Q as the pillar was scanned across the WGM and this indicated that there was only one field intensity maximum along this direction. This helped to confirm that the fundamental mode was indeed being investigated. This measurement was taken before any of the other experiments to insure that the fundamental mode was indeed being monitored. Figure 9.9 also shows the data

when a 200 nm diameter pillar (red circles) was scanned across this same resonance. As can be expected, the smaller diameter nanopillar induced less scattering of the WGM when compared to the 1 micron diameter pillar. When the position of the 200 nm pillar was optimally aligned to the fundamental WGM, the resulting $Q_{tot}$ for the composite system was $2x10^6$. Figure 9.10 displays some of the raw data when a 200 nm pillar was used as the scattering source. This figure displays the fact that the linewidth of the mode was not only broadened but its center frequency was shifted as the mode interacted with the pillar. Once the nanopillar passed through the mode volume the original linewidth and center frequency for the WGM were recovered.

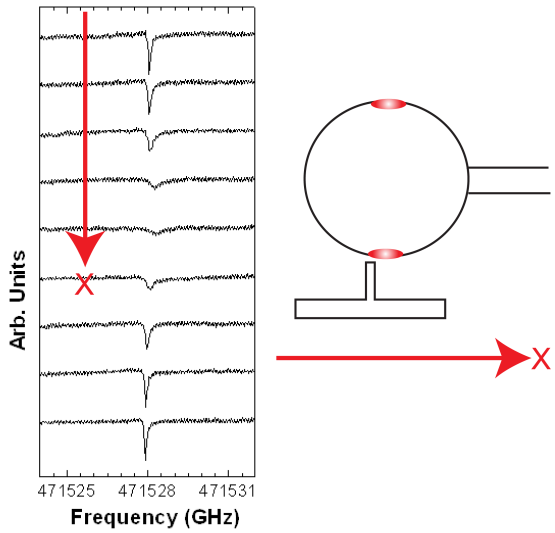


Figure 9.10: Raw data showing the linewidth broadening and frequency shift induced by the presence of a 200 nm diameter nanopillar.

From the shape of Fig. 9.9, the pillar was indeed interacting with the fundamental ($l = m$) WGM allowing a theoretical model based on a Weisskopf-Wigner formalism to

estimate the diameter of a diamond nanopillar so that the cavity decay rate κ for the composite system remain below the theoretical maximum cavity coupling rate *g*; this coupling rate was estimated to be approximately 50 MHz in chapter 2 [218]. For a sphere with a 50 micron diameter, and with the wavelength of light at 635 nm, the polar angular extent of this mode can be shown to be on the order of 4˚, in good agreement with the spatial extent of the Q-spoiling shown in Fig. 9.9 [219].

The total cavity decay rate κ of the composite nanopillar-microsphere system can be thought of as a combination of the over-coupled bare sphere $\kappa_0$ plus a scattering induced decay rate $\kappa_{np}$ due to the presence of the pillar:

$$\kappa = \kappa_0 + \kappa_{np} \tag{9.1}$$

When a nanopillar with a 200 nm diameter was used to induce the Q spoiling $\kappa/2\pi$ was approximately 120 MHz for the composite system and $\kappa_0/2\pi$ was approximately 40 MHz. Using (9.1) gives a value for $\kappa_{np}/2\pi$ of 80 MHz. In the Weisskopf- Wigner formalism, the pillar scatters the evanescent field elastically with a scattering rate given by:

$$\kappa_{sc} = \frac{\alpha^2 f(\mathbf{r})\omega_c^4}{6\pi c^3 V_c}, \tag{9.2}$$

where $\omega_c$ is the angular frequency, c is the speed of light, $V_c$ is the cavity mode volume, $f(\mathbf{r})$ describes the spatial variation of the electric field in the cavity mode, which is assumed to be unaffected by the pillar. The pillar is also assumed to be a spherical sub-wavelength scatterer, where the polarizability α of the scatter is given by:

$$\alpha = 4\pi r_{sc}^3 \left| \frac{\varepsilon - 1}{\varepsilon + 2} \right|. \tag{9.4}$$

In (9.4) $r_{sc}$ is the radius and ε is the dielectric constant of the scatterer, respectively. With $\lambda = 635$ nm, $r_{sc} = 100$ nm, $\varepsilon = 5.68$, $V_c = 310$ cubic microns, $\kappa_{sc}/2\pi = 80$ MHz and with $f(\mathbf{r})$ as an adjustable parameter, (9.4) results in a value of 0.2 for $f(\mathbf{r})$. Since the evanescent field decays rapidly away from the sphere surface, the value of f(r) obtained is considerably smaller than the field amplitude at the sphere surface relative or to the maximum field strength inside of the microsphere.

The polarizability, and hence $\kappa_{sc}$, scales strongly with the pillar radius as can be seen from the $r_{sc}^6$ power law in (9.2). Reducing the pillar diameter can significantly decrease the scattering induced decay rate for the composite system. For strong coupling cavity-QED, it is desirable that κ be comparable to the decoherence rate $\gamma/2\pi$ for the relevant optical transition. In the ideal case, an NV center can have a value of $\gamma_{NV}/2\pi$ on the order of 10 MHz. Assuming that the $r_{sc}^6$ power dependence for $\kappa_{sc}$ holds in (9.2), a value for $\kappa/2\pi$ on the order of 10 MHz can be achieved by shrinking the nanopillar diameter to 140 nm. Nanopillars of this size were fabricated and the experimental results displaying the Q spoiling induced by this size pillar are displayed below. However, it should be noted that the $r_{sc}^6$ dependence is no longer valid when the scatter size approaches optical wavelength. Therefor, this analysis cannot be applied to the 1 micron diameter pillar.

As was discussed in chapter eight, samples with 140 nm diameter nanopillars were fabricated from single crystal diamond. This was done after these initial

measurements and calculations were conducted. At that point in this research, the free space excitation technique had replaced the fiber coupling technique. Sets of measurements similar to those described above were conducted by scanning a 140 nm diameter pillar across the fundamental mode ($l = m$) of a deformed microsphere with a diameter of 50 microns. Figure 9.11 shows a plot similar to Fig. 9.9, and displays the linewidth as a function of the pillars position. The diamond pillar was in contact with the surface of the sphere during these experiments and the low temperature apparatus was used to acquire this data. The initial linewidth of the sphere was approximately 50 MHz and at the point of maximum Q spoiling the linewidth was on the order of 80 MHz. The corresponding Q at these values, when the wavelength of the cavity mode was near 637 nm, is $9 \times 10^6$ and $6 \times 10^6$, respectively.

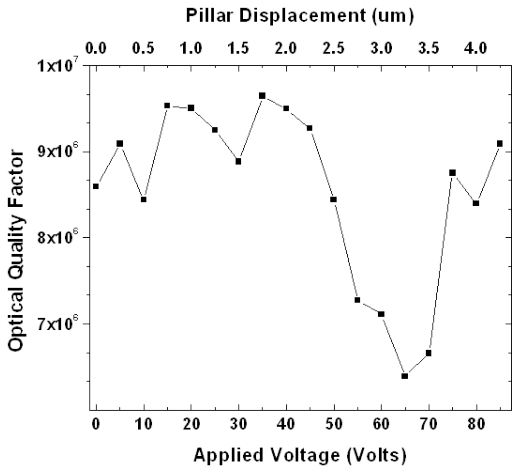


Figure 9.11: Quality factor for a composite system as a function of the relative position between a 50 micron diameter microsphere and a 140 nm diameter nanopillar. The nanopillar was scanned across the optical equator of a fundamental ($l = m$) whispering gallery mode.

Using the above analysis, the value for the cavity enhanced decay rate for a 140 nm diameter nanopillar would have a value for the induced decay rate of 20 MHz ($\kappa_{sc}/2\pi$). This value was calculated using the parameters mentioned above and is on the order of what was observed. The adjustable parameter $f(\mathbf{r})$ could be scaled to 0.26 in order to better fit the above data and match the observed value of $\kappa_{sc}/2\pi$ of 30 MHz. This would be reasonable considering that a deformed microsphere has an enhanced evanescent field decay length. There might be a slight deviation from the $r_{sc}^{6}$ dependence on the scattering induced broadening for a deformed microsphere.

## 9.4. Photoluminescence Spectra from the Composite System at 300 K

This section presents the PL data obtained at room temperature with the composite system describe in section 9.1. A 1 micron diameter tapered fiber was used to optically couple to the 50 micron diameter microsphere. The cavity operated in the over-coupled regime with a maximum $Q_{tot}$ of $6x10^6$. Diamond nanopillars of various diameters, as well as the bulk diamond substrate, were brought into contact with the sphere surface in order to observe their impact on the system's Q. However, once these nanopillars were optimally positioned within the evanescent field of the WGM, a 532 nm laser could be focused onto the pillars to excite NV centers in the sample.

When the bulk diamond substrate was placed in contact with the microsphere the lowest order azimuthal mode vanished in the transmission experiment but higher ($l \neq m$) order modes were still visible. This was due to the fact that the mode volume of these higher order WGMs did not completely interact with the entire diamond substrate.

Figure 9.12 shows the PL that was filtered through the microsphere when it was in contact with the bulk (in black) diamond substrate. Overlaid on this plot is the PL obtained directly from this same diamond sample with the confocal microscope arrangement mentioned in section 6.3. The two plots were taken with the same laser power (10 mW) and integration time (10 seconds). As can be seen from this figure, WGM structure was imprinted on the PL spectrum when it was filtered through the cavity.

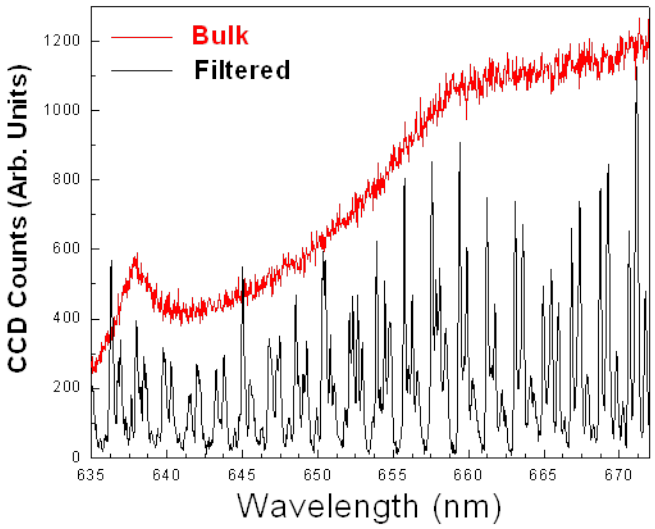


Figure 9.12: Photoluminescence obtained directly from the bulk (red) and photoluminescence from the bulk but filtered (black) through the sphere. These data were taken at room temperature.

This structure can be thought of as an envelope imprinted on the PL spectrum of the NV centers. Only the envelope for the family of cavity modes (same *l* value) could be observed because the individual WGMs were too sharp to resolve with the

spectrometer. There appeared to be two pairs of peaks that were higher in intensity followed by a third weaker peak. The first two are thought to come from the TE and TM modes for the $n$ =1 modes, while the third hump is a result of higher order radial modes. These higher order radial modes would couple more weakly to the samples. Figure 9.13 shows the filtered PL from NV centers in a 200 nm diameter nanopillar after it had been positioned at a point on the microsphere where the maximum Q-spoiling occurred.

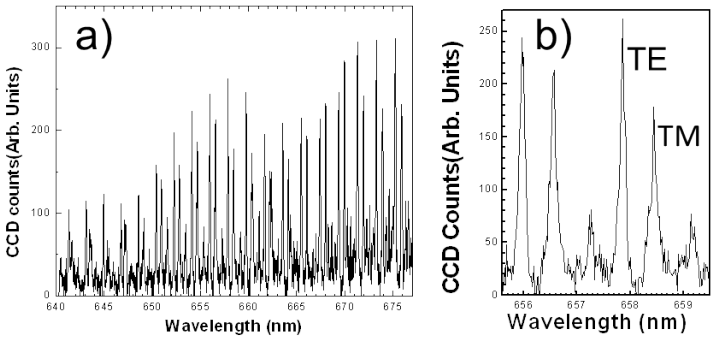


Figure 9.13: a) Photoluminescence filtered through a microsphere. b) A close-up of the data in a). The two peaks are a result of an offset for transverse electric and transverse magnetic modes. The pillar was 200 nm in diameter. These data were taken at room temperature.

This spectrum was acquired with a laser power of 100 mW and an integration time of 10 seconds. From this plot the WGM structure can be seen more clearly. The gold mask technique described in the previous chapter was used to suppress PL from that didn't originate from the nanopillar. The peak associated with the higher order radial modes was more noticeable as well. When the diamond nanopillar was positioned at a location where there was no observed Q-spoiling very little PL signal was detected on the spectrometer and no signatures of WGMs were noticed. Also, PL could not be observed

when the pillar was optimally aligned to the WGM, but the non-resonant excitation source was misaligned relative to the nanopillar position. The splitting of 1.3 nm for the TE–TM modes is in agreement with the theoretical expectation for a silica microsphere with a diameter of 50 microns and at a wavelength near 637nm [113].

## 9.5. Photoluminescence Spectra from the Composite System at 10 K

After the low temperature composite system had reached thermal equilibrium at 10 K, PL experiments were conducted similar to those in the previous section. For the data presented in this section, nanopillars fabricated from ppm nitrogen concentration substrates were used for filtered PL experiments. In these cryogenic temperature experiments, the PL from NV centers in diamond nanopillars were filtered through the WGMs of a deformed silica microsphere. Various sized pillars were used, however, there was very little difference in the spectra due to an increased background signal that did not originate from the cavity modes directly. The tapered fiber coupling in the room temperature set-up could better filter the signal spatially when compared to the spatial filter used for free-space coupling.

Figure 9.14 shows the filtered PL spectrum from a deformed microsphere when a 160 nm diameter nanopillar was optimized to the fundamental WGM of the microresonator. With a decreased signal-to-noise ratio it was more difficult to distinguish the TE and TM modes. The data in Fig. 9.14 was taken at 12 K with an excitation power of 100 mW. The integration time of the spectrometer was set to one second. The WGMs of the DDSS was tuned across the inhomogenously broadened ZPL

for the ensemble of NV centers in the nanopillar. For any of the tuning methods the step size was too fine to resolve with the spectrometer. The typical size for the step tuning method was on the order of a picometer, and the highest resolution of the spectrometer was 0.01 nm.

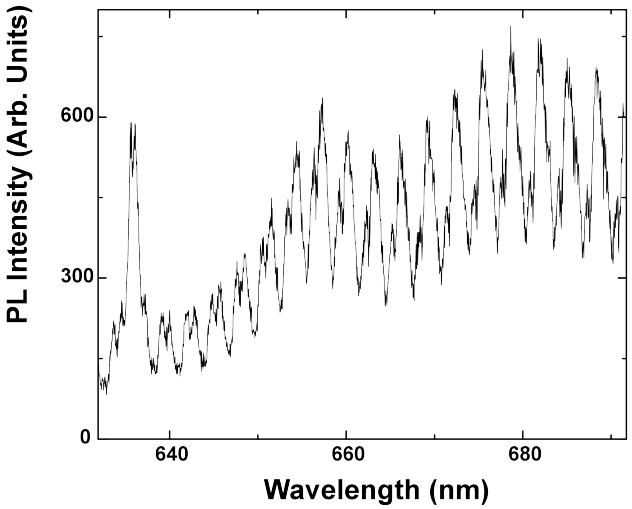


Figure 9.14: Photoluminescence from nitrogen vacancy centers in a diamond nanopillar filtered through a the whispering gallery modes of a deformed double-stemmed microsphere at 10 K

Figure 9.15a and 9.15b shows the filtered PL before and after 25 coarse tuning steps were applied to the DDSS, respectively. For the data in Fig. 9.15, a 5 micron diameter pillar was used for simple alignment between the pillar and the fundamental WGM. For these two scans, the laser power was 100 mW and the integration time for the spectrometer was one second. Before each acquisition with the spectrometer, the optical coupling to the microsphere was re-optimized.

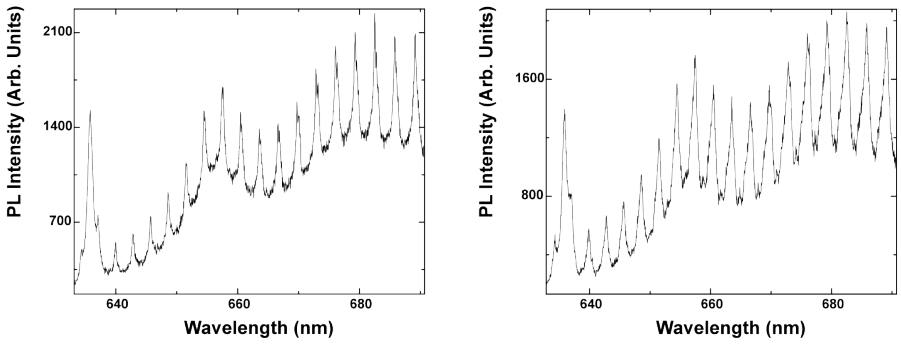


Figure 9.15: Photoluminescence spectra a) before and b) after 25 applications of the step tuning were made to the deformed double-stemmed microsphere. Each 25 V step corresponded to 30 GHz. These data were acquired at 10 K.

As the family of WGMs (same value of *l*) was tuned across the ZPL an increase in the PL emission from the ZPL was observed. Again, after each of the 25 steps the signal coupling to the microsphere was optimized for the best signal-to-noise ratio. Also, once the sphere was under tension the relative position between the microsphere and a five micron diameter pillar was unaffected by this amount of tuning. Figure 9.16 shows a contour plot that is built up from consecutive spectrometer scans. The number of counts at the peak of the ZPL decreased from approximately 2,300 counts per second to 1,000 counts per second from the first scan to the last scan shown in Fig. 9.16, respectively. In this particular case, the WGM mode frequency was shifted away from the ZPL. The data in this plot was taken at 10K with 100 mW of power used to excite the pillar and with an integration time of 5 seconds.

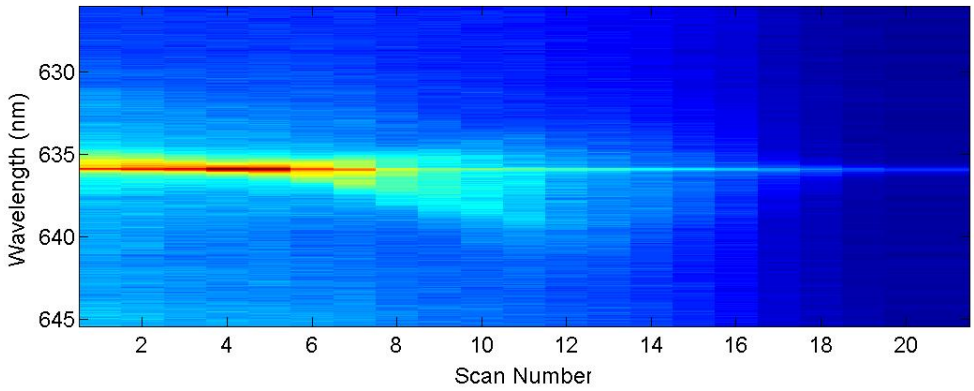


Figure 9.16: Consecutive photoluminescence spectra from the composite system at 10K. The whispering gallery modes in a deformed double-stemmed microsphere were tuned away from the zero phonon line by 30 GHz between scans.

During the course of this dissertation work there were no observations of coherent coupling between an NV center and a WGM. Many experimental approaches were taken to accomplish this, however, a signature coherent coupling was not observed. In the set-up described in section 9.2 for the two beam resonant excitation scheme, the overall sensitivity of the detection was one part in a million when the photomultiplier tube was used with the RF-lockin.

There are many reasons why this might be the case. First off, samples with ppm nitrogen concentrations were used because there was no observed PL from pillars fabricated from ppb substrates. However, as was shown in chapter seven, NV centers in this class of samples were spectrally unstable and were prone photodarkening. Second, there was the possibility that there were too few NV centers that were within the top 100 nm of the pillar. If this were the case, the chances of optimizing the resonant lasers with just these few NV centers is low making this approach time consuming and difficult.

However discouraging this may sound, the techniques and approaches developed in this research are necessary for the eventual development of a composite system that can coherently couple a single NV center in a diamond nanopillar a high-Q WGM in a deformed microsphere. The following chapter outlines the next steps for reaching these goals in future work.

# CHAPTER X

# CONCLUSION AND OUTLOOK

In this dissertation, a composite diamond nanopillar-fused silica microsphere system that could operate at liquid helium temperatures was developed. This research began with only a concept but over time it resulted in numerous technological advances that are necessary to coherently couple a nitrogen vacancy (NV) center in a nanopillar to the whispering gallery mode (WGM) supported by a microsphere. As the case would be for any cavity quantum electrodynamic (cavity-QED) system, overcoming technical and experimental challenges were a major part of the work. For a cavity-QED system to operate in the strong coupling regime, the cavity-coupling rate needs to be larger than the cavity or atomic decay rates.

Diamond nanopillars with various diameters were fabricated from single crystal diamond substrates. When a 140 nm diameter diamond nanopillar was positioned within the evanescent field of a fundamental ($l = m$) WGM the linewidth of the composite system was 80 MHz. If a gap is maintained between the nanopillar and the sphere surface Qs approaching 10 MHz are possible; maintaining a gap involves more technical difficulties and could reduce the cavity coupling rate. A composite system was engineered which enabled the nanopillar to be positioned with nanometer precision within the mode volume of 30 micron diameter microspheres at 10 K. With diamond nanopillars fabricated from ppm samples the PL emission from NV centers was filtered

through the WGMs of fused silica microspheres at 10 K. A fabrication technique was developed to coat the surface of the substrate with gold such that only the nanopillars were exposed. This insured that the signal detected originated from NV centers in the bulk.

Different classes of samples were used to fabricate pillars. These samples had either parts per million (ppm) or parts per billion (ppb) nitrogen concentrations. Nitrogen vacancy centers in bulk diamond and in diamond nanopillars were optically characterized using photoluminescence (PL) and photoluminescence excitation (PLE) techniques to determine their suitability for cavity-QED studies. As was shown in chapter six that the spectral stability and linewidth for NV centers in ppb SCD substrates were superior to color centers in ppm samples. For nanopillars fabricated from ppm diamond, PL and PLE was detected from pillars with diameters as small as 160 nm. Unfortunately nitrogen vacancy centers in these samples showed features of spectral instability and had broad linewidths. In ppb samples on the other hand, PL and PLE could not be observed from pillars with diameters smaller than 500 nm.

As was mention above, by introducing a gap between the microsphere surface and the diamond nanopillar the scattering induced broadening can be reduced. However, this would also reduce the cavity-coupling rate. In an attempt resolve these two issues nitrogen ions were implanted in high purity diamond to induce NV centers near the surface of the sample, which could then be used to fabricated diamond nanopillars. Photoluminescence and PLE signals could be detected from 200 nm diameter diamond nanopillars that were fabricated from regions of ppb diamond substrates that were irradiated nitrogen ions. Ultimately, it was determined that NV centers that were studied

in these types of samples showed spectral instabilities that were greater than those in ppm samples. Also, the linewidth for NV centers in these irradiated regions were larger than a gigahertz.

With this information another approach was developed to increase the interaction strength between the cavity modes and NV centers in the diamond nanopillars. The evanescent field decay length of deformed microsphere were investigated and it was observed that the decay length at specific regions was up to four times longer than those of a non-deformed microresonator. This enhanced evanescent decay length allows for the coupling of WGMs to NV centers deeper into the diamond substrate, or to increase the coupling rate to NV centers closer to the surface. Deformed microspheres, with their enhanced cavity decay length, can also be used with cold atoms or quantum dots in micro-pillars to enhance the coupling rate in these systems.

Another unique feature of the low temperature composite system developed in this research project was the solution for one of the shortcoming of fused silica microspheres. When fabricating a microsphere it is not possible to control the resonance frequency. For cavity-QED studies, it is crucial to overlap the cavity resonance with the emitter dipole transition frequency. To resolve this issue at liquid helium temperatures, the composite system utilized a deformed doubled-stemmed microsphere (DDSS) as the resonator. With this resonator integrated into the system, the WGM resonance frequency of the cavity could be tuned over 450 GHz with sub-10 MHz resolution. This was accomplished with sub-picometer changes in the sphere diameter at 10 K. The DDSS tuning capabilities can also be applied to other applications such as trace gas detection,

locking a microsphere to a laser as well as biological and chemical applications including those for protein detection [220, 221, 222].

The fact that resonant coupling between an NV center and a WGM was not observed begs the question, "Why?" The most obvious answer is that there were no NV centers within the evanescent field of the cavity. This could be due to the fact that the pillars have small volumes and within that region relatively few NV centers might be within the top 100 nanometers of the structure. Furthermore, due to mechanical polishing techniques, there could be a damaged layer of diamond that would need to be processed with microfabrication equipment. It is possible to remove this damaged layer and bring more pristine diamond to the surface. Other material growth or modification approaches could be taken to create NV centers within 50 nm from the tip of the diamond, which exhibit optical properties comparable to the ones observed in ppb bulk samples. This approach, either during the growth process or post growth by irradiating the samples with high-energy particles, is beyond the scope of this research and the capabilities of the Wang Lab. As was mentioned in chapter six, this area of research is of relevance for numerous applications, from cavity-QED to quantum metrology.

As the quality of the samples improve, the key ingredients of this dissertation research will be indispensible for cavity-QED research between NV centers and WGM silica resonators. Silica microresonators are the only class of microresonator with linewidths narrow enough for strong coupling with NV centers. Once a material growth technique has been developed to fabricate substrates with high quality NV centers near their surface, diamond nanopillars fabricated from those types of samples can incorporated into this composite system. With NV centers in the top 50 nm or so of the

nanopillar, introducing a gap between the pillar and the microsphere surface can increase the quality factor of the composite system. In this arrangement, Qs as high as $10^8$ are possible. Even if the strong coupling regime is not obtained numerous cavity mediated nonlinear experiments can be conducted; some of which are described in chapters one and two. The tools and techniques developed over the course of this research help to combine and harness quantum control of individual photons, electron spins, and nuclear spins in a cavity QED system that couples negatively charged nitrogen vacancy (NV) centers in diamond to an optical microresonator. These advances help in the development of a solid-state light-matter quantum interface that can reversibly map quantum states between light and a well-isolated nuclear spin.

REFERENCES CITED


1. Planck, M., *The Theory of Heat Radiation*, Philadelphia, (1914)

2. Dirac, P.a.M., *The Quantum Theory of Dispersion*. Proceedings of the Royal Society of London. Series A, **114**(769): p. 710-728. (1927).

3. Dirac, P.a.M., *The Quantum Theory of the Emission and Absorption of Radiation*. Proceedings of the Royal Society of London. Series A, **114**(767): p. 243-265. (1927).

4. Lamb, W.E. and Retherford, R.C., *Fine Structure of the Hydrogen Atom by a Microwave Method*. Physical Review, **72**(3): p. 241-243. (1947).

5. Casimir, H.B.G. and Polder, D., *The Influence of Retardation on the London-van der Waals Forces*. Physical Review, **73**(4): p. 360-372. (1948).

6. Chow, W.W., Scully, M.O., and Stoner, J.O., *Quantum-Beat Phenomena Described by Quantum Electrodynamics and Neoclassical Theory*. Physical Review A, **11**(4): p. 1380-1388. (1975).

7. Herman, R.M., Grotch, H., Kornblith, R., and Eberly, J.H., *Quantum Electrodynamic and Semiclassical Interference Effects in Spontaneous Radiation*. Physical Review A, **11**(4): p. 1389-1396. (1975).

8. Weisskopf, V. and Wigner, E., *Berechnung der Natürlichen Linienbreite auf Grund der Diracschen Lichttheorie*. Zeitschrift für Physik A Hadrons and Nuclei, **63**(1): p. 54-73. (1930).

9. Brown, R.H. and Twiss, R.Q., *A Test of a New Type of Stellar Interferometer on Sirius*. Nature, **178**(4541): p. 1046-1048. (1956).

10. Brown, R.H. and Twiss, R.Q., *Interferometry of the Intensity Fluctuations in Light II. An Experimental Test of the Theory for Partially Coherent Light*. Proceedings of the Royal Society of London. Series A. Mathematical and Physical Sciences, **243**(1234): p. 291-319. (1958).

11. Arecchi, F.T., *Measurement of the Statistical Distribution of Gaussian and Laser Sources*. Physical Review Letters, **15**(24): p. 912-916. (1965).

12. Arecchi, F.T., Gatti, E., and Sona, A., *Time distribution of photons from coherent and Gaussian sources*. Physics Letters, **20**(1): p. 27-29. (1966).

13. Morgan, B.L. and Mandel, L., *Measurement of Photon Bunching in a Thermal Light Beam*. Physical Review Letters, **16**(22): p. 1012-1015. (1966).

14. Drexhage, K.H., *IV Interaction of Light with Monomolecular Dye Layers*, in *Progress in Optics*, E. Wolf, Editor 1974, Elsevier. p. 163-232.

15. Goy, P., Raimond, J.M., Gross, M., and Haroche, S., *Observation of Cavity-Enhanced Single-Atom Spontaneous Emission*. Physical Review Letters, **50**(24): p. 1903-1906. (1983).

16. Hulet, R.G., Hilfer, E.S., and Kleppner, D., *Inhibited Spontaneous Emission by a Rydberg Atom*. Physical Review Letters, **55**(20): p. 2137-2140. (1985).

17. Martini, F.D., Innocenti, G., Jacobovitz, G.R., and Mataloni, P., *Anomalous Spontaneous Emission Time in a Microscopic Optical Cavity*. Physical Review Letters, **59**(26): p. 2955-2958. (1987).

18. Hinds, E.A., *Cavity Quantum Electrod Ynamics*, in *Advances In Atomic, Molecular, and Optical Physics*, B. David and B. Benjamin, Editors. 1990, Academic Press. p. 237-289.

19. Meschede, D., *Radiating Atoms in Confined Space: From Spontaneous Emission to Micromasers*. Physics Reports, **211**(5): p. 201-250. (1992).

20. Thompson, R.J., Rempe, G., and Kimble, H.J., *Observation of Normal-Mode Splitting for an Atom in an Optical Cavity*. Physical Review Letters, **68**(8): p. 1132-1135. (1992).

21. Turchette, Q.A., Hood, C.J., Lange, W., Mabuchi, H., and Kimble, H.J., *Measurement of Conditional Phase Shifts for Quantum Logic*. Physical Review Letters, **75**(25): p. 4710-4713. (1995).

22. Nogues, G., Rauschenbeutel, A., Osnaghi, S., Brune, M., Raimond, J.M., and Haroche, S., *Seeing a Single Photon Without Destroying It*. Nature, **400**(6741): p. 239-242. (1999).

23. An, K., Childs, J.J., Dasari, R.R., and Feld, M.S., *Microlaser: A laser with One Atom in an Optical Resonator*. Physical Review Letters, **73**(25): p. 3375-3378. (1994).

24. Hood, C.J., Lynn, T.W., Doherty, A.C., Parkins, A.S., and Kimble, H.J., *The Atom-Cavity Microscope: Single Atoms Bound in Orbit by Single Photons*. Science, **287**(5457): p. 1447-1453. (2000).

25. Imamog¯lu, A., Awschalom, D.D., Burkard, G., DiVincenzo, D.P., Loss, D., Sherwin, M., and Small, A., *Quantum Information Processing using Quantum Dot Spins and Cavity QED*. Physical Review Letters, **83**(20): p. 4204-4207. (1999).

26. Zheng, S.-B. and Guo, G.-C., *Efficient Scheme for Two-Atom Entanglement and Quantum Information Processing in Cavity QED*. Physical Review Letters, **85**(11): p. 2392-2395. (2000).

27. Zheng, S.-B., *Quantum-information Processing and Multiatom-Entanglement Engineering with a Thermal Cavity*. Physical Review A, **66**(6). (2002).

28. Lukin, M.D., Fleischhauer, M., Cote, R., Duan, L.M., Jaksch, D., Cirac, J.I., and Zoller, P., *Dipole Blockade and Quantum Information Processing in Mesoscopic Atomic Ensembles*. Physical Review Letters, **87**(3). (2001).

29. Duan, L.M., Kuzmich, A., and Kimble, H.J., *Cavity QED and Quantum-Information Processing with "Hot" Trapped Atoms*. Physical Review A, **67**(3). (2003).

30. van Enk, S.J., Kimble, H.J., and Mabuchi, H., *Quantum Information Processing in Cavity-QED*. Quantum Information Processing, **3**(1): p. 75-90. (2004).

31. Haroche, S. *Trapping Photons in Microspheres for Cavity QED Experiments*. in *Quantum Electronics and Laser Science Conference, 1996. QELS '96., Summaries of Papers Presented at the*. (1996)

32. Vernooy, D.W., Furusawa, A., Georgiades, N.P., Ilchenko, V.S., and Kimble, H.J., *Cavity QED with High-Q Whispering Gallery Modes*. Physical Review A, **57**(4): p. R2293-R2296. (1998).

33. Benson, O. and Yamamoto, Y., *Master-Equation Model of a Single-Quantum-Dot Microsphere Laser*. Physical Review A, **59**(6): p. 4756-4763. (1999).

34. Kippenberg, T.J., Spillane, S.M., Armani, D.K., and Vahala, K.J., *Fabrication and Coupling to Planar High-Q Silica Disk Microcavities*. Applied Physics Letters, **83**(4): p. 797-799. (2003).

35. Armani, D.K., Kippenberg, T.J., Spillane, S.M., and Vahala, K.J., *Ultra-High-Q Toroid Microcavity on a Chip*. Nature, **421**(6926): p. 925-928. (2003).

36. Buck, J., Cavity QED in microsphere and Fabry-Perot Cavities, Thesis, (2003)

37. Treussart, F., Ilchenko, V.S., Roch, J.F., Hare, J., Lefèvre-Seguin, V., Raimond, J.M., and Haroche, S., *Evidence for Intrinsic Kerr Bistability of High-Q Microsphere Resonators in Superfluid Helium*. The European Physical Journal D, **1**(3). (1998).

38. Aoki, T., Dayan, B., Wilcut, E., Bowen, W.P., Parkins, A.S., Kippenberg, T.J., Vahala, K.J., and Kimble, H.J., *Observation of Strong Coupling between One Atom and a Monolithic Microresonator*. Nature, **443**(7112): p. 671-674. (2006).

39. Reithmaier, J.P., Sek, G., Loffler, A., Hofmann, C., Kuhn, S., Reitzenstein, S., Keldysh, L.V., Kulakovskii, V.D., Reinecke, T.L., and Forchel, A., *Strong Coupling in a Single Quantum Dot-Semiconductor Microcavity System*. Nature, **432**(7014): p. 197-200. (2004).

40. Yoshie, T., Scherer, A., Hendrickson, J., Khitrova, G., Gibbs, H.M., Rupper, G., Ell, C., Shchekin, O.B., and Deppe, D.G., *Vacuum Rabi Splitting with a Single Quantum Dot in a Photonic Crystal Nanocavity*. Nature, **432**(7014): p. 200-203. (2004).

41. Peter, E., Senellart, P., Martrou, D., Lemaître, A., Hours, J., Gérard, J.M., and Bloch, J., *Exciton-Photon Strong-Coupling Regime for a Single Quantum Dot Embedded in a Microcavity*. Physical Review Letters, **95**(6). (2005).

42. Hennessy, K., Badolato, A., Winger, M., Gerace, D., Atatüre, M., Gulde, S., Fält, S., Hu, E.L., and Imamoğlu, A., *Quantum Nature of a Strongly Coupled Single Quantum Dot–Cavity System*. Nature, **445**(7130): p. 896-899. (2007).

43. Englund, D., Fushman, I., and Vuckovi, J., *General Recipe for Designing Photonic Crystal Cavities*. Optics Express, **13**(16): p. 5961-5975. (2005).

44. Reitzenstein, S. and Forchel, A., *Quantum Dot Micropillars*. Journal of Physics D: Applied Physics, **43**(3). (2010).

45. Park, H.-G., Kim, S.-H., Kwon, S.-H., Ju, Y.-G., Yang, J.-K., Baek, J.-H., Kim, S.-B., and Lee, Y.-H., *Electrically Driven Single-Cell Photonic Crystal Laser*. Science, **305**(5689): p. 1444-1447. (2004).

46. Ulrich, S.M., Gies, C., Ates, S., Wiersig, J., Reitzenstein, S., Hofmann, C., Löffler, A., Forchel, A., Jahnke, F., and Michler, P., *Photon Statistics of Semiconductor Microcavity Lasers*. Physical Review Letters, **98**(4). (2007).

47. Lalanne, P., Sauvan, C., and Hugonin, J.p., *Photon Confinement in Photonic Crystal Nanocavities*. Laser & Photonics Reviews, **2**(6): p. 514-526. (2008).

48. Solomon, G.S., Pelton, M., and Yamamoto, Y., *Spectral Tuning of the Coupling Between Isolated InAs Quantum Dots and the Fundamental Micropost Cavity Mode*. physica status solidi (c), **0**(4): p. 1205-1208. (2003).

49. Thon, S.M., Rakher, M.T., Kim, H., Gudat, J., Irvine, W.T.M., Petroff, P.M., and Bouwmeester, D., *Strong Coupling through Optical Positioning of a Quantum Dot in a Photonic Crystal Cavity*. Applied Physics Letters, **94**(11). (2009).

50. McCutcheon, M.W. and Loncar, M., *Design of a Silicon Nitride Photonic Crystal Nanocavity with a Quality factor of One Million for Coupling to a Diamond Nanocrystal*. Optics Express, **16**(23): p. 9. (2008).

51. Larsson, M., Dinyari, K.N., and Wang, H., *Composite Optical Microcavity of Diamond Nanopillar and Silica Microsphere*. Nano Letters, **9**(4): p. 1447-1450. (2009).

52. Young, A., Hu, C.Y., Marseglia, L., Harrison, J.P., O'Brien, J.L., and Rarity, J.G., *Cavity enhanced Spin Measurement of the Ground State Spin of an NV Center in Diamond*. New Journal of Physics, **11**(1). (2009).

53. Barclay, P.E., Fu, K.-M., Santori, C., and Beausoleil, R.G., *Hybrid Photonic Crystal Cavity and Waveguide for Coupling to Diamond NV-Centers*. Optics Express, **17**(12): p. 9588-9601. (2009).

54. Barclay, P.E., Santori, C., Fu, K.-M., Beausoleil, R.G., and Painter, O., *Coherent Interference Effects in a Nano-Assembled Diamond NV Center Cavity-QED System*. Optics Express, **17**(10). (2009).

55. Englund, D., Shields, B., Rivoire, K., Hatami, F., Vučković, J., Park, H., and Lukin, M.D., *Deterministic Coupling of a Single Nitrogen Vacancy Center to a Photonic Crystal Cavity*. Nano Letters, **10**(10): p. 3922-3926. (2010).

56. Hanson, R., Dobrovitski, V.V., Feiguin, A.E., Gywat, O., and Awschalom, D.D., *Coherent Dynamics of a Single Spin Interacting with an Adjustable Spin Bath*. Science, **320**(5874): p. 352-355. (2008).

57. Wrachtrup, J., Kilin, S., and Nizovtsev, A., *Quantum Computation Using the 13C Nuclear Spins Near the Single NV Defect Center in Diamond*. Optics and Spectroscopy, **91**(3): p. 429-437. (2001).

58. Rabeau, J.R., Reichart, P., Tamanyan, G., Jamieson, D.N., Prawer, S., Jelezko, F., Gaebel, T., Popa, I., Domhan, M., and Wrachtrup, J., *Implantation of Labelled Single Nitrogen Vacancy Centers in Diamond using 15N*. Applied Physics Letters, **88**(2): p. 023113-023113-3. (2006).

59. Dietl, T., Awschalom, D.D., Kaminska, M., and Ohno, H., *Spintronics*, (2008)

60. Steck, D., *Quantum and Atom Optics*, Eugene, Oregon, (2012)

61. Berman, P.R., *Cavity Quantum Electrodynamics*, (1994)

62. Jaynes, E.T. and Cummings, F.W., *Comparison of Quantum and Semiclassical Radiation Theories with Application to the Beam Maser*. Proceedings of the IEEE, **51**(1): p. 20. (1963).

63. Miller, R., Northup, T.E., Birnbaum, K.M., Boca, A., Boozer, A.D., and Kimble, H.J., *Trapped Atoms in Cavity QED: Coupling Quantized Light and Matter*. Journal of Physics B-Atomic Molecular and Optical Physics, **38**(9): p. S551-S565. (2005).

64. Vernooy, D.W. and Kimble, H.J., *Quantum Structure and Dynamics for Atom Galleries*. Physical Review A, **55**(2): p. 1239-1261. (1997).

65. Vernooy, D.W., Ilchenko, V.S., Mabuchi, H., Streed, E.W., and Kimble, H.J., *High-Q Measurements of Fused-Silica Microspheres in the Near Infrared*. Optics Letters, **23**(4): p. 247-249. (1998).

66. Childs, J.J., Atom-Field Interaction in Optical Resonators, Thesis, (1980)

67. Heinzen, D.J., Childs, J.J., Thomas, J.E., and Feld, M.S., *Enhanced and Inhibited Visible Spontaneous Emission by Atoms in a Confocal Resonator*. Physical Review Letters, **58**(13): p. 1320-1323. (1987).

68. Kimble, H.J., *Strong Interactions of Single Atoms and Photons in Cavity QED*. Physica Scripta, **T76**(1). (1998).

69. Hahn, K.H., King, D.A., and Harris, S.E., *Nonlinear Generation of 104.8-Nm Radiation within an Absorption Window in Zinc*. Physical Review Letters, **65**(22): p. 2777-2779. (1990).

70. Boller, K.J., Imamoglu, A., and Harris, S.E., *Observation of Electromagnetically Induced Transparency*. Physical Review Letters, **66**(20): p. 2593-2596. (1991).

71. Maki, J.J., Malcuit, M.S., Sipe, J.E., and Boyd, R.W., *Linear and Nonlinear Optical Measurements of the Lorentz Local Field*. Physical Review Letters, **67**(8): p. 972-975. (1991).

72. Lukin, M.D., Fleischhauer, M., Zibrov, A.S., Robinson, H.G., Velichansky, V.L., Hollberg, L., and Scully, M.O., *Spectroscopy in Dense Coherent Media: Line Narrowing and Interference Effects*. Physical Review Letters, **79**(16): p. 2959-2962. (1997).

73. Kuklinski, J.R., Gaubatz, U., Hioe, F.T., and Bergmann, K., *Adiabatic Population Transfer in a 3-Level System Driven by Delayed Laser-Pulses*. Physical Review A, **40**(11): p. 6741-6744. (1989).

74. Gaubatz, U., Rudecki, P., Schiemann, S., and Bergmann, K., *Population Transfer between Molecular Vibrational Levels by Stimulated Raman-Scattering with Partially Overlapping Laserfields - a New Concept and Experimental Results*. Journal of Chemical Physics, **92**(9): p. 5363-5376. (1990).

75. Fleischhauer, M., Imamoglu, A., and Marangos, J.P., *Electromagnetically Induced Transparency: Optics in Coherent Media*. Reviews of Modern Physics, **77**(2): p. 633-673. (2005).

76. Martin, M.J., Meiser, D., Thomsen, J.W., Ye, J., and Holland, M.J., *Extreme Nonlinear Response of Ultranarrow Optical Transitions in Cavity QED for Laser Stabilization*. Physical Review A, **84**(6). (2011).

77. Mucke, M., Figueroa, E., Bochmann, J., Hahn, C., Murr, K., Ritter, S., Villas-Boas, C.J., and Rempe, G., *Electromagnetically Induced Transparency with Single Atoms in a Cavity*. Nature, **465**(7299): p. 755-758. (2010).

78. Hofling, E., Werner, R., Schafer, F., Reithmaier, J.P., and Forchel, A., *Short-Cavity Edge-Emitting Lasers with Deeply Etched Distributed Bragg Mirrors*. Electronics Letters, **35**(2): p. 154-155. (1999).

79. Bermel, P., Rodriguez, A., Johnson, S.G., Joannopoulos, J.D., and Soljacic, M., *Single-Photon All-Optical Switching using Waveguide-Cavity Quantum Electrodynamics*. Physical Review A, **74**(4). (2006).

80. Cardimona, D.A., Alsing, P.M., Mozer, H., and Rhodes, C., *Interference Effects in a Three-level Atom in a Cavity Beyond the Weak-Field Approximation*. Physical Review A, **79**(6). (2009).

81. Jackson, J.D., *Classical Electrodynamics*, (1999)

82. Streed, E., Spectroscopy of Very High-Q Whispering Gallery Modes in Silica Microspheres., Thesis, (1999)

83. Stratton, J.A., *Electromagnetic Theory*, The United States of America, (1941)

84. Knight, J.C., Dubreuil, N., Sandoghdar, V., Hare, J., LefevreSeguin, V., Raimond, J.M., and Haroche, S., *Characterizing Whispering-Gallery Modes in Microspheres by Direct Observation of the Optical Standing-Wave Pattern in the Near Field*. Optics Letters, **21**(10): p. 698-700. (1996).

85. Roll, G., Optische Mikroresonatoren: Beschreibung im Bild der Geometrischen Optik, Thesis, (1999)

86. Barber, P.W. and Chang, R.K., *Optical Effects Associated with Small Particles*, Singapore, (1988)

87. van de Hulst, H.C., *Light Scattering by Small Particles*, New York, (1981)

88. Gorodetsky, M.L. and Ilchenko, V.S., *High-Q Optical Whispering-Gallery Microresonators - Precession Approach for Spherical Mode Analysis and Emission Patterns with Prism Couplers*. Optics Communications, **113**(1-3): p. 133-143. (1994).

89. Schiller, S., *Asymptotic Expansion of Morphological Resonance Frequencies in Mie Scattering*. Applied Optics, **32**(12): p. 2181-2185. (1993).

90. Braginsky, V.B., Gorodetsky, M.L., and Ilchenko, V.S., *Quality-Factor and Nonlinear Properties of Optical Whispering-Gallery Modes*. Physics Letters A, **137**(7–8): p. 393-397. (1989).

91. Gorodetsky, M.L., Pryamikov, A.D., and Ilchenko, V.S., *Rayleigh Scattering in High-Q Microspheres*. Journal of the Optical Society of America B, **17**(6): p. 1051-1057. (2000).

92. Mazzei, A., Götzinger, S., de S. Menezes, L., Zumofen, G., Benson, O., and Sandoghdar, V., *Controlled Coupling of Counterpropagating Whispering-Gallery Modes by a Single Rayleigh Scatterer: A Classical Problem in a Quantum Optical Light*. Physical Review Letters, **99**(17). (2007).

93. Kim, W., Özdemir, Ş.K., Zhu, J., and Yang, L., *Observation and Characterization of Mode Splitting in Microsphere Resonators in Aquatic Environment*. Applied Physics Letters, **98**(14): p. 141106-141106-3. (2011).

94. Osanai, H., Shioda, T., Moriyama, T., Araki, S., Horiguchi, M., Izawa, T., and Takata, H., *Effect of Dopants on Transmission Loss of Low-Oh-Content Optical Fibers*. Electronics Letters, **12**(21): p. 549-550. (1976).

95. Horiguchi, M. and Osanai, H., *Spectral Losses of Low-Oh-Content Optical Fibers*. Electronics Letters, **12**(12): p. 310-312. (1976).

96. Lacey, S., Ray and Wave Dynamics in Three Dimensional Asymemetric Optical Resonators, Thesis, The United States of America (2003)

97. Gorodetsky, M.L. and Ilchenko, V.S., *Optical Microsphere Resonators: Optimal Coupling to High-Q Whispering-Gallery Modes*. Journal of the Optical Society of America B, **16**(1): p. 147-154. (1999).

98. Dubreuil, N., Knight, J.C., Leventhal, D.K., Sandoghdar, V., Hare, J., and Lefevre, V., *Eroded Monomode Optical-Fiber for Whispering-Gallery Made Excitation in Fused-Silica Microspheres*. Optics Letters, **20**(8): p. 813-815. (1995).

99. Knight, J.C., Cheung, G., Jacques, F., and Birks, T.A., *Phase-Matched Excitation of Whispering-Gallery-Mode Resonances by a Fiber Taper*. Optics Letters, **22**(15): p. 1129-1131. (1997).

100. Matsko, A.B. and Ilchenko, V.S., *Optical Resonators with Whispering-Gallery Modes-Part I: Basics*. IEEE Journal of Selected Topics in Quantum Electronics, **12**(1): p. 3-14. (2006).

101. Park, Y.-S. and Wang, H., *Radiation Pressure Driven Mechanical Oscillation in Deformed Silica Microspheres via Free-Space Evanescent Excitation*. Optics Express, **15**(25): p. 16471-16477. (2007).

102. Mekis, A., Nöckel, J.U., Chen, G., Stone, A.D., and Chang, R.K., *Ray Chaos and Q Spoiling in Lasing Droplets*. Physical Review Letters, **75**(14): p. 2682-2685. (1995).

103. Nöckel, J.U. and Stone, A.D., *Ray and Wave Chaos in Asymmetric Resonant Optical Cavities*. Nature, **385**(6611): p. 45-47. (1997).

104. Nöckel, J.U., Stone, A.D., Chen, G., Grossman, H.L., and Chang, R.K., *Directional Emission from Asymmetric Resonant Cavities*. Optics Letters, **21**(19): p. 1609-1611. (1996).

105. Lacey, S. and Wang, H., *Directional Emission from Whispering-Gallery Modes in Deformed Fused-Silica Microspheres*. Optics Letters, **26**(24): p. 1943-1945. (2001).

106. Park, Y.-S., Cook, A.K., and Wang, H., *Cavity QED with Diamond Nanocrystals and Silica Microspheres*. Nano Lett., **6**(9): p. 2075-2079. (2006).

107. Lacey, S., Wang, H., Foster, D.H., and Nöckel, J.U., *Directional Tunneling Escape from Nearly Spherical Optical Resonators*. Physical Review Letters, **91**(3). (2003).

108. Park, Y.-S., Radiation Pressure Cooling of a Silica Optomechanical Resonator, Thesis, The United States of America (2009)

109. Fan, X., Cavity-QED Studies of Composite Semiconductor Nanostructure and Dielectric Microsphere System, Thesis, The United States of America (2000)

110. Kneubuhl, F.K. and Sigrist, M.W., *Laser*, Teubner, Stuttgar, Leipzig, (1999)

111. Siegman, A.E., *Lasers*, The United States of America, (1986)

112. Gorodetsky, M.L., Savchenkov, A.A., and Ilchenko, V.S., *Ultimate Q of Optical Microsphere Resonators*. Optics Letters, **21**(7): p. 453-455. (1996).

113. Schiller, S. and Byer, R.L., *High-Resolution Spectroscopy of Whispering Gallery Modes in Large Dielectric Spheres*. Optics Letters, **16**(15): p. 1138-1140. (1991).

114. Born, M. and Wolf, E., *Principles of Optics: Electromagnetic Theory of Propagation, Interference and Diffraction of Light*, (1997)

115. Menezes, L.D., Götzinger, S., Mazzei, A., Sandoghdar, V., and Benson, O., *Nanoparticles and Microspheres: Tools to Study the Interaction of Quantum Emitters via Shared Optical Modes*. Laser Resonators and Beam Control, **7**: p. 8. (2004).

116. Mononobe, S. and Ohtsu, M., *Fabrication of a Pencil-Shaped Fiber Probe for Near-Field Optics by Selective Chemical Etching*. Journal of Lightwave Technology, **14**(10): p. 2231-2235. (1996).

117. von Klitzing, W., Long, R., Ilchenko, V.S., Hare, J., and Lefèvre-Seguin, V., *Frequency Tuning of the Whispering-Gallery Modes of Silica Microspheres for Cavity Quantum Electrodynamics and Spectroscopy*. Optics Letters, **26**(3): p. 166-168. (2001).

118. Ilchenko, V.S., Volikov, P.S., Velichansky, V.L., Treussart, F., Lefevre-Seguin, V., Raimond, J.M., and Haroche, S., *Strain-Tunable High-Q Optical Microsphere Resonator*. Optics Communications, **145**(1-6): p. 86-90. (1998).

119. Obermuller, C., Deisenrieder, A., Abstreiter, G., Karrai, K., Grosse, S., Manus, S., Feldmann, J., Lipsanen, H., Sopanen, M., and Ahopelto, J., *Mechanical Nanomanipulation of Single Strain-Induced Semiconductor Quantum Dots*. Applied Physics Letters, **75**(3): p. 358-360. (1999).

120. Obermuller, C., Deisenrieder, A., Abstreiter, G., Karrai, K., Grosse, S., Manus, S., Feldmann, J., Lipsanen, H., Sopanen, M., and Ahopelto, J., *Pauli-Blocking Imaging of Single Strain-Induced Semiconductor Quantum Dots*. Applied Physics Letters, **74**(21): p. 3200-3202. (1999).

121. White, I.M., Hanumegowda, N.M., Oveys, H., and Fan, X., *Tuning Whispering Gallery Modes in Optical Microspheres with Chemical Etching*. Optics Express, **13**(26): p. 10754-10759. (2005).

122. Mosor, S., Hendrickson, J., Richards, B.C., Sweet, J., Khitrova, G., Gibbs, H.M., Yoshie, T., Scherer, A., Shchekin, O.B., and Deppe, D.G., *Scanning a Photonic Crystal Slab Nanocavity by Condensation of Xenon*. Applied Physics Letters, **87**(14): p. 141105-141105-3. (2005).

123. Park, Y.-S. and Wang, H., *Regenerative Pulsation in Silica Microspheres*. Optics Letters, **32**(21): p. 3104-3106. (2007).

124. Watkins, A., Ward, J., and Chormaic, S.N., *Thermo-Optical Tuning of Whispering Gallery Modes in Erbium: Ytterbium Doped Glass Microspheres to Arbitrary Probe Wavelengths*. Japanese Journal of Applied Physics, **51**(5). (2012).

125. Cai, Z., Chardon, A., Xu, H., Féron, P., and Michel Stéphan, G., *Laser characteristics at 1535 nm and thermal effects of an Er:Yb phosphate glass microchip pumped by Ti:sapphire laser*. Optics Communications, **203**(3–6): p. 301-313. (2002).

126. Ward, J. and Chormaic, S., *Thermo-Optical Tuning of Whispering Gallery Modes in Er:Yb Co-Doped Phosphate Glass Microspheres*. Applied Physics B: Lasers and Optics, **100**(4): p. 847-850. (2010).

127. White, G.K., *Thermal-Expansion of Reference Materials - Copper, Silica and Silicon*. Journal of Physics D-Applied Physics, **6**(17): p. 2070-2078. (1973).

128. Jewell, J.L., Gibbs, H.M., Tarng, S.S., Gossard, A.C., and Wiegmann, W., *Regenerative Pulsations from an Intrinsic Bistable Optical-Device*. Applied Physics Letters, **40**(4): p. 291-293. (1982).

129. Zak, J.K., Butler, J.E., and Swain, G.M., *Diamond Optically Transparent Electrodes: Demonstration of Concept with Ferri/Ferrocyanide and Methyl Viologen*. Analytical Chemistry, **73**(5): p. 908-914. (2001).

130. Kittel, C., *Introduction to Solid State Physics*, The United States of America, (2005)

131. Greentree, A.D., Fairchild, B.A., Hossain, F.M., and Prawer, S., *Diamond Integrated Quantum Photonics*. Materials Today, **11**(9): p. 22-31. (2008).

132. Popov, C., Kulisch, W., Reithmaier, J.P., Dostalova, T., Jelinek, M., Anspach, N., and Hammann, C., *Bioproperties of Nanocrystalline Diamond/Amorphous Carbon Composite Films*. Diamond and Related Materials, **16**(4-7): p. 735-739. (2007).

133. Kulisch, W., Popov, C., Bliznakov, S., Ceccone, G., Gilliland, D., Sirghi, L., and Rossi, F., *Surface and Bioproperties of Nanocrystalline Diamond/Amorphous Carbon Nanocomposite Films*. Thin Solid Films, **515**(23): p. 8407-8411. (2007).

134. Collins, A.T., Woad, P.J., Woods, G.S., and Kanda, H., *Localized Vibrational-Modes in Diamonds Grown from Mixed Carbon Isotopes*. Diamond and Related Materials, **2**(2-4): p. 136-141. (1993).

135. Peter, F., *Uber Brechungsindizes und Absorptionskonstanten des Diamanten zwischen 644 und 226 μm*. Zeitshrift FÜR Physik a Hadrons and Nuclei, **15**: p. 10. (1923).

136. Howell, D., *Strain-Induced Birefringence in Natural Diamond: A Review*. European Journal of Mineralogy, **24**(4): p. 575-585. (2012).

137. Zaitsev, A., *Optical Properties of Diamond*, Berlin Heidelber New York, (2001)

138. Field, J.R., *The Properties of Natural and Synthetic Diamond*, (1979)

139. Ohno, K., Heremans, F.J., Bassett, L.C., Myers, B.A., Toyli, D.M., Jayich, A.C.B., Palmstrom, C.J., and Awschalom, D.D., *Engineering Shallow Spins in Diamond with Nitrogen Delta-Doping*. Applied Physics Letters, **101**(8). (2012).

140. Martin, J., Wannemacher, R., Teichert, J., Bischoff, L., and Köhler, B., *Generation and Detection of Fluorescent Color Centers in Diamond with Submicron Resolution*. Applied Physics Letters, **75**(20): p. 3096-3098. (1999).

141. Aharonovich, I., Novel Single Photon Emitters Based on Color Centers in Diamond, Thesis, (2010)

142. Hunt, D.C., Twitchen, D.J., Newton, M.E., Baker, J.M., Kirui, J.K., van Wyk, J.A., Anthony, T.R., and Banholzer, W.F., *EPR Data on the Self-Interstitial Complex O3 in Diamond*. Physical Review B, **62**(10): p. 6587-6597. (2000).

143. Hunt, D.C., Twitchen, D.J., Newton, M.E., Baker, J.M., Anthony, T.R., Banholzer, W.F., and Vagarali, S.S., *Identification of the Neutral Carbon [100]-Split Interstitial in Diamond*. Physical Review B, **61**(6): p. 3863-3876. (2000).

144. Rand, S.C. and Deshazer, L.G., *Visible Color-Center Laser in Diamond*. Optics Letters, **10**(10): p. 481-483. (1985).

145. Kaiser, W. and Bond, W.L., *Nitrogen, A Major Impurity in Common Type Ia Diamond*. Physical Review, **115**(4): p. 6. (1959).

146. Davies, G. and Hamer, M.F., *Optical Studies of 1.945 Ev Vibronic Band in Diamond*. Proceedings of the Royal Society of London Series A-Mathematical and Physical Sciences, **348**(1653): p. 285-298. (1976).

147. Neves, A.J. and Nazare, M.H., *Properties, Growth and Applications of Diamond*, United Kingdom, (2001)

148. Babamoradi, M., Saani, M.H., Ranjbar, A., Vesaghi, M.A., and Kawazoe, Y., *Effect of Lattice Relaxation on Spin Density of Nitrogen-Vacancy Centers in Diamond and Oscillator Strength Calculations*. European Physical Journal B, **84**(1): p. 1-9. (2011).

149. Jelezko, F. and Wrachtrup, J., *Single Defect Centres in Diamond: A Review*. Physica Status Solidi a-Applications and Materials Science, **203**(13): p. 3207-3225. (2006).

150. van Oort, E., Stroomer, P., and Glasbeek, M., *Low-Field Optically Detected Magnetic Resonance of a Coupled Triplet-Doublet Defect Pair in Diamond*. Physical Review B, **42**(13): p. 8605-8608. (1990).

151. Jelezko, F., Gaebel, T., Popa, I., Gruber, A., and Wrachtrup, J., *Observation of Coherent Oscillations in a Single Electron Spin*. Physical Review Letters, **92**(7). (2004).

152. Hemmer, P.R., Turukhin, A.V., Shahriar, M.S., and Musser, J.A., *Raman-Excited Spin Coherences in Nitrogen-Vacancy Color Centers in Diamond*. Optics Letters, **26**(6): p. 361-363. (2001).

153. Tamarat, P., Gaebel, T., Rabeau, J.R., Khan, M., Greentree, A.D., Wilson, H., Hollenberg, L.C.L., Prawer, S., Hemmer, P., Jelezko, F., and Wrachtrup, J., *Stark Shift Control of Single Optical Centers in Diamond*. Physical Review Letters, **97**(8). (2006).

154. Manson, N.B., Harrison, J.P., and Sellars, M.J., *Nitrogen-Vacancy Center in Diamond: Model of the Electronic Structure and Associated Dynamics*. Physical Review B, **74**(10). (2006).

155. Vanoort, E., Manson, N.B., and Glasbeek, M., *Optically Detected Spin Coherence of the Diamond N-V Center in Its Triplet Ground-State*. Journal of Physics C-Solid State Physics, **21**(23): p. 4385-4391. (1988).

156. Fuchs, G.D., Dobrovitski, V.V., Hanson, R., Batra, A., Weis, C.D., Schenkel, T., and Awschalom, D.D., *Excited-State Spectroscopy using Single Spin Manipulation in Diamond*. Physical Review Letters, **101**(11). (2008).

157. Wang, R., Zhang, X., Cen, X., Zhang, C., Fan, Y., and Fu, Z., *Evaluation of the Clinical Application value of 18F-fluorodeoxyglucose Metabolic Imaging using Single Photon Emission Computed Tomography with Coincidence Detecting in Lymphoma*. European Journal of Nuclear Medicine and Molecular Imaging, **34**: p. S307-S307. (2007).

158. Beha, K., Batalov, A., Manson, N.B., Bratschitsch, R., and Leitenstorfer, A., *Optimum Photoluminescence Excitation and Recharging Cycle of Single Nitrogen-Vacancy Centers in Ultrapure Diamond*. Physical Review Letters, **109**(9). (2012).

159. Doherty, M.W., Dolde, F., Fedder, H., Jelezko, F., Wrachtrup, J., Manson, N.B., and Hollenberg, L.C.L., *Theory of the Ground-State Spin of the NV- Center in Diamond*. Physical Review B, **85**(20). (2012).

160. Neumann, P., Kolesov, R., Jacques, V., Beck, J., Tisler, J., Batalov, A., Rogers, L., Manson, N.B., Balasubramanian, G., Jelezko, F., and Wrachtrup, J., *Excited-State Spectroscopy of Single NV Defects in Diamond Using Optically Detected Magnetic Resonance*. New Journal of Physics, **11**. (2009).

161. van Oort, E., van der Kamp, B., Sitter, R., and Glasbeek, M., *Microwave-Induced Line-Narrowing of the N-V Defect Absorption in Diamond*. Journal of Luminescence, **48–49, Part 2**(0): p. 803-806. (1991).

162. Shen, Y., Sweeney, T.M., and Wang, H., *Zero-Phonon Linewidth of Eingle Nitrogen Vacancy Centers in Diamond Nanocrystals*. Physical Review B, **77**(3). (2008).

163. Tisler, J., Balasubramanian, G., Naydenov, B., Kolesov, R., Grotz, B., Reuter, R., Boudou, J.-P., Curmi, P.A., Sennour, M., Thorel, A., Börsch, M., Aulenbacher, K., Erdmann, R., Hemmer, P.R., Jelezko, F., and Wrachtrup, J.r., *Fluorescence and Spin Properties of Defects in Single Digit Nanodiamonds*. ACS Nano, **3**(7): p. 1959-1965. (2009).

164. Pham, L.M., Bar-Gill, N., Le Sage, D., Belthangady, C., Stacey, A., Markham, M., Twitchen, D.J., Lukin, M.D., and Walsworth, R.L., *Enhanced Metrology using Preferential Orientation of Nitrogen-Vacancy Centers in Diamond*. Physical Review B, **86**(12). (2012).

165. Tamarat, P., Manson, N.B., Harrison, J.P., McMurtrie, R.L., Nizovtsev, A., Santori, C., Beausoleil, R.G., Neumann, P., Gaebel, T., Jelezko, F., Hemmer, P., and Wrachtrup, J., *Spin-Flip and Spin-Conserving Optical Transitions of the Nitrogen-Vacancy Centre in Diamond*. New Journal of Physics, **10**(4). (2008).

166. Wrachtrup, J. and Jelezko, F., *Processing Quantum Information in Diamond*. Journal of Physics: Condensed Matter, **18**(21): p. S807-S824. (2006).

167. Horowitz, V.R., Alemán, B.J., Christle, D.J., Cleland, A.N., and Awschalom, D.D., *Electron Spin Resonance of Nitrogen-Vacancy Centers in Optically Trapped Nanodiamonds*. Proceedings of the National Academy of Sciences, **109**(34): p. 13493-13497. (2012).

168. Hanson, R., Mendoza, F.M., Epstein, R.J., and Awschalom, D.D., *Polarization and Readout of Coupled Single Spins in Diamond*. Physical Review Letters, **97**(8). (2006).

169. Robledo, L., Childress, L., Bernien, H., Hensen, B., Alkemade, P.F.A., and Hanson, R., *High-Fidelity Projective Read-Out of a Solid-State Spin Quantum Register*. Nature, **477**(7366): p. 574-578. (2011).

170. Shin, C., Kim, C., Kolesov, R., Balasubramanian, G., Jelezko, F., Wrachtrup, J., and Hemmer, P.R., *Sub-Optical Resolution of Single Spins using Magnetic Resonance Imaging at Room Temperature in Diamond*. Journal of Luminescence, **130**(9): p. 1635-1645. (2010).

171. Childress, L., Coherent Manipulation of Single Quantum Systems in the Solid State, Thesis, Boston (2007)

172. Balasubramanian, G., Neumann, P., Twitchen, D., Markham, M., Kolesov, R., Mizuochi, N., Isoya, J., Achard, J., Beck, J., Tissler, J., Jacques, V., Hemmer, P.R., Jelezko, F., and Wrachtrup, J., *Ultralong Spin Coherence Time in Isotopically Engineered Diamond*. Nature Materials, **8**(5): p. 383-387. (2009).

173. Buckley, B.B., Fuchs, G.D., Bassett, L.C., and Awschalom, D.D., *Spin-Light Coherence for Single-Spin Measurement and Control in Diamond*. Science, **330**(6008): p. 1212-1215. (2010).

174. Childress, L., Dutt, M.V.G., Taylor, J.M., Zibrov, A.S., Jelezko, F., Wrachtrup, J., Hemmer, P.R., and Lukin, M.D., *Coherent Dynamics of Coupled Electron and Nuclear Spin Qubits in Diamond*. Science, **314**(5797): p. 281-285. (2006).

175. Maurer, P.C., Kucsko, G., Latta, C., Jiang, L., Yao, N.Y., Bennett, S.D., Pastawski, F., Hunger, D., Chisholm, N., Markham, M., Twitchen, D.J., Cirac, J.I., and Lukin, M.D., *Room-Temperature Quantum Bit Memory Exceeding One Second*. Science, **336**(6086): p. 1283-1286. (2012).

176. Gaebel, T., Domhan, M., Popa, I., Wittmann, C., Neumann, P., Jelezko, F., Rabeau, J.R., Stavrias, N., Greentree, A.D., Prawer, S., Meijer, J., Twamley, J., Hemmer, P.R., and Wrachtrup, J., *Room-Temperature Coherent Coupling of Single Spins in Diamond*. Nature Physics, **2**(6): p. 408-413. (2006).

177. Dutt, M.V.G., Childress, L., Jiang, L., Togan, E., Maze, J., Jelezko, F., Zibrov, A.S., Hemmer, P.R., and Lukin, M.D., *Quantum Register Based on Individual Electronic and Nuclear Spin Qubits in Diamond*. Science, **316**(5829): p. 1312-1316. (2007).

178. Neumann, P., Mizuochi, N., Rempp, F., Hemmer, P., Watanabe, H., Yamasaki, S., Jacques, V., Gaebel, T., Jelezko, F., and Wrachtrup, J., *Multipartite Entanglement Among Single Spins in Diamond*. Science, **320**(5881): p. 1326-1329. (2008).

179. Jelezko, F., Popa, I., Gruber, A., Tietz, C., Wrachtrup, J., Nizovtsev, A., and Kilin, S., *Single Spin States in a Defect Center Resolved by Optical Spectroscopy*. Applied Physics Letters, **81**(12): p. 2160-2162. (2002).

180. Nizovtsev, A., Kilin, S., Jelezko, F., Popa, I., Gruber, A., Tietz, C., and Wrachtrup, J., *Spin-Selective Low Temperature Spectroscopy on Single Molecules with a Triplet-Triplet Optical Transition: Application to the NV Defect Center in Diamond*. Optics and Spectroscopy, **94**(6): p. 848-858. (2003).

181. Santori, C., Fattal, D., Spillane, S.M., Fiorentino, M., Beausoleil, R.G., Greentree, A.D., Olivero, P., Draganski, M., Rabeau, J.R., Reichart, P., Gibson, B.C., Rubanov, S., Jamieson, D.N., and Prawer, S., *Coherent Population Trapping in Diamond N-V Centers at Zero Magneticfield*. Optics Express, **14**(17): p. 7986-7993. (2006).

182. Degen, C.L., *Scanning Magnetic Field Microscope with a Diamond Single-Spin Sensor*. Applied Physics Letters, **92**(24): p. 243111-243111-3. (2008).

183. Maze, J.R., Stanwix, P.L., Hodges, J.S., Hong, S., Taylor, J.M., Cappellaro, P., Jiang, L., Dutt, M.V.G., Togan, E., Zibrov, A.S., Yacoby, A., Walsworth, R.L., and Lukin, M.D., *Nanoscale Magnetic Sensing with an Individual Electronic Spin in Diamond*. Nature, **455**(7213): p. 644-647. (2008).

184. Jiang, L., Hodges, J.S., Maze, J.R., Maurer, P., Taylor, J.M., Cory, D.G., Hemmer, P.R., Walsworth, R.L., Yacoby, A., Zibrov, A.S., and Lukin, M.D., *Repetitive Readout of a Single Electronic Spin via Quantum Logic with Nuclear Spin Ancillae*. Science, **326**(5950): p. 267-272. (2009).

185. Schoenfeld, R.S. and Harneit, W., *Real Time Magnetic Field Sensing and Imaging using a Single Spin in Diamond*. Physical Review Letters, **106**(3). (2011).

186. Santori, C., Barclay, P.E., Fu, K.M.C., Beausoleil, R.G., Spillane, S., and Fisch, M., *Nanophotonics for Quantum Optics using Nitrogen-Vacancy Centers in Diamond*. Nanotechnology, **21**(27). (2010).

187. Neu, E., Fischer, M., Gsell, S., Schreck, M., and Becher, C., *Fluorescence and Polarization Spectroscopy of Single Silicon Vacancy Centers in Heteroepitaxial Nanodiamonds on Iridium*. Physical Review B, **84**(20). (2011).

188. Siyushev, P., Jacques, V., Aharonovich, I., Kaiser, F., Müller, T., Lombez, L., Atatüre, M., Castelletto, S., Prawer, S., Jelezko, F., and Wrachtrup, J., *Low-Temperature Optical Characterization of a Near-Infrared Single-Photon Emitter in Nanodiamonds*. New Journal of Physics, **11**(11). (2009).

189. Müller, T., Aharonovich, I., Lombez, L., Alaverdyan, Y., Vamivakas, A.N., Castelletto, S., Jelezko, F., Wrachtrup, J., Prawer, S., and Atatüre, M., *Wide-Range Electrical Tunability of Single-Photon Emission from Chromium-Based Colour Centres in Diamond*. New Journal of Physics, **13**(7). (2011).

190. Aharonovich, I., Castelletto, S., Johnson, B.C., McCallum, J.C., Simpson, D.A., Greentree, A.D., and Prawer, S., *Chromium Single-Photon Emitters in Diamond Fabricated by Ion Implantation*. Physical Review B, **81**(12). (2010).

191. Vavilov, V.S., Gippius, A.A., Zaitsev, A.M., Deryagin, B.V., V., S.B., and Aleksenko, A.E., *Investigation of the Cathodoluminescence of Epitaxial Diamond Films*. Soviet Physics Semiconductors-USSR, **14**(9): p. 1. (1981).

192. Kurtsiefer, C., Mayer, S., Zarda, P., and Weinfurter, H., *Stable Solid-State Source of Single Photons*. Physical Review Letters, **85**(2): p. 290-293. (2000).

193. Beveratos, A., Brouri, R., Gacoin, T., Poizat, J.P., and Grangier, P., *Nonclassical Radiation from Diamond Nanocrystals*. Physical Review A, **64**(6). (2001).

194. McGuinness, H.J., Raymer, M.G., McKinstrie, C.J., and Radic, S., *Quantum Frequency Translation of Single-Photon States in a Photonic Crystal Fiber*. Physical Review Letters, **105**(9). (2010).

195. Raymer, M.G., Hayden, M., Steven van, E., and Colin, M. *Quantum Frequency Translation and Interference of Two Photons of Different Color*. in *Laser Science*. Optical Society of America. (2011)

196. Takagi, H., Ogawa, H., Yamazaki, Y., Ishizaki, A., and Nakagiri, T., *Quantum Size Effects on Photoluminescence in Ultrafine Si Particles*. Applied Physics Letters, **56**(24): p. 2379-2380. (1990).

197. Marzin, J.Y., Gerard, J.M., Izrael, A., Barrier, D., and Bastard, G., *Photoluminescence of Single Inas Quantum Dots Obtained by Self-Organized Growth on Gaas*. Physical Review Letters, **73**(5): p. 716-719. (1994).

198. Brunner, K., Abstreiter, G., Bohm, G., Trankle, G., and Weimann, G., *Sharp-Line Photoluminescence and 2-Photon Absorption of Zero-Dimensional Biexcitons in a Gaas/Algaas Structure*. Physical Review Letters, **73**(8): p. 1138-1141. (1994).

199. Brunner, K., Abstreiter, G., Bohm, G., Trankle, G., and Weimann, G., *Sharp-Line Photoluminescence of Excitons Localized at Gaas/Algaas Quantum-Well Inhomogeneities*. Applied Physics Letters, **64**(24): p. 3320-3322. (1994).

200. Empedocles, S.A., Norris, D.J., and Bawendi, M.G., *Photoluminescence Spectroscopy of Single CdSe Nanocrystallite Quantum Dots*. Physical Review Letters, **77**(18): p. 3873-3876. (1996).

201. Franck, J. and Dymond, E.G., *Elementary Processes of Photochemical Reactions*. Transactions of the Faraday Society, **21**(February). (1926).

202. Vamivakas, A.N. and Atature, M., *Photons and (Artificial) Atoms: An Overview of Optical Spectroscopy Techniques on Quantum Dots*. Contemporary Physics, **51**(1): p. 17-36. (2010).

203. Monemar, B., *Fundamental Energy Gaps of Alas and Alp from Photoluminescence Excitation-Spectra*. Physical Review B, **8**(12): p. 5711-5718. (1973).

204. Monemar, B., *Fundamental Energy Gap of GaN from Photoluminescence Excitation Spectra*. Physical Review B, **10**(2): p. 676-681. (1974).

205. Ennen, H., Wagner, J., Muller, H.D., and Smith, R.S., *Photoluminescence Excitation Measurements on Gaas-Er Grown by Molecular-Beam Epitaxy*. Journal of Applied Physics, **61**(10): p. 4877-4879. (1987).

206. Bradac, C., Gaebel, T., Naidoo, N., Sellars, M.J., Twamley, J., Brown, L.J., Barnard, A.S., Plakhotnik, T., Zvyagin, A.V., and Rabeau, J.R., *Observation and Control of Blinking Nitrogen-Vacancy Centres in Discrete Nanodiamonds*. Nature Nanotechnology, **5**(5): p. 345-349. (2010).

207. Acosta, V.M., Bauch, E., Ledbetter, M.P., Santori, C., Fu, K.M.C., Barclay, P.E., Beausoleil, R.G., Linget, H., Roch, J.F., Treussart, F., Chemerisov, S., Gawlik, W., and Budker, D., *Diamonds with a High Density of Nitrogen-Vacancy Centers for Magnetometry Applications*. Physical Review B, **80**(11). (2009).

208. Choy, J.T., Hausmann, B.J.M., Babinec, T.M., Bulu, I., Khan, M., Maletinsky, P., Yacoby, A., and Loncar, M., *Enhanced Single-Photon Emission from a Diamond-Silver Aperture*. Nature Photonics, **5**(12): p. 738-743. (2011).

209. Hausmann, B.J.M., Babinec, T.M., Choy, J.T., Hodges, J.S., Hong, S.K., Bulu, I., Yacoby, A., Lukin, M.D., and Loncar, M., *Single-Color Centers Implanted in Diamond Nanostructures*. New Journal of Physics, **13**. (2011).

210. Toyli, D.M., Weis, C.D., Fuchs, G.D., Schenkel, T., and Awschalom, D.D., *Chip-Scale Nanofabrication of Single Spins and Spin Arrays in Diamond*. Nano Letters, **10**(8): p. 3168-3172. (2010).

211. Hiscocks, M.P., Ganesan, K., Gibson, B.C., Huntington, S.T., Ladouceur, F., and Prawer, S., *Diamond Waveguides Fabricated by Reactive Ion Etching*. Optics Express, **16**(24): p. 19512-19519. (2008).

212. Castelletto, S., Harrison, J.P., Marseglia, L., Stanley-Clarke, A.C., Gibson, B.C., Fairchild, B.A., Hadden, J.P., Ho, Y.L.D., Hiscocks, M.P., Ganesan, K., Huntington, S.T., Ladouceur, F., Greentree, A.D., Prawer, S., O'Brien, J.L., and Rarity, J.G., *Diamond-Based Structures to Collect and Guide Light*. New Journal of Physics, **13**. (2011).

213. Bayer, M., *Coherent Population Trapping - Quantum Optics with Dots*. Nature Physics, **4**(9): p. 678-679. (2008).

214. Xu, X.D., Sun, B., Berman, P.R., Steel, D.G., Bracker, A.S., Gammon, D., and Sham, L.J., *Coherent Population Trapping of an Electron Spin in a Single Negatively Charged Quantum Dot*. Nature Physics, **4**(9): p. 692-695. (2008).

215. Goldner, P., Guillot-Noel, O., Louchet, A., de Seze, F., Crozatier, V., Lorgere, I., Bretenaker, F., and Le Gouet, J.L., *Hyperfine Structure of Tm3+ in YAG for Quantum Storage Applications*. Optical Materials, **28**(6-7): p. 649-654. (2006).

216. Goldner, P., Guillot-Noel, O., Louchet, A., de Seze, F., Crozatier, V., Lorgere, I., Bretenaker, F., and Le Gouet, J.L., *Hole Burning Study of Tm3+ : YAG Hyperfine Structure for Quantum Storage Applications*. Journal of Luminescence, **119**: p. 293-297. (2006).

217. de Seze, F., Louchet, A., Crozatier, V., Lorgere, I., Bretenaker, F., Le Gouet, J.L., Guillot-Noel, O., and Goldner, P., *Experimental Tailoring of a Three-Level Lambda System in Tm3+: YAG*. Physical Review B, **73**(8). (2006).

218. Mazzei, A., Goetzinger, S., Menezes, L.D., Zumofen, G., Benson, O., and Sandoghdar, V., *Controlled coupling of counterpropagating whispering-gallery modes by a single Rayleigh scatterer: A classical problem in a quantum optical light*. Physical Review Letters, **99**(17). (2007).

219. Knight, J.C., Dnbreuil, N., Sandoghdar, V., Hare, J., Lefevreseguin, V., Raimond, J.M., and Haroche, S., *Mapping Whispering-Gallery Modes in Microspheres with a near-Field Probe*. Optics Letters, **20**(14): p. 1515-1517. (1995).

220. Teraoka, I., Arnold, S., and Vollmer, F., *Perturbation Approach to Resonance Shifts of Whispering-Gallery Modes in a Dielectric Microsphere as a Probe of a Surrounding Medium*. Journal of the Optical Society of America B-Optical Physics, **20**(9): p. 1937-1946. (2003).

221. Vollmer, F., Braun, D., Libchaber, A., Khoshsima, M., Teraoka, I., and Arnold, S., *Protein Detection by Optical Shift of a Resonant Microcavity*. Applied Physics Letters, **80**(21): p. 4057-4059. (2002).

222. Rezac, J.P. and Rosenberger, A.T., *Locking a Microsphere Whispering-Gallery Mode to a Laser*. Optics Express, **8**(11): p. 605-610. (2001).